REACTIVE MAGNETRON SPUTTERING AS A GROWTH ALTERNATIVE FOR GALLIUM NITRIDE NANOWIRES

REACTIVE MAGNETRON SPUTTERING AS A GROWTH ALTERNATIVE FOR GALLIUM NITRIDE NANOWIRES

By NIKOLAUS ANDREW CHRISTOPHER JEWELL, B.Eng., B.HSc (Hons)

A Thesis

Submitted to the School of Graduate Studies

in Partial Fulfillment of the Requirements

for the Degree

Master of Applied Science

McMaster University

MASTER OF APPLIED SCIENCE (2014) McMaster University

(Engineering Physics) Hamilton, Ontario

TITLE: Reactive Magnetron Sputtering as a Growth Alternative for Gallium Nitride Nanowires

AUTHOR: Nikolaus Andrew Christopher Jewell, B.Eng Engineering Physics, B.HSc Hons (McMaster University)

SUPERVISORS: Dr. R.R. LaPierre and Dr. A. Kitai

NUMBER OF PAGES: xvii, 159

Abstract

Gallium nitride nanowires are high-performance materials with wide, direct bandgaps and superior electron transport properties. Although their properties make them of great interest for next-generation light-emitting diodes, detectors, and display technologies, their widespread use has been limited by serial and expensive production processes, such as molecular beam epitaxy and metalorganic chemical vapor deposition, respectively. Here, the results of growing gallium nitride nanowires via DC magnetron sputtering at different temperatures and using different metal catalysts are reported.

A new substrate heater was designed to minimize contamination from the heater filament and increase the substrate temperature window to in excess of 900°C. Sixteen-mm^2 (111) silicon samples had one-to-four nm of a metal catalyst deposited on them using evaporation. This metal catalyst layer (gold, platinum, or nickel) was employed to induce catalyst-assisted vapor-liquid-solid nanowire growth. Samples were subjected to a hydrofluoric acid dip to remove surface oxide and then loaded into the deposition chamber where gallium nitride was deposited via a reactive nitrogen DC magnetron sputtering system that used a gallium target. Surface morphology and composition were analyzed using both scanning and transmission electron microscopy. Energy-dispersive x-ray spectroscopy and electron energy loss spectroscopy were used to measure the presence of gallium and nitrogen in the resulting nanowires, respectively.

The newly engineered furnace significantly reduced tungsten contamination to below the detectable levels of energy-dispersive x-ray spectroscopy. Gallium nitride nanowires were present on gold-catalyzed samples only in the gold-covered region of the silicon substrate exposed to a gallium flux; these nanowires had diameters between 20 and 30 nm and were hundreds of nanometres in length. Nanowire morphology improved as temperature was elevated, but it did so at the cost of lower areal density. Conversely, platinum-coated samples yielded fewer nanowires than their gold-coated counterparts. (111) silicon samples that had nickel deposited on them displayed the best gallium nitride nanowire growths. They had the best surface morphologies, had negligible oxygen concentrations, and were the most densely populated. Moreover, gallium nitride nanowires grown using nickel were consistently single crystalline and their lengths ranged from hundreds of nanometres to well over a micron.

Acknowledgements

First and foremost, I would like to express my deep gratitude to my supervisors, Dr. Ray LaPierre and Dr. Adrian Kitai. Their leadership, insights, and personal support helped to create a truly inimitable learning experience. I could not have imagined how transformative of an experience my graduate studies would be when I first accepted their offer to perform research.

This research would also not have been possible without the training and assistance of the many professional staff that helped me during the numerous phases of my thesis project. I would like to thank Clealand Berwick, Jim Cleaver, and Martin Wensveen, of the Engineering & Science Machine Shop for their help while designing and fabricating my high-temperature furnace. Next, I would like to acknowledge the staff of the Canadian Centre for Electron Microscopy (CCEM); in particular, I would like to recognize Carmen Andrei, Chris Butcher, Glynis de Silveira, and Steve Koprich for their microscopy expertise, advice, and rich conversations. I would also like to acknowledge Doris Stevanovic and Zhilin Peng for their steadfast efforts to maintain a well-functioning cleanroom within the Centre for Emerging Device Technologies (CEDT) and provide comprehensive help to users of the facilities, such as myself.

My graduate research project could not have been undertaken without funding. For this, I would like to extend thanks to the National Science and Engineering Research Council of Canada, the Ontario provincial government, and the department of engineering physics at McMaster University. I would also like to especially recognize the

NSERC CREATE program in photovoltaics for its contributions and personal support throughout my studies.

My transformation to date would not have been possible without the hands-on mentorship of a few special individuals. I would like to acknowledge Dr. Del Harnish for sharing his incisive thoughts and providing constant encouragement to walk the path less traveled, over the past nine years. Nothing-worthwhile doing has ever been done in a sterile box and without the prospect of failure. Next, I would like to thank Mr. Paul Bates for his candor, willingness to help, and sagacity during our encounters - I continuously reflect and act on our discussions. I cannot begin to enumerate the ways in which you have helped me. I would also like to thank Mr. Mark Chamberlain, Dr. Yossi Feinberg and Mr. Iain Klugman for their personal support and helping me realize my true purpose in life.

Finally, I would like to thank those closest to me in life. To my mother and father, thank you for letting me learn through my own mistakes and supporting me in the many ways that you do. To my partner, thank you for your love and patience over the course of this project, both from close and from afar. I know that it has not always been easy. Yet, it was necessary. It has been a great pleasure to share this period of personal and intellectual growth with you.

"You either learn your way towards writing your own script in life, or you unwittingly become an actor in someone else's script." – JTG

Table of Contents

List of Figures

List of Tables

List of Engineering Drawings

1. Background

1.1 Introduction

In this chapter, an overview of gallium nitride and its applications will be provided in sections 1.2 and 1.3. A brief examination of the major gallium nitride thin film production technologies will be covered in section 1.4. More specifically, hydride vapor phase epitaxy, metal organic vapor phase epitaxy, and molecular beam epitaxy will be introduced in order to provide a context to the competition facing the manufacturing method discussed within this thesis. Section 1.5 will introduce the vapor-liquid-solid approach, a common mechanism used to grow semiconductor nanowires. Finally, the chapter will close with the motivations behind this thesis in section 1.6.

1.2 Gallium Nitride Material Overview

The group III-nitride material system consists of gallium nitride (GaN), indium nitride (InN), and aluminum nitride (AlN)[1]. These direct bandgap materials that span the visible spectrum have demonstrated desirable commercialization properties: the ability to take on both p- and n-type doping profiles, and long device lifetimes[2].

Gallium nitride is a wide bandgap semiconductor material that is increasingly gaining the interest of scientists and engineers. While GaN typically takes a wurtzite crystal structure under ambient conditions, but it can also take a zincblende structure[2-5]. At room temperature, the bandgap of GaN has been shown to be 3.43 eV and 3.3 eV

for its wurtzite and zincblende forms, respectively[6]. GaN devices thus produce 361 nm and 376 nm radiation, corresponding to the blue visible region of the electromagnetic spectrum. Important physical properties of GaN are reviewed in more detail elsewhere[1, 6].

The growth methods that create nitride semiconductors, such as gallium nitride, induce a native n-type conductivity background in these materials[7]. However, the doping of gallium nitride films is typically modulated through the addition of silicon and magnesium atoms[8, 9]. The former causes the semiconductor to become more n-type, while the latter element increases the p-type nature of the film. Silicon impurities create shallow donor states between 22 meV and 42 meV below the conduction band edge when substituting gallium atoms and thus behave as essentially ideal dopants at room temperature[10, 11]. In contrast, p-type doping is much more difficult to achieve with acceptor states being created by magnesium atoms between 130 and 170 meV above the valence band edge[8]. In fact, the inability to introduce p-dopants into GaN was one of the reasons for the slow pace of nitride research in the past. More exotic dopants, such as rare-earth elements, have also been used in nitrides for special purposes[12].

Currently, the manufacturing of gallium nitride films and nanostructures is dominated by MOVPE and MBE methods. GaN nanowires are high-performance, large direct bandgap materials that are traditionally grown using these expensive fabrication technologies. The development of a low-cost, large-area alternative fabrication procedure for GaN nanowires using sputtering is investigated within this thesis. While there has been work done on developing a sputtering-based production method for

gallium nitride nanowires within the literature, these works focus on gallium oxide targets for the group-III source and ammonia as nitrogen sources[13, 14]. The proposed procedure within this thesis uses a reactive DC magnetron sputtering system in a nitrogen environment, elemental gallium targets for the group-III source, and (111) silicon substrates.

1.3 Applications of Gallium Nitride

Although single crystal gallium nitride was first successfully grown in 1970, there was little advancement in terms of devices until over two decades later[15]. Unlike most other semiconductors, such as silicon and III-V materials, heteroepitaxy techniques have historically been more advanced than their bulk crystal growth counterparts. Consequently, one of the major obstacles to growing high-performance III-nitride devices has been the absence of a native substrate to grow on that is both lattice and thermally matched to these materials[16]. The resulting cracking of these heteroepitaxial III-nitride films led to the high defect densities and the debasement of electrical and optical performance[16]. In the case of wurtzite gallium nitride, its *a* and *c* lattice constants, 3.189 angstroms and 5.182 angstroms, have thermal expansion coefficients of 5.59×10^{-6} K^{-1} and 7.75×10^{-6} K^{-1}, respectively[16]; these values differ for the typical substrates for nitride growth: silicon carbide and sapphire. For example, sapphire has *a* and *c* lattice constants of 4.758 angstroms and 12.991 angstroms with corresponding thermal expansion coefficients of 7.5×10^{-6} K^{-1} and 8.5×10^{-6} K^{-1}, respectively[16].

Gallium nitride is a commonly used wide bandgap material for both high-frequency and high-power applications. Examples of these high-power applications include Schottky diodes and power heterostructure field-effect transistors (HFETs)[17-19]. A typical high-frequency application of GaN is its use in conjunction with the ternary alloy aluminum gallium nitride to create high electron mobility transistors (HEMTs)[20, 21]. Other common applications of GaN devices are as light-emitting diodes in the blue/green portion of the electromagnetic spectrum, solid-state lighting when combined with a phosphor coating, photovoltaic cells, laser diodes, and sensing[22-28].

1.4 Thin Film Growth of Gallium Nitride

There are numerous methods of growing nitride thin films and this section will briefly describe the most prevalent methods for growing single crystalline gallium nitride and other III-nitride films: hydride vapor phase epitaxy (HVPE), metal organic vapor phase epitaxy (MOVPE), and molecular beam epitaxy (MBE).

The growth conditions have important effects on the resulting semiconductor crystal quality. High-quality III-nitride crystals require growth temperatures that are routinely in excess of 1000°C due to the dissociation of the nitrogen precursor[29-32]. These elevated temperatures introduce negative consequences, such as increasing nitrogen vapor pressure. In order to facilitate nitride film growth, one compensates the high temperature by using very high V-III ratios and flow rates[33, 34]. These factors in turn have implications on vapor phase transport and flow patterns within the reactor during growth, both of which can affect film stoichiometry and uniformity[35].

The nitrogen sources themselves also play other roles in film growth. The most common nitrogen sources in III-nitride growth are ammonia (NH_3) and diatomic nitrogen gas (N_2)[34]. These gases are quite thermally stable, as evidenced by their correspondingly high bond energies. Moreover, both of these bond energies are higher than those of arsine and phosphine, the common gaseous sources of arsenic and phosphorus in III-V semiconductor deposition, respectively. Ammonia is easier to crack into reactive atomic nitrogen molecules than diatomic nitrogen is and this leads to the creation of either nitrogen-rich and gallium-rich growth conditions during deposition depending on the source gas and method used[36, 37]. In nitrogen-rich situations, such as growths using ammonia, the flux of the group III component (i.e. gallium in this case) determines the growth rate of the semiconductor film[36]. The converse is true in gallium-rich environments.

Hydride vapor phase epitaxy (HVPE) is the preferred method to grow bulk gallium nitride crystals[30, 38]. This method grew in popularity following the successful demonstration of p-type doping in 1989[39]. During HVPE, molten gallium is exposed to hydrogen chloride gas to form volatile chloride compounds (i.e. gallium chloride) that subsequently interact with ammonia to deposit gallium nitride on a substrate that usually has a pre-deposited nucleation layer of GaN, AlN, or zinc oxide[38, 40]. Typical growth temperatures for this technique are in the vicinity of 1000°C[29, 30, 41].

The main advantage of HVPE is the ability to deposit single crystal GaN at high rates, often in the 100s of microns per hour[29, 42]. Following deposition, if necessary, there are a host of processes to remove the epilayer from a foreign substrate. These

aspects have spurred great interest in the scientific community about developing large-area deposition systems for gallium nitride and other III-nitrides. Market reports indicate that industry is also moving towards larger wafer sizes. According to Lux Research, four-inch epitaxially grown wafers will peak at sales of $2.1 billion in 2017 and industry will transition to six-inch wafers, which are expected to fetch $1.4 billion in sales in 2020[43].

Like any technology still under development, there are shortcomings to hydride vapor phase epitaxy. Of particular relevance to gallium nitride nanostructure growth, is that the high deposition rates come at the cost of the ability to create abrupt junctions, thereby precluding the semiconductor device designers from creating certain devices and intricate heterostructures. A more detailed review of HVPE for nitride semiconductors can be found elsewhere[40, 44].

Another common technique for growing group-III nitride thin films is metal organic vapor phase epitaxy. MOVPE has been the dominant industry technology for manufacturing group III-nitride devices and films since the 1990s. This process employs gaseous alkyl metal precursors for group-III elements, such as trimethylgallium in the case of gallium, and ammonia as its nitrogen source[45, 46]. During a typical epitaxial growth run, the source gases are fed into the reactor in a segregated manner to avoid parasitic reactions. Gallium nitride is deposited through the group-III alkyl species undergoing thermal decomposition on top of the heated substrate and the cracking of ammonia at high temperatures. Interestingly, only a few percent of the ammonia gas undergoes pyrolysis at 1000°C[47]. Considerable V/III ratios, typically in excess of 1000,

are a prerequisite of high-quality nitride MOVPE due to this low conversion rate[48-50]. The large oversupply of ammonia necessary for growth is a leading source of impurity incorporation in nitride film; it allow requires ventilation systems capable of handling the high throughput.

That being said, MOVPE has a number of advantages, including the ability to readily produce both p-type and n-type gallium nitride, and abrupt semiconductor structures, such as quantum wells and dots[32, 51, 52]. The latter makes it a preferred growth technique for gallium nitride-based devices, such as LEDs and transistors[31, 53, 54]. The ability to effortlessly scale to multiple wafer depositions greatly facilitates the industrial use of MOVPE.

The last major semiconductor production technology to be discussed is molecular beam epitaxy (MBE). In the case of gallium nitride films, there are two variations of the MBE technique: ammonia-MBE and plasma-assisted MBE[55]. Both setups operate under ultrahigh vacuum (UHV), deposit at rates of 1 micron per hour or slower, and typically use solid source effusion cells for group-III components, such as gallium, indium, and aluminum; but they differ with respect to their group V source[55].

Ammonia MBE systems use ammonia as its nitrogen source as one would imagine. They operate in N-rich regimes and temperature ranges around 860°C – 920°C[56]. Special trapping and pumping components are integrated into these systems to maintain UHV conditions amidst ammonia injection. Conversely, MBE systems that use nitrogen as its group-V source require a RF plasma to crack the nitrogen gas into much more reactive atomic nitrogen particles since nitrogen possesses a very high

thermal stability[57]. In fact, plasma-assisted setups are the much more common type of III-nitride MBE system today and allow one to explore both Ga-rich and N-rich environments[36]. Plasma-assisted MBE growth of gallium nitride typically occurs at lower temperatures than ammonia-based MBE, typically in the neighbourhood of 550°C to 850°C[37, 57-59]. MBE is particularly well-suited to nitride semiconductor crystal growth and surface investigations since the UHV environment allows researchers to use high precision electron beam *in situ* monitoring techniques, such as reflection high-energy electron diffraction (RHEED). Other advantages of MBE-based nitride growth include the ability to create abrupt junction doping profiles and grow at lower temperatures than nitride HVPE and MOVPE techniques[36].

1.5 Vapor-Liquid Solid Growth of Nanowires

The vapor-liquid-solid (or VLS) mechanism was first proposed by Wagner and Ellis at Bell Telephone Laboratories in 1964 as an explanation for the epitaxial growth of their silicon microwhiskers. They observed that these structures required an impurity particle at their tips, such as gold, to grow and would do so until the impurity was consumed[60]. Wagner and Ellis also contended that the selection of a catalyst for VLS growth was not arbitrary, and that one must consider a multitude of factors, such as whether or not the droplet alloy would become molten at the deposition temperature and interfacial energies of the substrate, vapor reactants, and impurity droplet[60]. Considerable research on the VLS mechanism has been performed since the pioneering work by Wagner and Ellis to extend our understanding of it in group IV, III-V, and II-VI

semiconductor material systems[61-64]. Over time, the VLS method's ability to preferentially direct anisotropic crystal growth has attracted the interest of semiconductor engineers looking to create novel, high-aspect ratio materials and devices.

Understanding the VLS method requires the consideration of how a sample is prepared. Conventionally, a thin layer of metal is deposited on a clean semiconductor substrate. The sample is subsequently annealed in the growth chamber under vacuum causing the metal layer to alloy with the substrate and form liquid droplets on the substrate surface. During growth, these particles function as collection centres (also called sinks) for impinging vapor-phase growth species[65].

In the case of VLS grown gallium nitride nanowires, nickel is a frequently used seed particle (but by no means the exclusive catalyst), as are gallium and ammonia as source materials[66]. While under a flux of growth species, the concentration of the group-III and group-V constituents increases within the droplet until a critical level of supersaturation is reached. At this point, there is a high probability that a stable nucleus will form at the vapor-liquid-solid interface, and once formed, growth material will be quickly precipitated from the droplet to complete a single III-V bilayer beneath the entire droplet[67, 68]. As a result, the nanowire crystal assumes the diameter of the droplet and grows in a layer-by-layer fashion for the length of time that the growth species are supplied. The crystallographic growth direction of the one-dimensional nanowire structure corresponds to the direction of the lowest nucleation barrier[69]. For example, zincblende semiconductor nanowires, such as gallium arsenide and silicon,

tend to nucleate along the <111> direction[70]. The VLS process is illustrated in Figure 1.1.

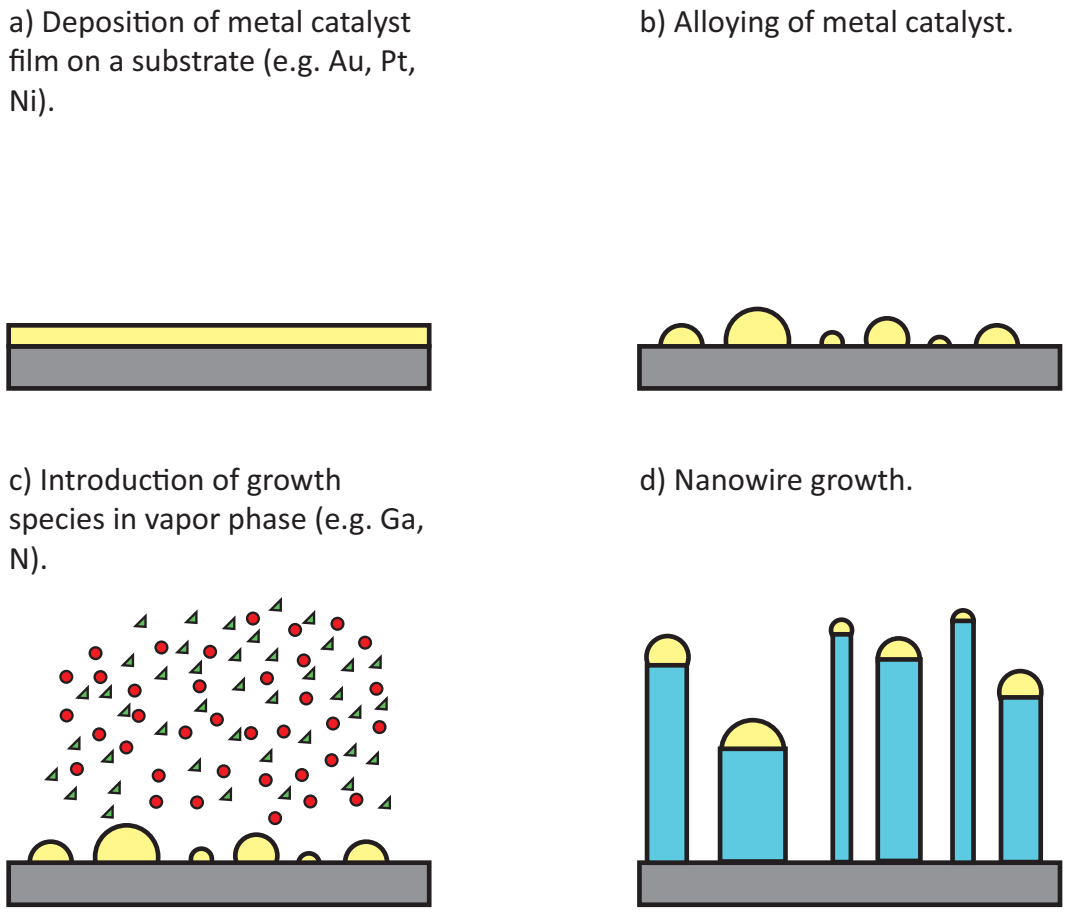

Figure 1.1: The Vapor-Liquid-Solid Process.

There are some additional remarks worth mentioning about the catalyst droplets used during the VLS growth of semiconductor nanowires. While there is an abundance of research utilizing metallic catalysts as seed particles to grow semiconductor nanowires, the process is not restricted to them. In fact, there is increasing interest in growing semiconductor nanowires using the group-III component as a self-catalyst; for example, gallium would be pre-deposited as a self-catalyst for gallium arsenide nanowires[71]. The primary motivation for this is to integrate high-

performance III-V nanostructures onto conventional VLSI silicon technology without the debasement of electronic and optical properties of the device by a catalyst, such as gold[71].

Nanowires expand the design possibilities for semiconductor device engineers. Nanowires enable engineers to construct devices in both the axial (along the VLS growth direction) and radial (perpendicular to VLS growth) directions by varying growth conditions. Axial growth of nanowire homojunctions or heterojunctions is essentially the straightforward application of the VLS method with the additional requirement of introducing different source constituents to be incorporated during growth in a controlled manner[70, 71]. Radial growth of nanowires (also known as shell growth) arises when growth conditions are changed to favour the conformal deposition of vapor phase reactants onto the solid nanowire surface[72, 73]. This growth process is called vapor-solid (VS) growth. Considerable flexibility over the desired shell composition is allowed through varying source reactants, dopants, growth temperature, and V/III ratio[72-74]. Moreover, the thickness of the shell can be scaled with deposition time. The combination of these two growth modes enables the epitaxial growth of three-dimensional semiconductor devices.

1.6 Overview of Thesis

Herein, this thesis consists of four chapters and an appendix. All experimental methods are detailed in chapter two. Chapter three examines the production and testing of three high-temperature furnace designs. Chapter four elaborates on the

different gallium nitride nanowire experiments conducted over the course of this thesis. Chapter five provides concluding remarks and suggestions for future work on this project. Finally, the appendix section contains engineering drawings and assembly instructions for the different furnace designs.

2. Experimental Methods

2.1 Introduction

In this chapter, an overview of the experimental methods used during the course of this thesis will be described. Section 2.2 provides an overview of reactive DC magnetron sputtering and how it was used to create samples. Section 2.3 details how substrate samples were prepared before and after deposition. The procedure and parameters for a typical sample growth are then elaborated on in section 2.4. Finally, sections 2.5 and 2.6 describe the scanning electron microscopy and transmission electron microscopy techniques that were used to examine the resulting samples, respectively.

2.2 Reactive DC Magnetron Sputtering

2.2.1 Sputtering Overview

Sputtering is a physical vapor deposition method that allows one to deposit almost any material conformally over large areas. The underlying principles of sputtering are most easily understood through examining its simplest configuration. DC (or diode) sputtering utilizes a parallel plate setup under vacuum, in which the target source and the substrate to be deposited on are positioned on the cathode and anode plates, respectively. The target is placed under a negative bias, usually ranging from

hundreds of volts (V) to several kilovolts (kV), while the anode's potential is either grounded or varied. DC sputtering systems are typically operated at pressures of a few hundred milliTorr (mTorr) and use argon (Ar) as the working gas. Deposition of thin films through sputtering involves the condensation of material that was ejected (or sputtered) from a target material on the cathode through the impingement of energetic ions. During operation, a sputtering system relies on the creation of a quasi-neutral gas containing ions, electrons, and neutral species called a plasma between the electrodes to generate and sustain these ion-induced ejections of material. The process begins spontaneously under vacuum when a cosmic ray or ultraviolet light causes the initial ionization event and the ensuing collision cascade between working gas atoms/ions (i.e. Ar and Ar^+), target atoms, and secondary electrons creates a self-sustaining plasma under the appropriate deposition system conditions. Ions collide with the target source and sputter a vapor of target atoms that deposits on the substrate residing on the anode. Not all incident ions result in sputtered atoms. The ratio of sputtered atoms from the target to incident ions is referred to as the sputtering yield.

While DC sputtering is the easiest method to understand, it is not widely used in industry due to its relatively slow deposition rates and high working pressures. The dominant method used in the production of thin films and coatings is magnetron sputtering. These systems have many advantages over DC and RF sputtering configurations, including fast deposition rates, denser coatings, reduced working pressures (on the order of a few mTorr), and lower required voltages for operation. Although there are numerous designs for magnetrons, all implementations have

magnets configured in geometries such that the resulting magnetic field is orthogonal to the electric field that is used to accelerate ions into the target. The orientations of these fields give rise to a Lorentz force that confines electrons to a cycloidal hopping motion close to the cathode's surface. This confinement of electrons increases the viability of the plasma at lower pressures by increasing the probability of an ionizing electron-atom collision occuring and allows sputtered atoms to travel in more of a ballistic-like manner to the substrate. A typical annular design of a DC magnetron is shown in Figure 2.1. This type of magnetron corresponds to the type used during experiments for this thesis.

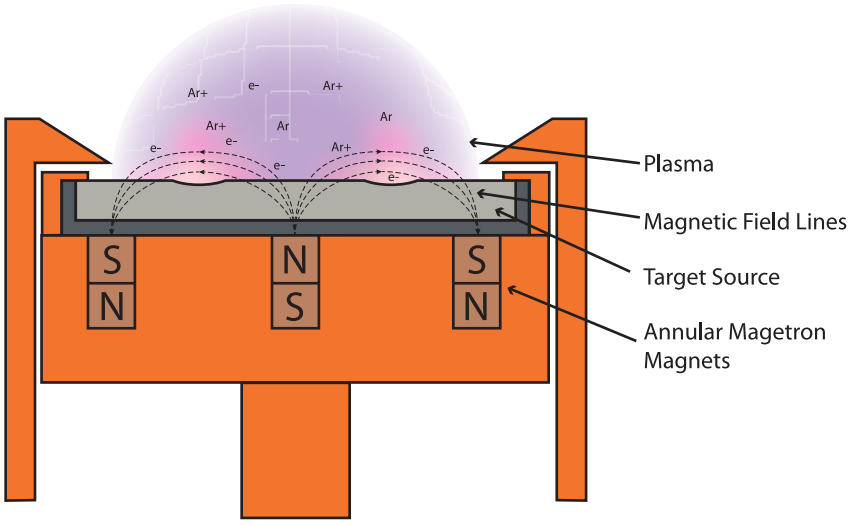

Figure 2.1: Typical Design of Annular DC Magnetron.

Reactive sputtering systems introduce a reactive gas, such as oxygen or nitrogen, into the chamber in addition to the working gas. The purpose of introducing these additional gases is for them to react with the sputtered materials in the formation of the film deposited on the substrate. This is a common approach to growing oxide and nitride thin films.

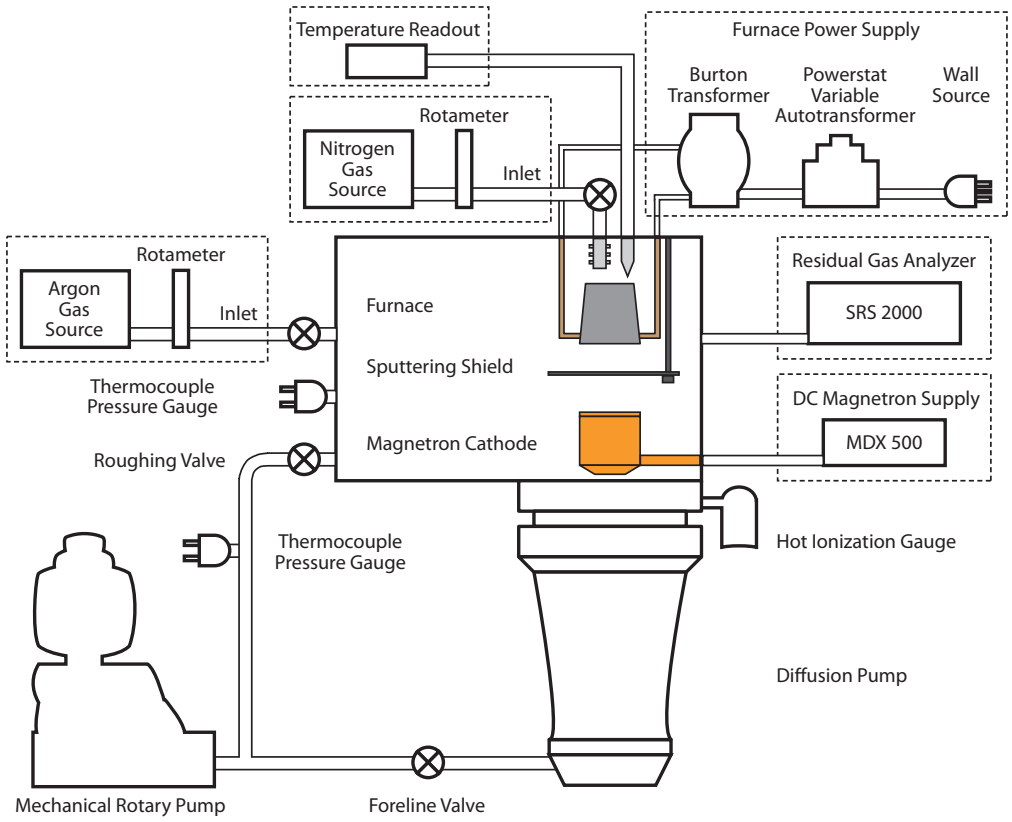

Figure 2.2: Schematic of Sputtering System.

2.2.2 Reactive DC Magnetron Sputtering Deposition System

The deposition system used during the experiments for this thesis was a customized setup for group III - nitride semiconductor films, in particular gallium nitride. The main

stainless steel cylindrical chamber was approximately 71 cm in diameter and 26 cm tall. This structure contained inlets for gases (i.e. argon and nitrogen), ports for measuring equipment, and a connection to a SRS 2000 residual gas analyzer. The chamber's vacuum system primarily consisted of a diffusion pump situated below a cold water trap. A single mechanical rotary pump was used to both pump down the main chamber and back the diffusion pump. Pressure measurements above 10^{-3} Torr were performed using thermocouple gauges situated in the chamber and roughing lines, and by a Pirani gauge. A Bayard – Alpert ionization gauge was used to read pressures below 10^{-3} Torr. Temperature was monitored using a Type-K thermocouple and read out using an Omega 4002-KC Reader. Flow of nitrogen and argon gases into the chamber was regulated through the use of Matheson rotameters. The group-III source was an elemental gallium target produced by melting 99.999% pure gallium ingots from Alfa Aesar. Finally, an Onyx-2 magnetron cathode from Angstrom Sciences and an Advanced Energy MDX 500 DC power supply were used to create a plasma during the sputtering process. The substrate was heated using Joule heating. The exact geometry and materials used during heating is described in further depth in Chapter 3. Figure 2.2 depicts a simplified schematic of this system and its components.

During a typical growth, the main chamber was initially pumped down from atmospheric pressure to about 5×10^{-2} Torr using the rotary pump then the diffusion pump was used to evacuate the chamber further. The chamber was then allowed to pump down for a minimum of five hours. The vacuum system at its best could not evacuate below 1.0×10^{-5} Torr. Gases were introduced towards the end of the sample

heating process. The graphs in Figure 2.3 show the calibration curves for nitrogen and argon from the manufacturers of the rotameters.

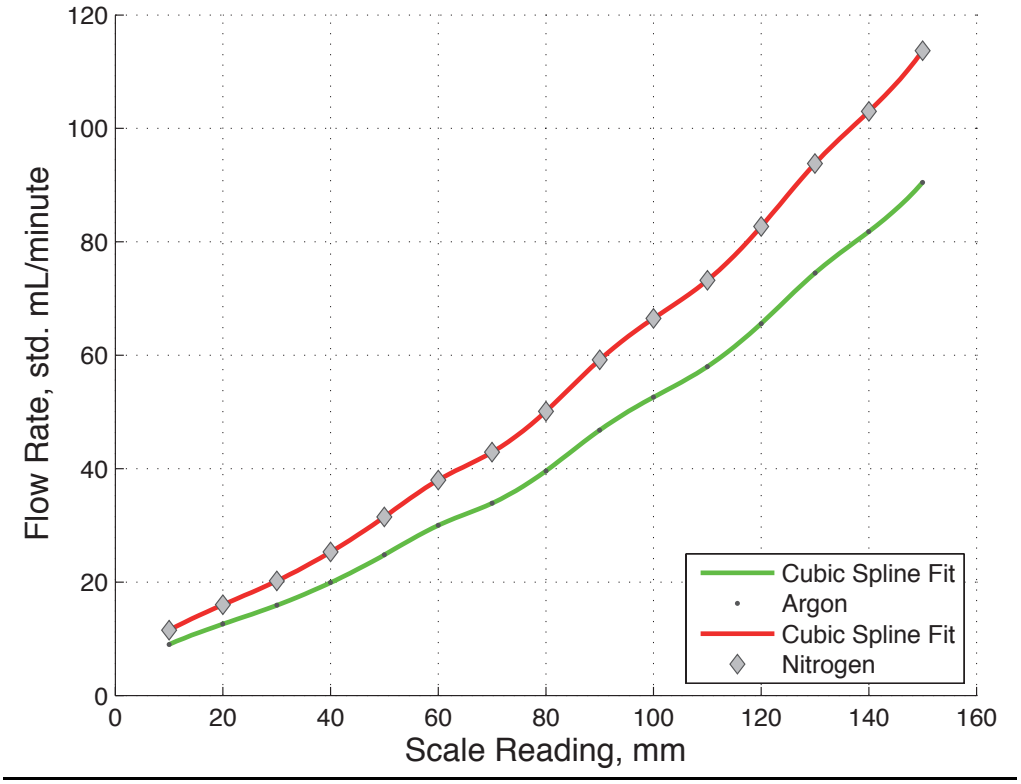

Figure 2.3: Gas Calibration Charts. This figure shows the Matheson rotameter calibration curves for argon and nitrogen.

2.3 Sample Preparation

2.3.1 Initial Sample Preparation

Substrate samples began as standard three-inch (111) silicon wafers. After the wafer was removed from its packaging, a thin layer of Shipley S1808 photoresist was applied to it in order to minimize possible damage and contamination during subsequent processing. Following a typical baking procedure, a silicon wafer was

mechanically cut using a Microace 3 dicing saw into smaller square samples. These square samples were oriented so that their sides were either perpendicular or parallel to the major flat marker on the wafer. Initially, samples were cut into 7 mm x 7mm squares to fit into the original sample holder, but they were enlarged to 16 mm x 16 mm squares in subsequent furnace designs.

Following the dicing procedure, the photoresist layer was removed within the Centre for Emerging Device Technologies' class 10000 cleanroom. Each square was subjected to three 10 minute rinses under sonication: one in semiconductor grade acetone, one in semiconductor grade methanol, and one in deionized water. The substrate samples were also rinsed in deionized water between the acetone and methanol rinses and dried using a pressurized nitrogen gun. A sacrificial oxide layer was then grown on substrate samples through a 20-minute ultraviolet (UV) ozone treatment. This oxide layer was then removed using a one minute buffered hydrogen fluoride (BHF) dip before metallization. The sample was rinsed in deionized water for one minute, dried under nitrogen, and then immediately loaded in the metal evaporation system within the cleanroom. Minimizing exposure to oxygen prior to metal deposition was a priority, as the formation of a thermal silicon oxide layer would catastrophically affect VLS growth.

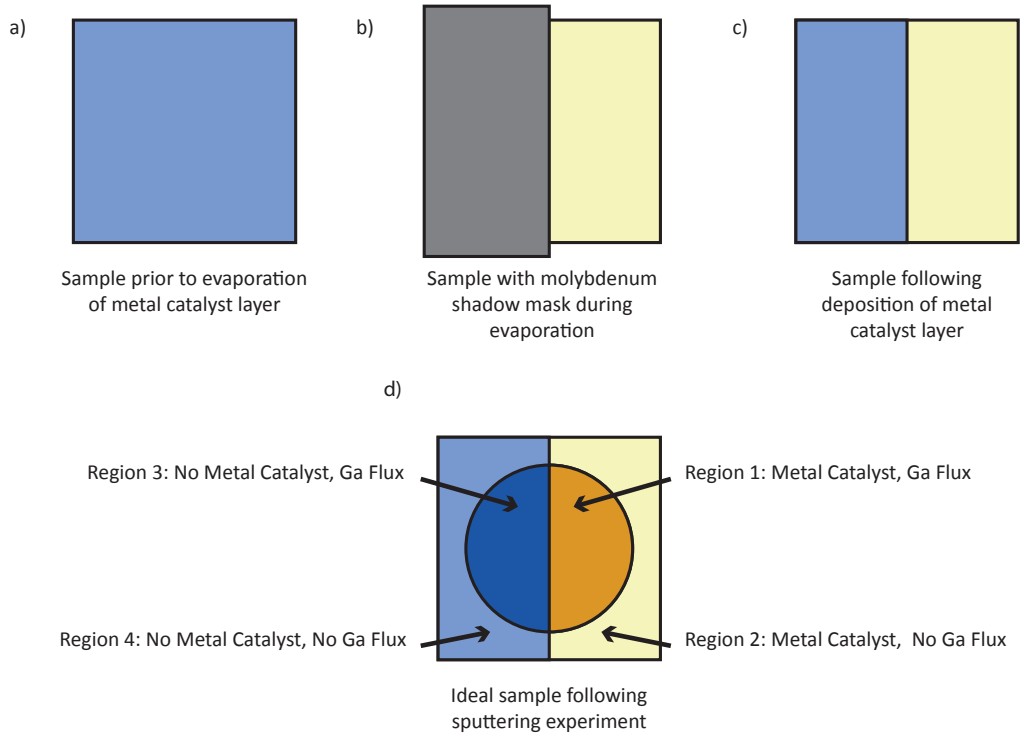

Figure 2.4: Sample Preparation and Resulting Experimental Regions.

2.3.2 Deposition of Catalysts

All metal catalysts were deposited on substrate samples using electron beam evaporation under high vacuum. Substrate samples rotated slowly in the chamber while one to four nanometers (nm) of gold (Au), platinum (Pt), or nickel (Ni) were deposited on their surfaces. Metal atoms were deposited across an entire sample, except in areas masked by the clip holding a sample in place.

This procedure was modified once the new furnace designs were installed within the sputtering system in order to increase experimental throughput. Half of the 16 mm x 16 mm (111) Si samples were covered by a molybdenum shadow mask during

deposition in order to create distinct regions with and without metal catalysts. This partition in combination with the circular aperture on which the sample sat during deposition in the sputtering chamber gave rise to four experimental regions that could be studied during a single growth: 1) metal catalyst exposed to the gallium flux, 2) metal catalyst shadowed from the gallium flux, 3) no metal catalyst exposed to the gallium flux, and 4) no metal catalyst and shadowed from the gallium flux. Figure 2.4 illustrates these demarcated areas.

Once the metal catalyst layer was deposited, the sample was quickly transferred and loaded into the furnace within the sputtering system and the chamber was subsequently evacuated. Samples that were not immediately loaded into the chamber were subjected to one-minute HF dip to remove any surface oxide and rinsed in deionized water at a later date before being loaded into the sputtering system.

2.3.3 Sample Preparation for Microscopy

Samples were not modified or disturbed prior to examination using scanning electron microscopy. They were securely mounted on an available electron beam lithography stub using clips and then imaged. If samples proved to possess GaN nanowires, these nanowires were removed by mechanically scrapping a standard holey (copper mesh) transmission electron microscopy (TEM) grid over the appropriate region. This method was found to be the most effective in isolating GaN nanowires for TEM analysis.

2.4 Sample Growth

2.4.1 Growth Parameters

Over the course of this thesis, a large number of growth conditions were investigated across 46 experiments to determine if they led to the production of gallium nitride nanowires via sputtering. This parameter space included: growth temperature (or its surrogate of furnace input power), the presence of a metal catalyst, the type of metal catalyst, the amount of catalyst deposited, magnetron cathode power, and deposition time. Table 2.1 summarizes a breakdown of these growth conditions. A more detailed discussion is be pursued in later chapters on the experimental results.

Substrate	(111) Si
Growth Temperature	700C - 900C
Presence of Catalyst	Yes or No
Catalyst Type	Au, Pt, or Ni
Catalyst Thickness	1 nm, 2 nm, or 4 nm
Magnetron Cathode Power	65 W to 100 W
Deposition Time	Varies

Table 2.1: Experimental Growth Conditions Summary.

The choice of catalyst for these experiments was based on literature concerning the growth of gallium nitride nanowires by MOCVD and MBE[75-77]. Initially, Au was used due to its popularity; however, poor results led to experimentation with Pt and Ni as well. The initial growth conditions used were adapted from previous gallium nitride thin film work of Harris Shen, a doctoral candidate within Dr. Kitai's research group.

Changes in furnace design also played a role in the growth of GaN nanowires; the control of nitrogen and argon flow played a more minor role due to the resolution of the rotameters used.

2.4.2 Growth Procedure

This section describes the growth procedure for a typical deposition run. Some of the settings may differ between experiments as they were intentionally modified to investigate a specific condition setting. The growth procedure, in particular the ramping of temperature within the furnace, was changed between initial experiments with the original furnace and those conducted with the newly engineered models in order to prevent damage to the equipment.

There were numerous revisions to the furnace during the course of this thesis. The growth procedure is best explained for the newer furnaces first since the method used for the original furnace is a simplification of it. Moreover, the deposition method remained consistent amongst all subsequent furnace models. Following the evacuation of the sputtering chamber to a pressure in the low 10^{-5} Torr range, the variable autotransformer was engaged and slowly ramped to the desired setting (as a percentage of input voltage from the wall). This ramping corresponded to increasing the temperature of the sputtering furnace. For every 10% increase in voltage, the furnace was allowed to sit for 10 minutes at this temperature and approach thermal equilibrium. As this process progressed, the temperature of the furnace would reach between 750°C and 800°C; argon gas was then let into the chamber until its rotameter read “80”. At this time, the magnetron cathode was turned on in order to pre-sputter

the surface of the gallium target before growth. This pre-sputtering process was performed for 15 minutes at a cathode power setting of 70 W. Once this pre-sputtering process was completed, nitrogen gas (at a rotameter setting of 110-130) was allowed to enter the chamber from above the furnace. The temperature reading was then allowed to stabilize to equilibrium, the working pressure of the chamber was adjusted to between 10-to-20 mTorr (ideally 15 mTorr) on the Pirani gauge, and the magnetron power was increased. Once these actions were completed, the sputtering shield was then rotated to the open position and the substrate underwent deposition for a set time. Upon completion of the growth, the DC magnetron power supply was immediately turned off, and then the autotransformer was wound down quickly to the 0% setting. The argon gas was turned off and the sample was allowed to cool in nitrogen until the furnace temperature was below 100°C. In the case of the original furnace, there were no breaks when ramping the voltage with the autotransformer: the dial was immediately wound to 100% and then the temperature of the furnace was allowed to equilibrate.

2.5 Scanning Electron Microscopy

2.5.1 Scanning Electron Microscopy Imaging

Scanning electron microscopy (SEM) was performed in order to examine the resulting surface morphologies of the deposited films and ascertain whether or not a growth condition modification gave rise to gallium nitride nanowires. All scanning

electron microscopy was performed using the JEOL 7000F SEM within the Canadian Centre for Electron Microscopy at McMaster University.

A typical SEM operates under vacuum and comprises of an electron source, an anode plate, a number of electromagnetic lenses, and a detection system. Only a small portion of the electrons generated by thermionic or field emission in the upper electron column pass through a hole in the anode plate on its way to the electron lenses. Initially, the condenser lens demagnifies the incident beam and sets both the minimum beam size and available beam current, then the objective lens is used to focus the diameter of the incident electron beam on the surface of the sample where an interaction volume is created. The scanning coils within the column allow the incident electron beam to be rastered across the sample while electrons and photons are collected by a detection system and the image is reconstructed pixel-by-pixel for the operator.

SEM imaging is made possible through incident electrons undergoing both elastic and inelastic collisions when they impinge on surface and bulk atoms during the rastering process. These collisions occur within what is termed the interaction volume and the depth that the beam penetrates is proportional to the accelerating voltage used by the electron source. This probing of the substrate gives rise to many different signals that can be detected: Auger electrons, secondary electrons, backscattered electrons, and a variety of X-rays. The interaction volume and some of these signals are shown in Figure 2.5. SEM was used during this thesis to investigate the surface topography of a sample following sputtering. As such, secondary electrons were of interest since they are produced near the surface and provide information on this aspect. An accelerating

voltage of 3-8 kV and a small probe current setting were used while imaging, except in very few circumstances.

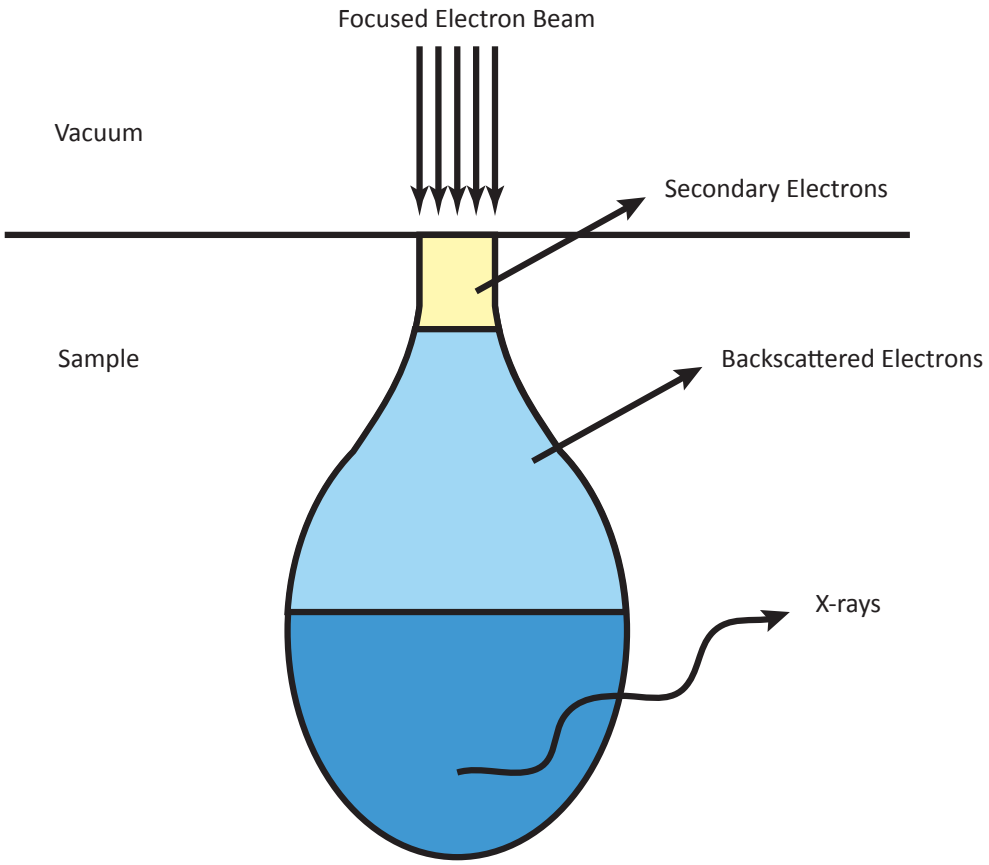

Figure 2.5: SEM Interaction Volume.

2.5.2 Energy-Dispersive X-ray Spectroscopy

Understanding the chemical composition of the resulting films and nanowires was also a concern during this thesis. In particular, identifying the presence of gallium, nitrogen, catalysts, and any contaminants was useful in determining the success of a growth experiment and / or furnace design. Qualitative compositional analysis was

performed by energy-dispersive x-ray spectroscopy (EDS or EDX) at accelerating voltages of 10-15 kV while using the JEOL 7000F scanning electron microscope at the Canadian Centre for Electron Microscopy. All results were interpreted using Oxford Instruments' INCA software. EDS on the JEOL 7000F was used as a preliminary screening technique for samples. More detailed x-ray analysis of suitable samples was performed on the JEOL 2010 transmission electron microscope in the Canadian Centre for Electron Microscopy (CCEM).

EDS is a localized chemical analysis technique. In the case of the JEOL 7000F, incident electrons are used to induce x-ray excitation within a sample. As mentioned previously, higher accelerating voltages of electrons generated by the source provide electrons with a higher kinetic energy and this allows them to penetrate deeper into the specimen and generate characteristic x-ray photons. Characteristic x-rays arise from the discrete energy levels available for electrons within an atom. Electrons with large kinetic energies collide with elements within a material and promote tightly bound, inner shell electrons, leaving vacancies to be filled. Outer shell electrons of higher energy fill these holes and release x-ray photons with energies corresponding to the transition between these two shells. Moreover, these transition energies between shells are distinct for different elements and are used to identify their presence within a sample. The emitted x-rays are read out by a detector and converted into a voltage pulse that is proportional to the energy of the detected photon. The elemental composition of an area of the specimen can be probed as the electron beam rasters over the sample.

2.6 Transmission Electron Microscopy

2.6.1 Transmission Electron Microscopy Imaging

Transmission electron microscopy (TEM) was performed to investigate the surface geometry, elemental composition, and crystal structure of the gallium nitride nanowires grown by DC reactive sputtering. All transmission electron microscopy was performed using the JEOL 2010 transmission electron microscope within the Canadian Centre for Electron Microscopy.

TEM is an excellent means to structurally image thin samples, such as thin films and nanowires at high magnifications. The components of a TEM are similar to those in a SEM; there is an electron gun (a field source in the case of the JEOL 2010), electromagnetic lenses, apertures to control the spot size on the sample, and a detection system capable of reading out different signals. However, the accelerating voltages of the primary electrons are typically at much higher voltages in a TEM than those used in SEM, usually in the 100s of kV. During imaging, electrons are projected onto the sample where they undergo scattering. The different types and degrees of scattering provide one with different signals to measure and create a TEM micrograph. Firstly, incident electrons can undergo elastic and inelastic scattering within the sample. Elastic electron scattering, which involves no kinetic energy loss, allows one to investigate a specimen's crystal structure through the creation of diffraction patterns, whereas the latter type allows one to probe spatial variations in crystal composition and perform different types of spectroscopy.

Bright-field and dark-field imaging differ by how the electron beam is processed once it passes through a thin sample. During bright-field imaging, the aperture is positioned within the back focal plane so that only the central beam is allowed through. Consequently, thinner areas that cause less scattering appear brighter in a bright-field TEM image, while regions that are thicker or consist of heavy elements appear darker. On the other hand, dark-field imaging involves using the aperture to block the central electron beam while selecting for a scattered (diffracted) beam. Here, heavier elements and thicker regions appear brighter since it is more probable for electrons to scatter away from the direct beam at wide angles or undergo backscattering. When an annular dark-field detector is employed to collect scattered electrons, in particular those scattered incoherently at very high angles, one can resolve even subtle variations in the Z-ratio quite well. When this technique is performed on a scanning transmission electron microscope, it is called high-angle annular dark-field (HAADF) imaging.

2.6.2 Selective Area Diffraction

Selective Area Diffraction (SAD) was performed on individual nanowires isolated on the copper grids to gain structural information (i.e. crystallographic growth direction and crystal structure) about them.

2.6.3 Electron Energy Loss Spectroscopy

Electron energy loss spectroscopy (or EELS) was used to perform compositional analysis on isolated nanostructures. This technique was chosen due to its sensitivity to measure elements with lighter atomic ratios (Z), such as nitrogen. EELS examines the

loss of kinetic energy that electrons experience while undergoing inelastic scattering as they pass through a TEM sample. These electrons were bombarded onto the sample with a well-defined energy range and the resulting energy losses measured by a spectrometer correspond to well understood loss-mechanisms, such as plasmons and inner shell ionization, that were used to identify individual elements within a sample.

2.6.4 Energy Dispersive X-ray Spectroscopy

EDS measurements were performed in the TEM to determine the chemical makeup of isolated nanostructures. It was performed as a complimentary measurement to EELS since EDS is more sensitive to elements with higher Z, such as gallium, nickel, and gold. Furthermore, EDS measurements made in the JEOL 2010 allowed the spatial distribution of different elements to be mapped over the nanostructure in the absence of a substrate.

3. Motivational Experiments and Furnace Design

3.1 Introduction

In this chapter, initial nanowire experiments and the development of better growth furnaces is discussed. Section 3.2 describes the original furnace and the growth experiments performed using it. Section 3.3 explores the different furnace models designed and manufactured with gallium nitride nanowire growth in mind. The chapter then closes with a discussion of the performance of the different furnace designs with respect to critical design objectives in section 3.4.

3.2 Initial Experiments with Original Furnace

3.2.1 Original Furnace Overview

The original substrate heater, Figure 3.1, was designed and created by Harris Shen, a doctoral candidate within Dr. Adrian Kitai's research group, prior to the commencement of this thesis. In this design, a closed circuit was created between a central tungsten heating coil within the deposition chamber and the exterior input transformer by connecting the tungsten filament to two 3/16" diameter copper rods using two screw-mounted 1/2" diameter stainless steel cylindrical mounts. This arrangement carried current into the growth chamber where it was dissipated across the tungsten filament because of its higher electrical resistance. The filament also

served as a structural support for a cylindrical alumina crucible. This central crucible possessed coincident horizontal slots in its walls. The sample holder, Figure 3.2, with the substrate itself oriented downwards, was inserted into these grooves and held in position during a growth. Nitrogen gas and the argon/gallium vapor flux diffused towards the sample through vertical circular holes on the top and bottom of the crucible, respectively. A type-K thermocouple was also fed in through the top hole. The final feature of this design was a custom-made molybdenum shield positioned below the substrate heater and above the DC magnetron unit. This shield functioned to prevent blackbody radiation that was generated during the Joule heating of the tungsten filament from damaging the gallium target below. It consisted of a central aperture through which the argon/gallium flux was directed towards the downward-facing substrate, and two smaller holes that were used for mounting the shield to the aforementioned stainless steel mounts.

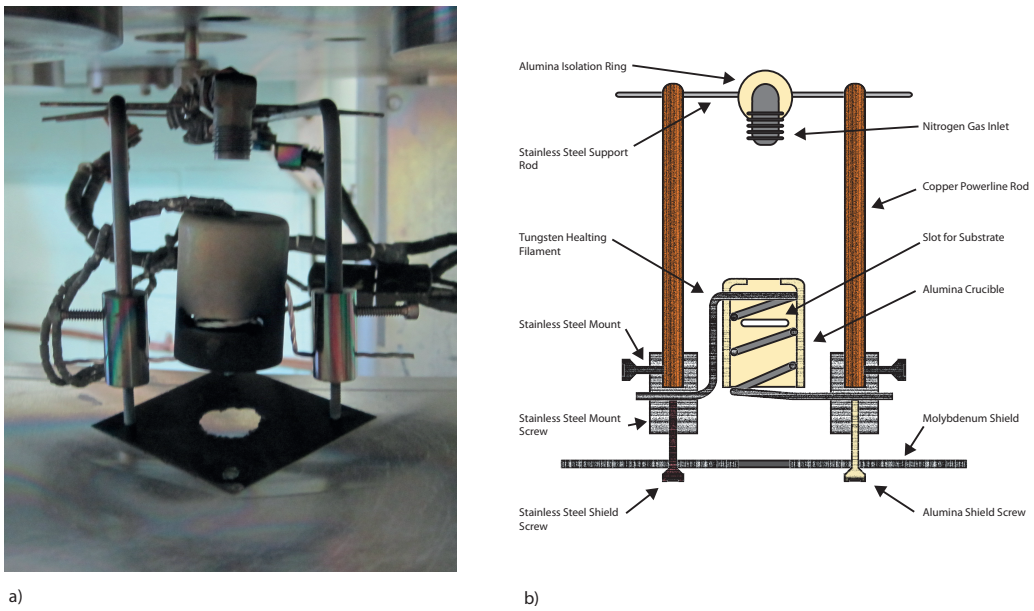

Figure 3.1: a) Original furnace design. b) Simplified cross-sectional diagram of original furnace (not-to-scale).

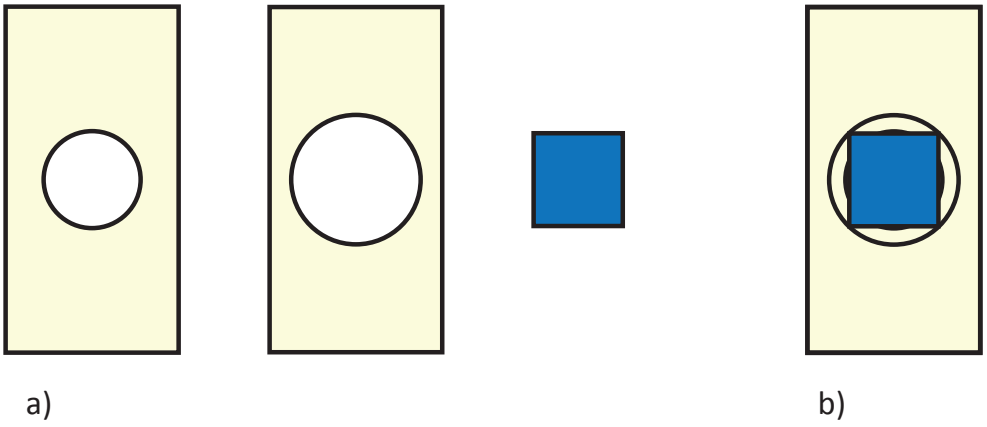

Figure 3.2: a) Components of original substrate holder. From left-to-right: bottom alumina plate, top alumina plate, substrate (facing downwards). b) Assembled original substrate holder.

3.2.2 Initial Nanowire Experiments

The deposition system settings used for the beginning growth experiments were adopted from the gallium nitride thin film studies of Harris Shen, a doctoral student within the Kitai group. These system settings involved using a working pressure during sputtering of approximately 13 mTorr and argon and nitrogen flow rates corresponding to about 19.1 std mL/minute and 47.9 std mL/minute, respectively, and corresponded to an empirical thin film growth rate on the order of two microns per hour. The initial experiments of this thesis comprised of four 7 mm x 7 mm square (111) silicon samples, each having 1 nm of gold conformally deposited across its surface. The input power settings were set to their maximum values for all four of these experiments, resulting in a measured substrate temperature ranging between 667°C and 700°C for three of the four samples and an anomalous reading for the other as discussed below. All nanowire growths were 15 minutes in duration.

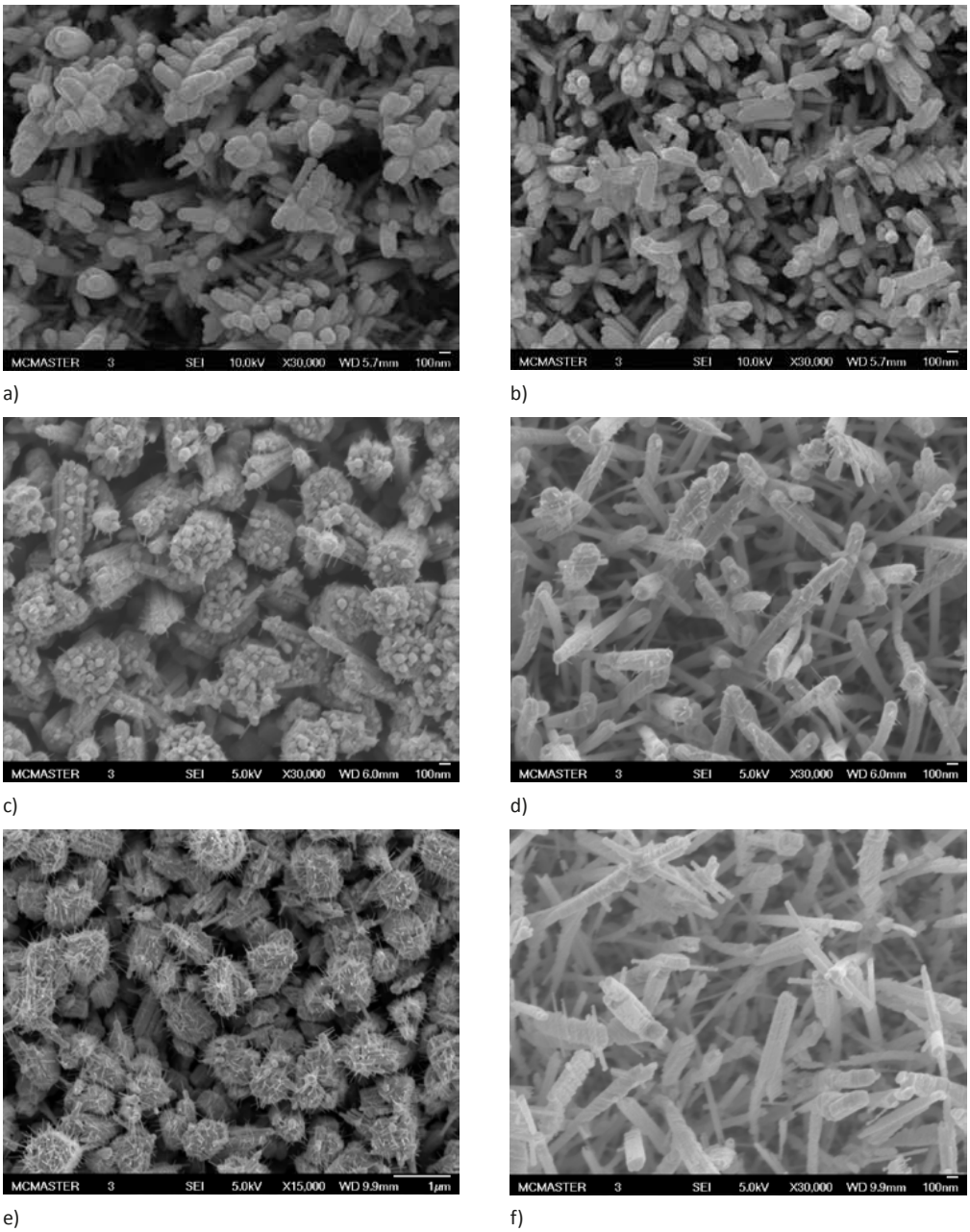

Figure 3.3: SEM images resulting from a series of 15-minute nanowire growth experiments that used a 1 nm gold catalyst layer. Figures 3.3a and 3.3b show representative surface structures from the centre and edge regions of a substrate grown at 700°C, respectively. Figures 3.3c and 3.3d illustrate characteristic structures found at the centre and edge regions of a substrate grown at 667°C, respectively. Finally, figures 3.3e and 3.3f depict typical surface morphologies from the centre and edge regions of a

substrate grown at 692°C, respectively. All images are tilted at 0°. Figure 3.3e is shown at 15000X magnification instead of 30000X magnification because no images were taken of this region at 30000X.

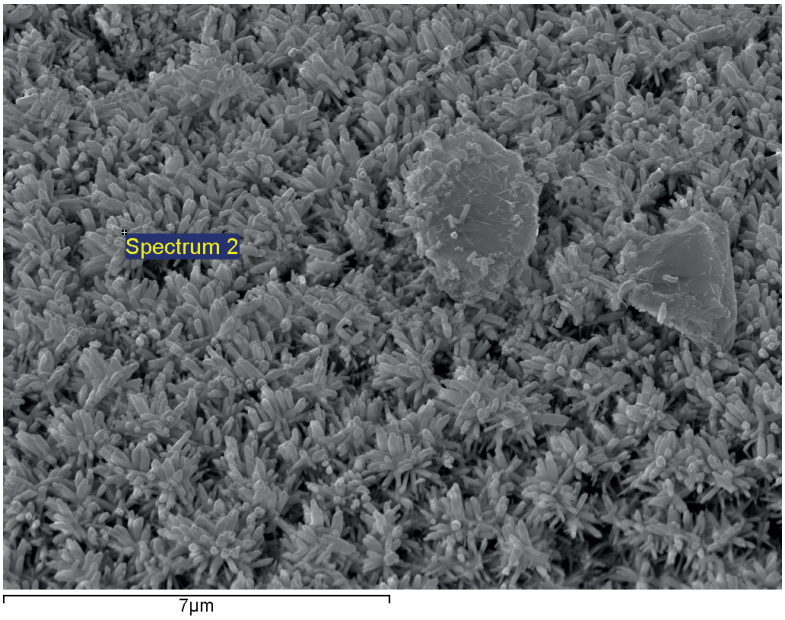

a)

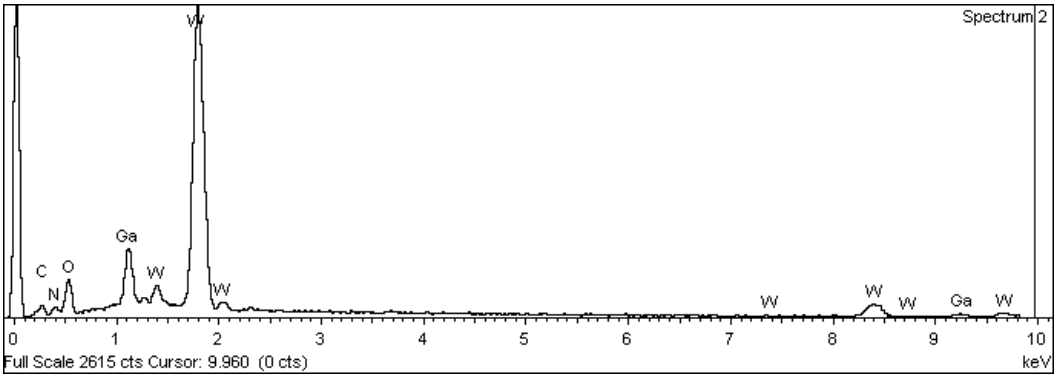

b)

Figure 3.4: Qualitative energy-dispersive X-ray spectroscopy of nanostructures**.** Figure 3.4a shows the location where EDS measurements were performed on the nanostructures from the sample shown in Figures 3.3a and 3.3b. Figure 3.4b depicts the resulting qualitative EDS spectrum. Here, one can see peaks associated with carbon, oxygen, nitrogen, gallium, and tungsten.

Three of the four experimental growths that were performed in the neighbourhood of 700°C resulted in “nanowire-like” structures being grown on the

substrate that differed substantially from ideal semiconductor nanowires in appearance and quality (see Figure 3.3). These nanostructures possessed visually rough surfaces when performing SEM imaging on them and, in general, they showed no collective preferential nucleation direction during growth. However, the sample shown in Figures 3.3a and 3.3b did show large regions where nanostructures grew in a symmetrical, branching manner. Within a given sample, there were a number of different types of similar nanostructures in terms of size. The diameter of these "nanowire-like" structures ranged from tens of nm to 100 nm to over 500 nm. Although the resulting geometry of these structures tended to obscure their true lengths, the lengths of the different nanostructures were estimated to range between 100s of nm to microns. The density of these nanostructures was also quite high given their size distribution and orientation. Qualitative SEM EDS measurements of these samples were dominated by peaks associated with tungsten. Figure 3.4 shows EDS measurements of the nanostructures found on the sample shown in Figures 3.3a and 3.3b. Finally, no metal catalysts were observed at any of the tips of the resulting nanostructures on any of the samples during SEM imaging.

The fourth experimental growth exhibited aberrant temperature readings during the 15-minute deposition run. When the stainless steel sputtering shield was rotated to expose the substrate to the argon/gallium flux, the temperature reading rapidly increased from 707°C to 850°C and may have continued to rise. In order to prevent possible damage to the deposition system, the input power was reduced from 100% (about 221 W) to 70% (160 W). This corrective action resulted in the temperature

reading stabilizing at 700°C for the remainder of the growth. Once again, the growth conditions gave rise to nanostructures. However, this time the resulting nanowires more closely resembled traditional semiconductor nanowires. Figure 3.5 shows distinct nanowire populations formed at the edge and at the centre of the sample. At the substrate edge, the surfaces of the nanowires appeared significantly smoother under SEM imaging than those found at the centre within the same sample and those from previous samples. These nanowires were very straight in appearance and also grew in random directions. In juxtaposition to these nanowires species, those found towards the centre of the sample resembled nanowires found in previous growths, possessing rough surface morphologies and not perfectly straight structures. The nature of the nanowires found at the edge of this sample prompted the use of TEM to examine individual wires more closely. Figure 3.6 depicts the TEM analysis of an isolated nanowire. Both bright-field and HAADF STEM images seem to indicate that the nanowire possesses a core-shell structure. This idea is corroborated by the axial EDS linescan shown in Figure 3.6d, where the tungsten signal diminishes as the linescan moves from the region of the nanowire possessing a shell to the tip of the nanowire where it does not. Both the axial and transverse EDS linescans evince that the tungsten levels within the nanowire far exceed those of gallium and oxygen. It is also pertinent to note that no gold catalyst particles were found on the tips of nanowires during SEM and TEM analysis of nanowires from this sample.

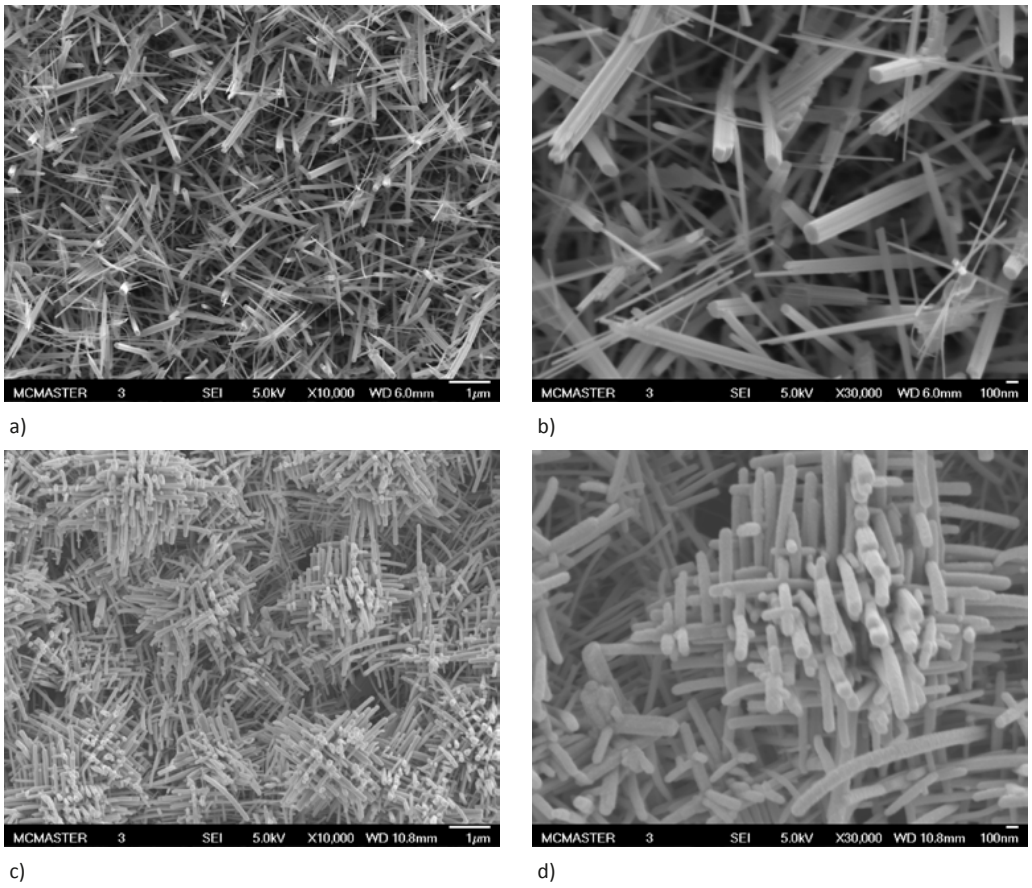

Figure 3.5: SEM images from anomalous nanowire growth experiment (0° tilt angle). Figure 3.5a and Figure 3.5b display the resulting nanowire structures near the edge of the sample at 10000X and 30000X magnification, respectively. Figure 3.5c and Figure 3.5d display the resulting nanowire structures near the centre of the sample at 10000X and 30000X magnification, respectively.

Although these initial experiments were successful in producing “nanowire-like” structures, the results seem to indicate that these structures were neither high quality nor primarily gallium nitride in terms of composition. These experiments also raise concerns about substrate temperature and contamination during nanowire growth. Even when the input power to the substrate heater is set to 100%, the substrate temperature is regularly measured to be around 700°C, a level far below the high

temperatures typically used within the literature to grow gallium nitride thin films and nanowires. Such insufficient temperatures are a plausible explanation for the surface roughness witnessed on the resulting nanowires since adatoms would be more likely to impinge at a given site on the surface and incorporate immediately there rather than diffuse and aggregate into larger smoother polycrystalline step edges.

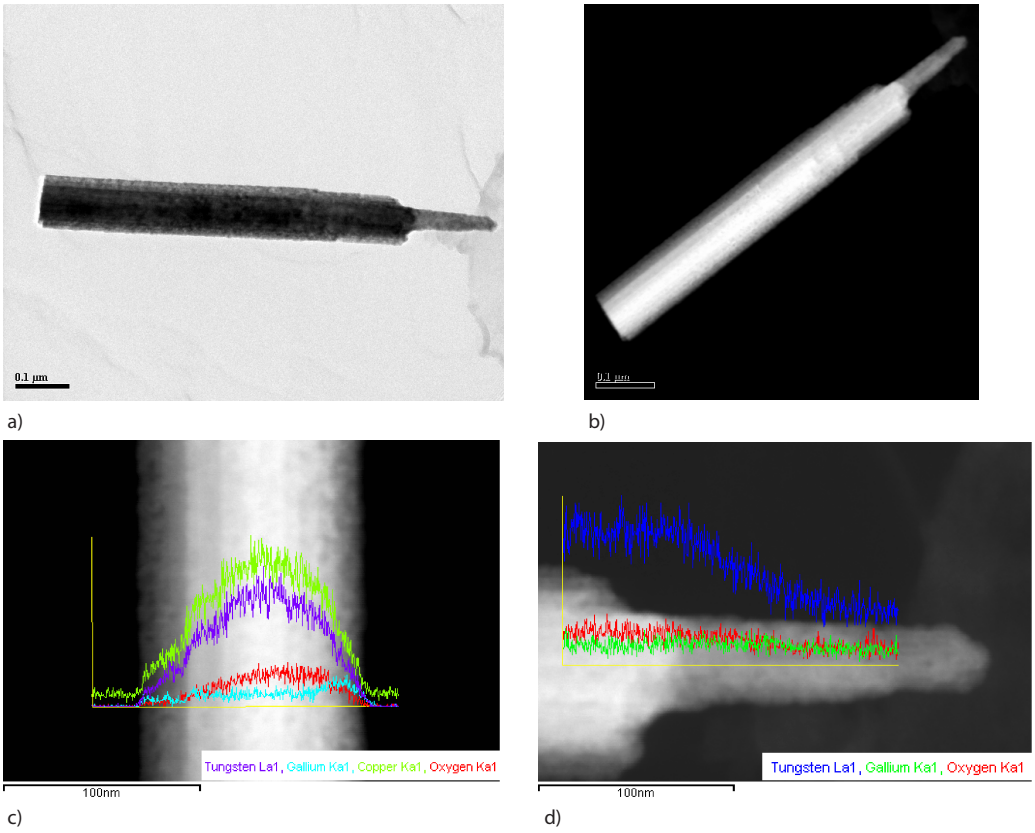

Figure 3.6: TEM images from anomalous nanowire growth experiment. Figure 3.6a depicts a bright-field TEM image of an isolated nanowire. Figure 3.6b shows a high-angle annular dark-field image of the same nanowire. Figures 3.6c and 3.6d exhibit the results of a transversal and axial TEM EDS linescan, respectively.

Whether or not the thermocouple reading accurately reflects the substrate temperature is another important issue. In the current design, it was quite difficult to

ensure that the thermocouple tip was always on the backside of the substrate during a growth. Sometimes it could be, but it is possible that the tip was farther away than thought or perhaps touching the heating filament. Moreover, there were definitely some temperature concerns within the anomalous nanowire growth experiment. The temperature levels and the temperature spike could not be experimentally repeated. A likely explanation for the temperature spike would be an electrical short between the thermocouple wires or a loose electrical connection. The apparent higher temperatures may have also been the result of the thermocouple being closer to the filament.

Despite the temperature questions raised by this aberrant experiment, this experiment and the others were useful in identifying the likely presence of the thermal gradient across the substrate during a growth. The quality of the nanostructures tended to be better as one approached the edge from the centre, and the edges were closer to the cylindrical heating filament than the centre. This proximity to the heater element would spatially correlate with greater heat transfer over the course of the growth. Figure 3.7 shows a transition region between the centre and the edge of the sample shown in Figures 3.3e and 3.3f, where the resulting nanostructures appear more ideal as one moves towards the edge of the sample (and towards the heating element).

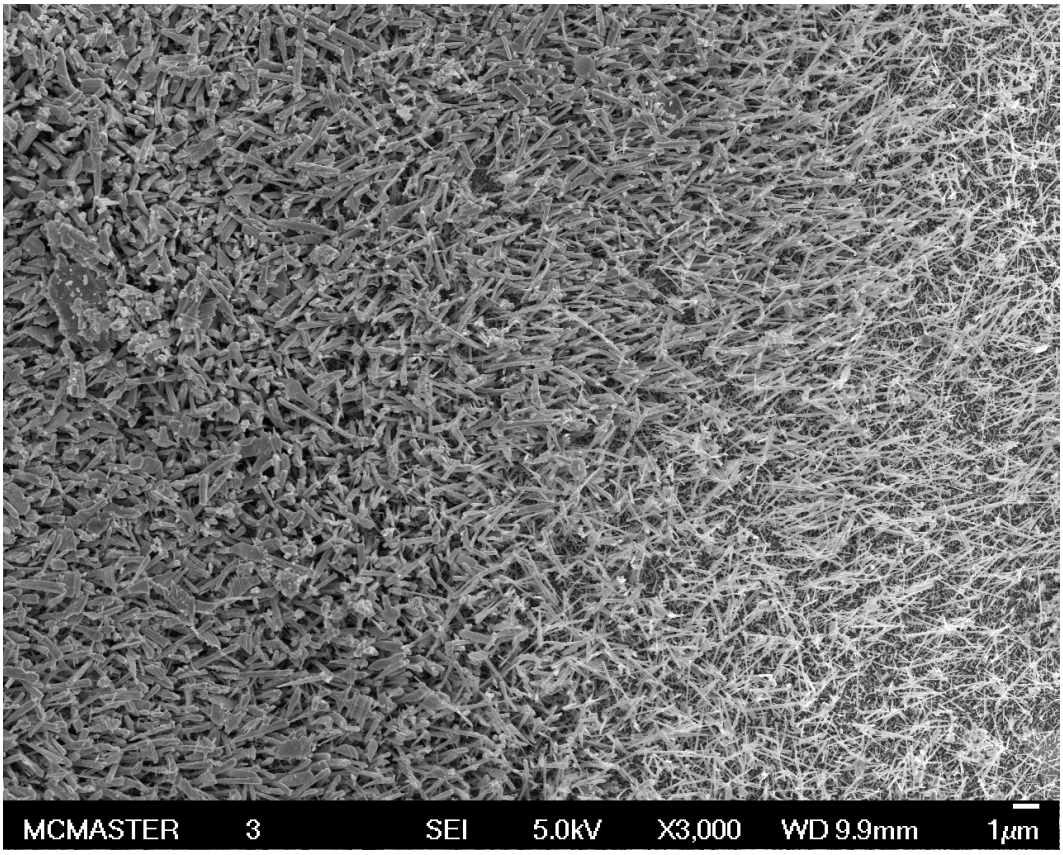

Figure 3.7: SEM image showing possible temperature gradient across substrate**.** This image of nanostructures was taken from the substrate shown in Figures 3.3e and 3.3f. The progression from left-to-right in this image corresponds to radial movement from the centre of the sample towards its edge.

The second major finding during these experiments was the large tungsten presence within the resulting nanostructures. The significant contamination of the nanowires from elements present within the chamber, made it difficult to isolate whether or not gold served as the primary VLS catalyst, if at all. The likely source of tungsten debasement was the heating filament behaving as an evaporative source. There was no barrier between the filament and the substrate to prevent any sublimated

tungsten vapor from being transported to the surface of the substrate and incorporated into the growing nanostructures. Even if tungsten was not present, the lack of a negative control region on a sample (i.e. a region without gold) made identifying the origin of nanowire growth difficult. Any resulting nanowire growths could not be compared to a possible control thin film (or hypothetical self-catalyzed nanowires). All of these findings helped to shape future experiments and served as the motivation for developing a new furnace design.

3.3 Furnace Design

3.3.1 Motivations and Design Goals

Temperature limitations and unwanted sample contamination became the major motivations for developing a new substrate heater, but they were not the sole reasons for doing so. There were reliability problems associated with the tungsten filament being heated while supporting the alumina crucible. Upon replacing a filament, there was only a limited time (and number of heating cycles) until the weight of the crucible caused neighbouring windings of the filament to touch and short-circuit. This was particularly problematic when such an event occurred part way through an actual deposition run. Depending on the positions of the filament coils when loading, it was also difficult to load the sample holder into the crucible without displacing the actual sample. Another weak point of the original design was the use of an alumina screw to electrically isolate the molybdenum shield from the stainless steel mounts. This ceramic screw could be easily broken and had been previously. Finally, the introduction of a

larger sample size would allow multiple experiments to be performed in parallel more easily.

The major design criteria for the new furnace designs were extending the temperature range to at least 800°C, minimizing external contamination (preferably to negligible levels), increasing the reliability of the heating filament, and improving experimental throughput. Higher temperatures were to be achieved by generating more heat and minimizing its loss. A direct line-of-sight between the tungsten filament (that had been present before) would be eliminated through the use of a ceramic shell and ceramic beads. Reliability was to be increased by ensuring that no weight was supported by the tungsten filament. Lastly, increasing the sample size to 16 mm x 16 mm squares and introducing catalyst patterns as described in section 2.3.2 allowed four experiments to be performed in the place of just one. Other minor design objectives were modularity and ease-of-loading.

3.3.2 Materials Selection and Manufacturing

The materials selection process for this project was primarily driven by the suitability of a material for an evacuated environment (i.e. minimal outgassing) and high-temperature work. Strength and weight were also considerations. Type 304 stainless steel was chosen to be used for support structures due to its preferential use in vacuum systems because of its low volatility, toughness, and corrosion resistance. The refractory metal molybdenum was selected to be used for metallic heat shielding. Alumina (i.e. aluminum oxide, Al_2O_3), a ceramic material, was selected to be implemented where electrical or thermal isolation was desired. Oxygen-free high-

conductivity (OFHC) copper was chosen for selected parts used in the conduction of electricity between the input transformer and the heating element. All manufacturing of customized furnace parts other than those made from ceramics was performed using equipment within the Engineering & Science Machine Shop at McMaster University, such as lathes and milling machines. Once machining was completed, all parts were put through consecutive five-minute sonicated baths in acetone, ethanol, and deionized water then dried before being assembled.

The manufacturing process had its moments of learning. Two are worth discussing. The first one involves learning how to machine stainless steel properly. Stainless steel is a much more difficult material to machine correctly than aluminum, another metal typically used in the construction of scientific equipment. There were numerous setbacks when tapping a 6-32 thread and drilling holes with diameters smaller than 1/8”, including broken drill bits and taps. These consequences would often require the work pieces to be re-machined, often only to have one or both of these problems happen again. Eventually, some research indicated that these problems could be traced to the stainless steel undergoing work hardening as a result of inferior quality cutting tools. Sourcing and purchasing high-speed steel drill bits and taps, and using them in conjunction with large amounts of cutting fluid overcame this problem.

The other pertinent learning point related to developing a procedure to drill closely spaced holes through alumina ceramic. Alumina offered many advantages as an insulator material under vacuum, but its high brittleness and low thermal conductivity posed problems when drilling or cutting it. Drilling too fast or with too much pressure

would cause the material to either fracture immediately or introduce mechanical stresses that would be aggravated during subsequent processing and/or heating.

Three obstacles were overcome: ensuring a slow drilling speed, securing the sample, and finding an appropriate cutting tool. A stock drill press present within the Kitai lab did not initially allow for sufficiently slow drilling speeds. This shortcoming was addressed by re-machining two salvaged pulleys to fit the drive and drill shafts of the aforementioned drill press, implementing these pulleys with the much smaller one on the drive shaft, and replacing the drive belt with one sized to fit this customized setup. Next, securing the ceramic properly during machining was handled. Through trial-and-error, it was found that mounting the alumina samples (e.g. 1 mm thick plates or crucibles) to a 1/4" plate of aluminum using Crystalbond™ adhesive was the most effective method to reliably and temporarily bond the ceramic. Finally, determining an appropriate cutting tool for an ultra hard material like alumina was investigated. Through extensive research, it was determined that diamond drill bits would be able to drill through alumina, provided that one used large amounts of water as coolant. Diamond hole saw drill bits from two American companies, UKAM Industrial Superhard Tools and Diamond Drill Bit & Tools, were then ordered and evaluated using different drilling setups and applied pressures. The performance of the UKAM drill bits was quite unsatisfactory – they were not able to penetrate the 1 mm thick alumina plate. In contrast to this, the drill bits from Diamond Drill & Tools were able to machine through the plates and crucible.

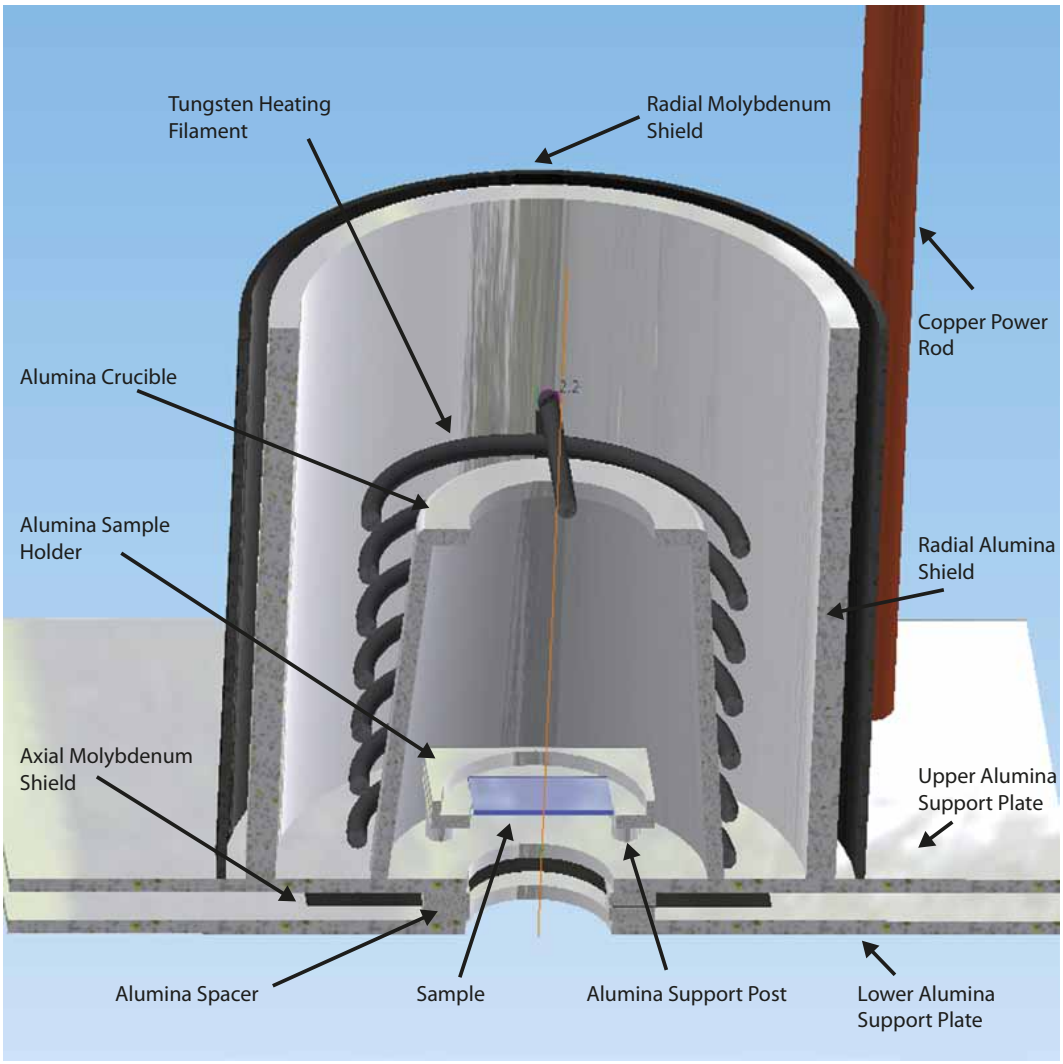

Figure 3.8: Simplified Cross-section of "Mark 1" Furnace Design. Image is rendered using AutoCAD Inventor Software.

3.3.3 "Mark 1" Design

The development of the "Mark 1" design sought to address the problems outlined in section 3.3.1. This design began with an alumina crucible that contained the sample and its holder during a given growth experiment. A cylindrical tungsten heating filament wrapped around the exterior of the alumina crucible and was connected to the

main copper power lines by screw-tightened copper connectors and braided copper wire. These materials were supported by two alumina plates, in between which a piece of molybdenum was placed. Finally, an array of cylindrical heat shields was placed concentrically about the alumina crucible. This arrangement is illustrated in Figure 3.8 as a simplified cross-sectional view of this furnace design and its important components. The final “Mark 1” furnace assembly is shown in Figure 3.9. Here, the copper electrical connectors, braided copper wires, alumina beads, and the weight-bearing structure are visible. It is important to note that the plastic sheath covering the braided copper wire was removed prior to installation.

The size of the sputtering chamber and the geometry of the magnetron cathode introduced dimensional constraints during the design process. These size limitations and the original furnace design influenced the final structure of the “Mark 1”. Like the original substrate heater, this design relied on the central stainless steel nitrogen line to bear the weight of the entire furnace apparatus through horizontal stainless steel rods and copper power lines. That being said, the “Mark 1” employed two solid 0.25-inch diameter OFHC copper rods (McMaster-Carr) instead of the 0.1875-inch diameter ones used previously, and an additional set of horizontal supports as means to support more weight. The upper and lower alumina support plates bore the weight of the central furnace; stainless steel clamps buttressed these plates below. Moreover, The arrangement of these 1.5 mm thick alumina plates negated the need for any alumina screws to be used for electrical isolation. A 0.875-inch aperture was drilled into the top of a C6-AO alumina crucible (RD Mathis) to facilitate easy positioning of the

thermocouple probe behind a sample during a growth. The larger size of this crucible compared to that of the one used in the original furnace also allowed for bigger substrates.

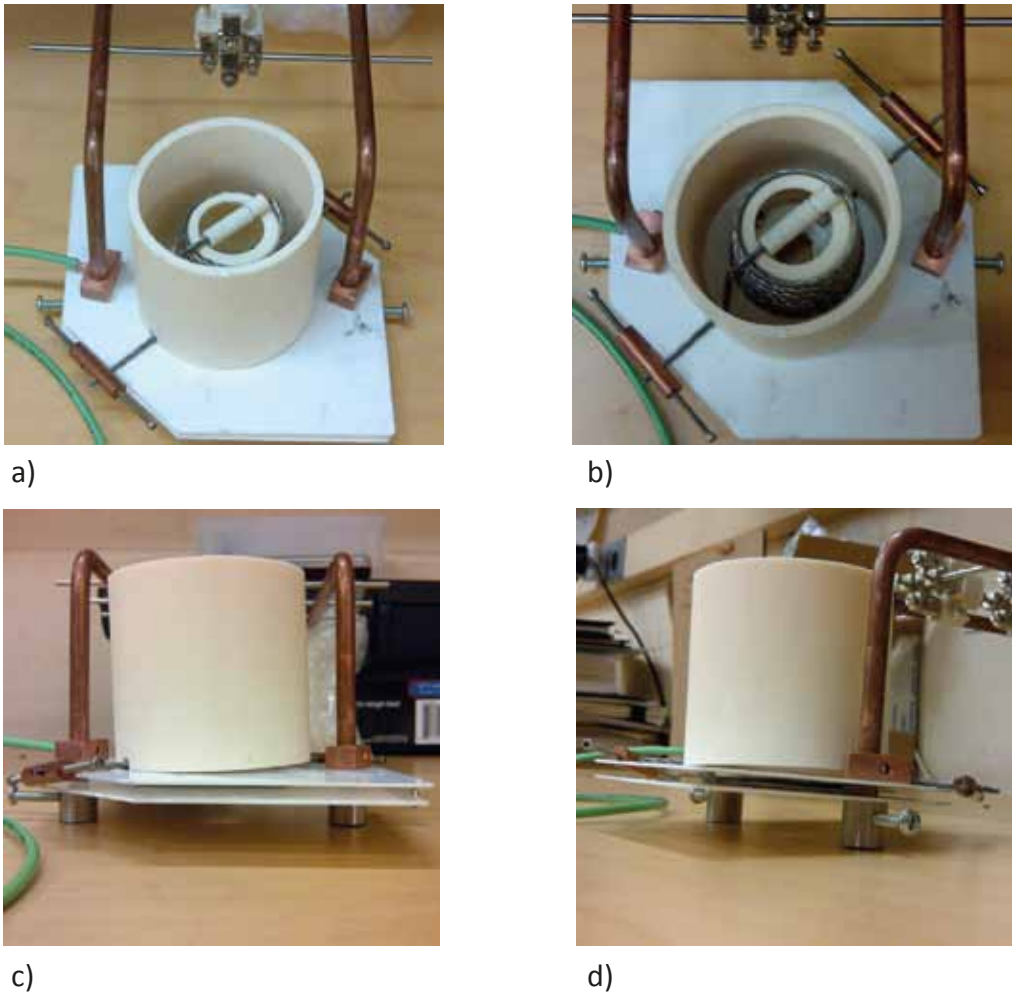

Figure 3.9: Images of completed “Mark 1” Design Prior to Installation. a) Iso-Top View. B) Top View. C) Front View. D) Iso-Side View.

Eliminating the high levels of tungsten found in early nanowire experiments also factored into the “Mark 1” design. It was hypothesized at the time that the tungsten filament was acting as an evaporative source. The apparently logical solution to this

problem was to prevent a direct line-of-sight between the filament and the substrate during a growth. This was accomplished by positioning the sample and its holder within an inverted barrier (i.e. the modified alumina crucible.). The geometry of the tungsten filament (RD Mathis) ensured that part of the coil would cross the previously mentioned 0.875-inch aperture; this feature was covered with alumina beads in order to minimize the probability of the tungsten atoms entering into the crucible. Incidentally, the inverted nature of the crucible and tungsten filament also alleviated the need of the filament to bear any weight.

Most importantly, the "Mark 1" design was created to dramatically increase temperature output. The "Mark 1" was built on the premises that increasing the amount of input power and decreasing the amount of heat lost during operation would both improve temperature performance. Thicker copper power lines enabled the transmission of higher currents to the tungsten filament without sacrificing mechanical integrity. The tungsten coil chosen for Joule heating was also larger in size and in number of coils than the one previously used, in order to maximize its electrical resistance. Methods to minimize conductive, convective, and radiative heat loss were also examined. Ultimately, reducing radiative loss was selected to be the primary concern. Using the cylindrical symmetry about the sample as a guide, heat can escape as radiation axially (i.e. vertically) and radially outwards. Cylindrical heat shields composed of 99.8% pure alumina (Anderman Ceramics Limited) and molybdenum (Alfa Aesar) were positioned concentrically about the sample as attempts to trap and reflect heat back towards the substrate. An axial heat shield made of molybdenum (Alfa Aesar)

was positioned below the sample in order to both reflect heat back up to the substrate and reduce the amount of blackbody radiation that damaged the gallium target below. It was decided that it was not practical to place any axial heat shielding above the heater due to sizing and complexity constraints.

All engineering diagrams pertaining to the “Mark 1” design can be found in the appendix.

3.3.4 “Mark 2” Design

Temperature testing of the “Mark 1” model identified a major engineering flaw: the design was not able to bear the weight of the furnace during heating. The “Mark 2” design involved devising another way to bear the weight of the furnace and organize the axial heat shielding. This variant would also adopt a number of the features from the “Mark 1” design without any modification, including structural supports (i.e. 0.25-inch copper power lines, stainless steel support rods, etc…), heating configuration (i.e. tungsten filament, electrical connections, and alumina crucible), and radial heat shields.

Alumina was originally chosen to be the material of the support plates in the “Mark 1” design because it is a strong, light material that is also a great insulator while under vacuum. It appeared that the 1.5 mm thick alumina plates might not have been thick enough.That being said, installing an arbitrarily thick alumina plate was not a realistic option since the overall weight of the furnace needed to be minimized in its current configuration. A number of possible solutions were evaluated to replace these plates, and in the end, it was decided that modifying a 99.8% pure alumina boat

(Anderman Ceramics Limited) was the best course of action. This ceramic boat provided a lighter structure than a standard piece of alumina of comparable size since it was hollowed out and its 2mm thin wall provided a 33% increase in thickness. The geometry of the ledge differed from the previous design in that it was not a square plate. This is important because the square plate design of the "Mark 1" made it susceptible to differential thermal expansion; areas close to the centre (and close to the heating filament) experienced a much larger expansion than outer regions (away from the heat source), eventually resulting in thermal shock and cracking of the plate.

In addition to the central 0.625-inch aperture that allowed the argon/gallium flux through, two oversized 0.25-inch holes were drilled to allow for deformation of the copper power lines and alumina boat during heating. The height of the boat was also reduced to 15 mm in order to prevent it from interfering with the rotation of the sputtering shield. This modified boat was installed in an inverted fashion so as to create a support ledge between copper power lines. The radial heat shields were placed symmetrically on this alumina ledge about the central 0.625-inch aperture.

The other major design change in the "Mark 2" involved reconfiguring the central superstructure that supported the sample holder and alumina crucible, and contained the axial heat shielding. Previously, the alumina crucible and sample holder were both located above the upper alumina support plate and the axial heat shielding was sandwiched between the upper and lower alumina support plates. This new design involved reducing the size of the top and bottom alumina plates from 102 mm (4-inch) x 102 mm (4-inch) x 1.5 mm to 50 mm x 50 mm x 1.5 mm. Each of these new alumina

plates would maintain the same geometry of holes from the “Mark 1” design, but the 0.25-inch holes that had surrounded the copper power lines were eliminated. The 0.625-inch hole would continue to act as an aperture for the incoming argon/gallium flux, while the four 0.125-inch holes would function to position the alumina rods that supported the sample holder and prevented the assembly from shearing apart. From top-to-bottom, the new superstructure contained a top alumina plate with four 0.125-inch holes and one central 0.625-inch hole, a molybdenum heat shield with four 0.125-inch holes and one central 0.625-inch hole, two alumina spacers (each with two 0.125-inch holes), a molybdenum heat shield with four 0.125-inch holes and one central 0.625-inch hole, and a bottom alumina plate with only a central 0.625-inch central hole. This central superstructure with the four-alumina posts aligned through the four 0.125-inch holes was aligned with the 0.625-inch hole on the alumina support ledge. The sample holder and alumina crucible were then placed on top this structure.

Figure 3.10 shows AUTOCAD Inventor® rendering of the “Mark 2” furnace design. All engineering drawings relating to the “Mark 2” design can be found in the appendix.

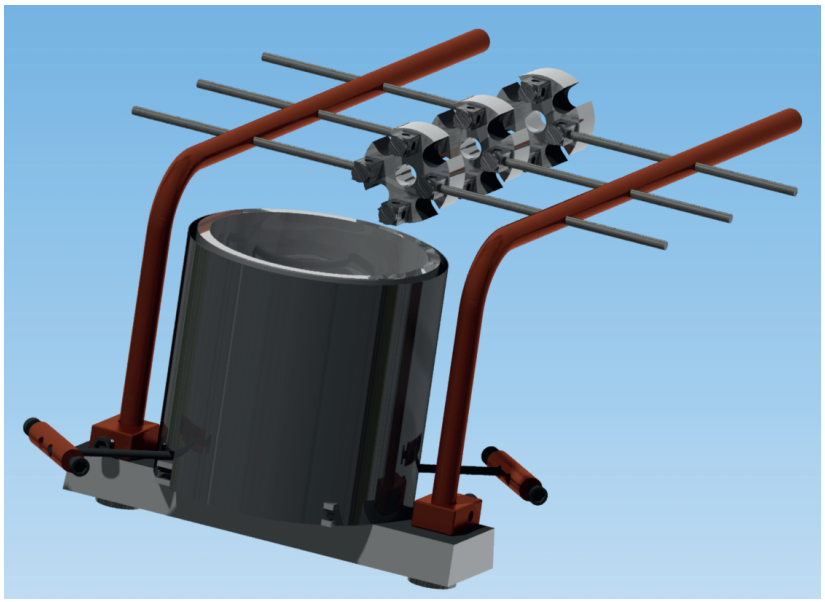

a)

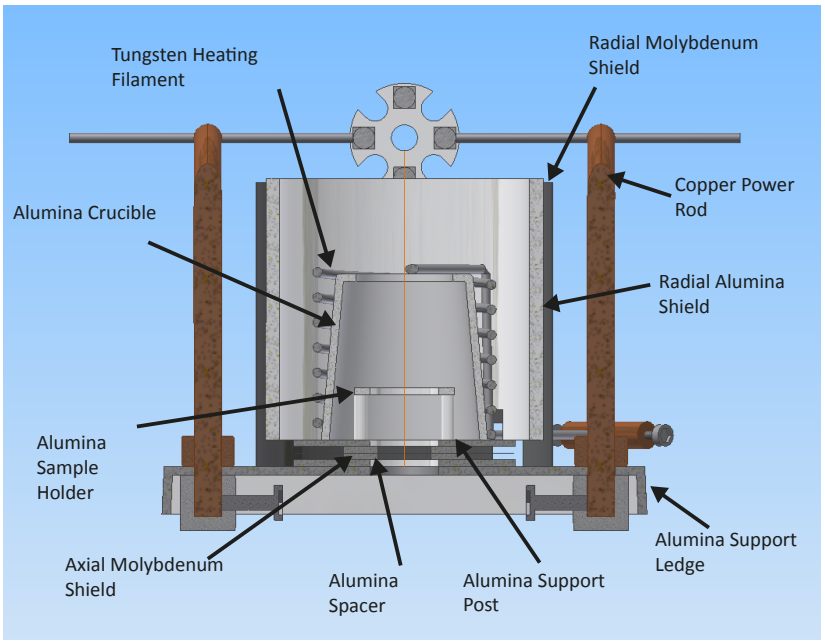

b)

Figure 3.10: "Mark 2" Furnace Design. Figure 3.10a shows an AUTOCAD Inventor rendering of the "Mark 2" design. Figure 3.10b depicts a simplified cross-section of the design.

3.3.5 "Mark 3" Design

Shortcomings of the "Mark 2" design became apparent over time and with experience using the setup. In particular, there was a need to address the integrity of the electrical connections and the ability to quickly and reliably load a sample in the next design iteration. The "Mark 3" design incorporated a large number of features from its predecessors, including the crucible, the weight-bearing alumina ledge, and the sample holder. Figure 3.11 shows an installed "Mark 3" furnace design without any radial shielding.

The screw-mounted copper electrical connector between the main 0.25-inch diameter power lines and the braided copper wires was sometimes observed to be loose following a growth experiment. The original electrical connector used a 2-56 UNC screw to ensure contact between the rods and braided wires. A possible explanation for this phenomenon may be that the small size of this screw in conjunction with electrical heating degraded the amount of pressure provided by the screw with usage over time. In order to ensure maximum power transfer to the furnace, a larger connector capable of maintaining a stronger pressure while securing the electrical leads was created. A 0.4-inch x 0.4-inch x 0.7-inch OFHC copper rectangular prism was machined to allow for the use of a 6-32 UNC screw. This larger screw would be able to generate more pressure. These connectors can be seen at the base of the input and output copper rods in Figure 3.11.

The other major change to the furnace design involved a reworking of the structure that supports the central superstructure (i.e. sample holder, axial shielding,

and alumina crucible) on top of the weight-bearing alumina ledge. In the previous model, there were two molybdenum axial shields, two different pieces of 1.5-mm alumina plates, and a set of alumina guides that functioned to stabilize the 0.125-inch diameter alumina rods that supported the sample holder. This arrangement was not the easiest to load a sample onto. While experience with the dexterous task of loading the sample into the furnace improved one's ability to correctly assemble the heater, it was by no means a trivial process. Many things could happen. For example, the alumina support rods could move and dislodge the sample away from the centre or the sample holder could dislodge and prevent the sample from being exposed to the gallium/argon flux. The "Mark 3" design simplified this and only used two pieces of alumina and one molybdenum shield. The introduction of a 2-inch x 2-inch x 0.25-inch 99.8% pure alumina plate (Anderman Ceramics Limited) with 0.125-inch diameter holes helped to stabilize the alumina posts by providing more vertical support. The bottom alumina plate and the molybdenum heat shield for axial heat reflection were recycled from the "Mark 2" design. The new ceramic plate elevated the alumina crucible higher than before and necessitated trimming the 70 mm tall molybdenum radial heat shield to a height of 50 mm. This entire central superstructure is located beneath the alumina crucible in Figure 3.11.

All engineering drawings relating to the "Mark 3" design can be found in the appendix.

Figure 3.11: "Mark 3" furnace design without any radial shielding.

3.3.6 Miscellaneous Sputtering System Modifications

At the same time that the “Mark 3” furnace design was created and installed, a critical modification to the sputtering system was made. It had been previously found that the original oxygen-free high-conductivity copper target holder was interacting with the gallium metal that it contained. A customized 2-inch diameter, 0.25-inch thick graphite target holder with an impurity level of 5 parts per million was commissioned

from Graphite Machining Inc. A more detailed discussion about this interaction problem can be found in section 3.4.2. The engineering drawing of this holder is available in the appendix.

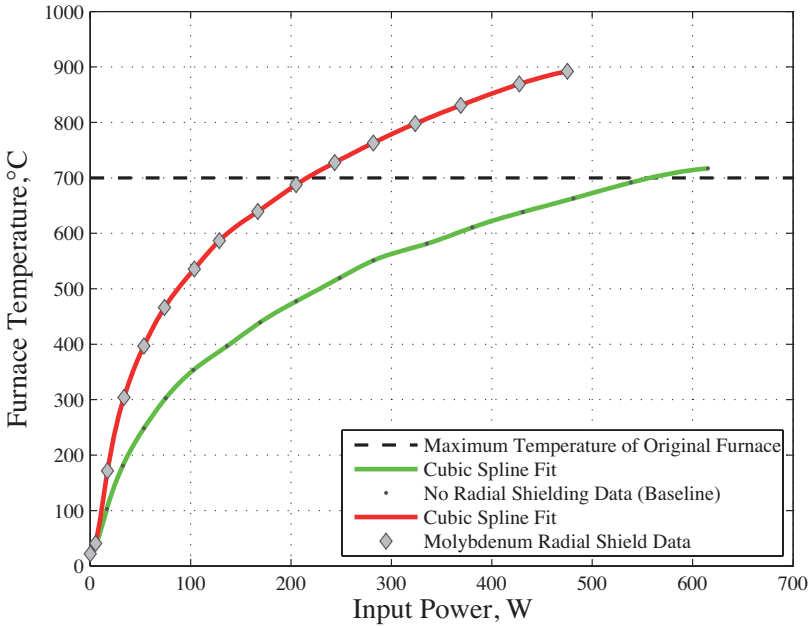

a)

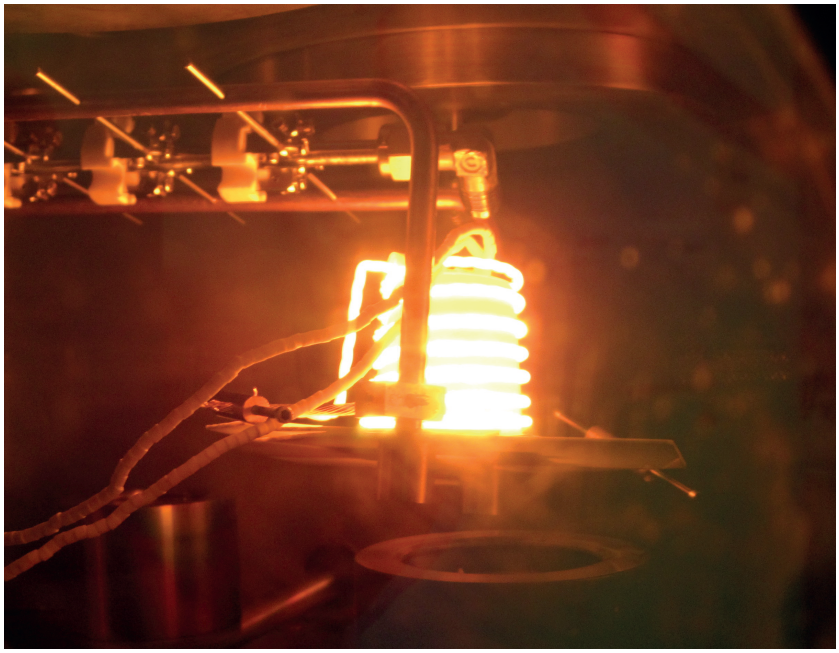

b)

Figure 3.12: Thermal output of "Mark 1" furnace design. Figure 3.12a depicts the relationship between input power and output temperature for the "Mark 1" design for non-shielded and molybdenum shielded configurations. Figure 3.12b illustrates the non-shielded configuration being heated.

3.4 Furnace Baseline Experiments

3.4.1 Temperature Performance

All furnace designs were benchmarked according to temperature output prior to being used for the actual nanowire growth experiments. This benchmarking process was performed in a similar manner to the heating procedure described in section 2.4.2, however it differed in that ramping of the variable autotransformer proceeded at intervals of 5% rather than 10%. Temperature, voltage, and current readings were taken after the furnace was allowed to sit for 10 minutes at each setting. The temperature outputs were then compared with the maximum temperature regularly realized by the original furnace (i.e. 700°C) and the design goal of generating temperatures in excess of 800°C.

The thermal performance data collected from the benchmarking of the "Mark 1" design is depicted in Figure 3.12. Here, two variants of this design are compared: one without a radial shield and one with a molybdenum radial shield. In the case of no shielding, the design exceeded temperatures of 700°C at only 85% of input power. This power setting resulted in a temperature of 717°C while dissipating about 615 W. Measurements at higher input power were not pursued since the model demonstrated that it could exceed the performance of the original substrate heater without the use of any radial shielding. The second configuration that involved a molybdenum shield performed even better than its non-shielded counterpart, and this is quite evident from 15% input power onwards. This configuration exceeded the design objective of 800°C at

60% input power (i.e. 324 W) and ultimately was able to reach a stable temperature of 892°C at 75% input power (i.e. 475 W).

When the input power was further increased and a temperature of 906°C was achieved, the bottom alumina plate cracked completely and the top one partially fractured. At this point in time, the benchmarking experiment was terminated. The mechanical failure of the design can most likely be attributed to the weight distribution of the superstructure and the spatial variation in temperature across the alumina plate. Most of the weight of the superstructure is concentrated at the centre of a 1.5 mm thick ceramic plate. The introduction of the radial molybdenum shield significantly improved temperature output by reducing radiative heat loss from the tungsten filament. This reduction in heat loss via radiation was qualitatively corroborated through the operator's perception of a discernibly elevated temperature outside the deposition chamber when not using the molybdenum heat shield. The higher concentration of heat at the centre of the furnace may have led to larger thermal stresses being created at the centre rather than further outwards. While one cannot definitively rule out the introduction of mechanical stresses during manufacturing as a cause, the localization of weight distribution and thermal stresses at the centre seem to be the likely explanation for this design failure. Incidentally, this mechanical failure of the "Mark 1" design precluded a planned experiment to explore the effects of a radial alumina shield.

The output temperatures of the "Mark 2" design for different input powers and radial shielding arrangements are shown in Figure 3.13. Temperature measurements were taken at intervals of input power up to and including 80%. The baseline version of

this design without radial shielding achieved a final stable temperature of 713°C with an input power of 525 W, again exceeding the performance of the original furnace. The usage of alumina and molybdenum radial shielding resulted in maximum steady temperatures of 848°C (at 526 W) and 922°C (at 524 W), respectively. Both of these radial shield types were capable of meeting the outlined temperature design criteria and outperformed the non-shielded version. Ultimately, the molybdenum shield configuration was used during initial nanowire growth attempts that used gold catalysts because it showed the best performance and was an easier option to set up.

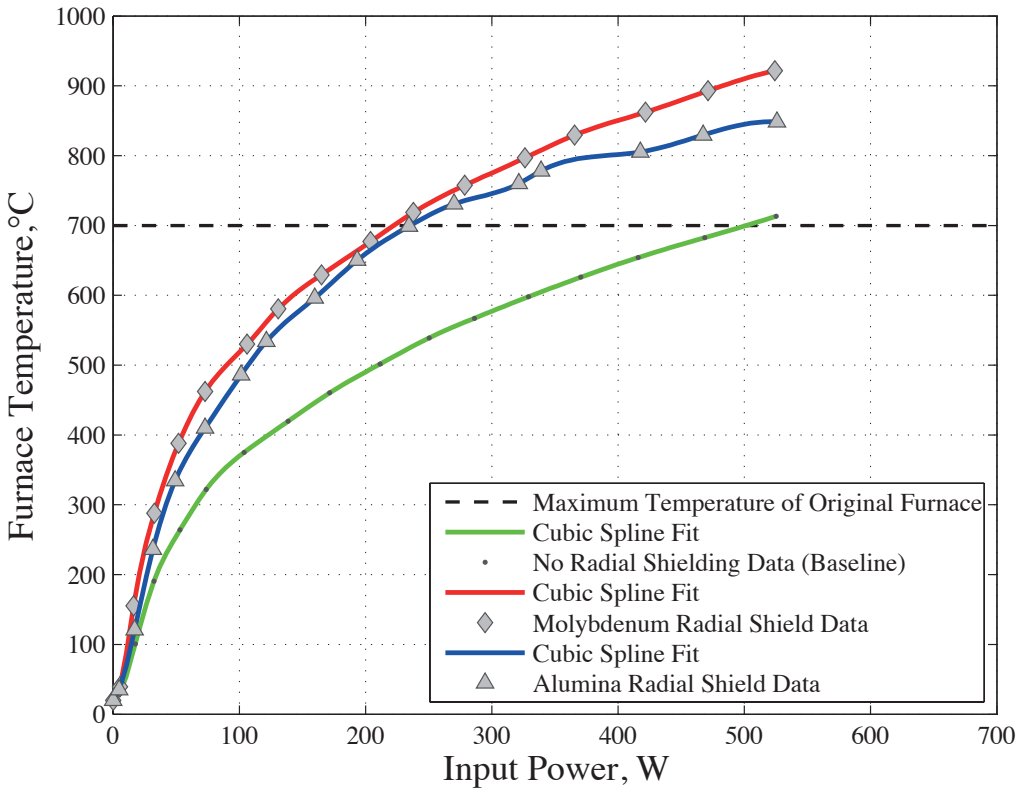

Figure 3.13: Thermal output of "Mark 2" furnace design**.** Figure 3.13 shows the relationship between input power and output temperature for the "Mark 2" design for non-shielded and shielded configurations (i.e. alumina and molybdenum).

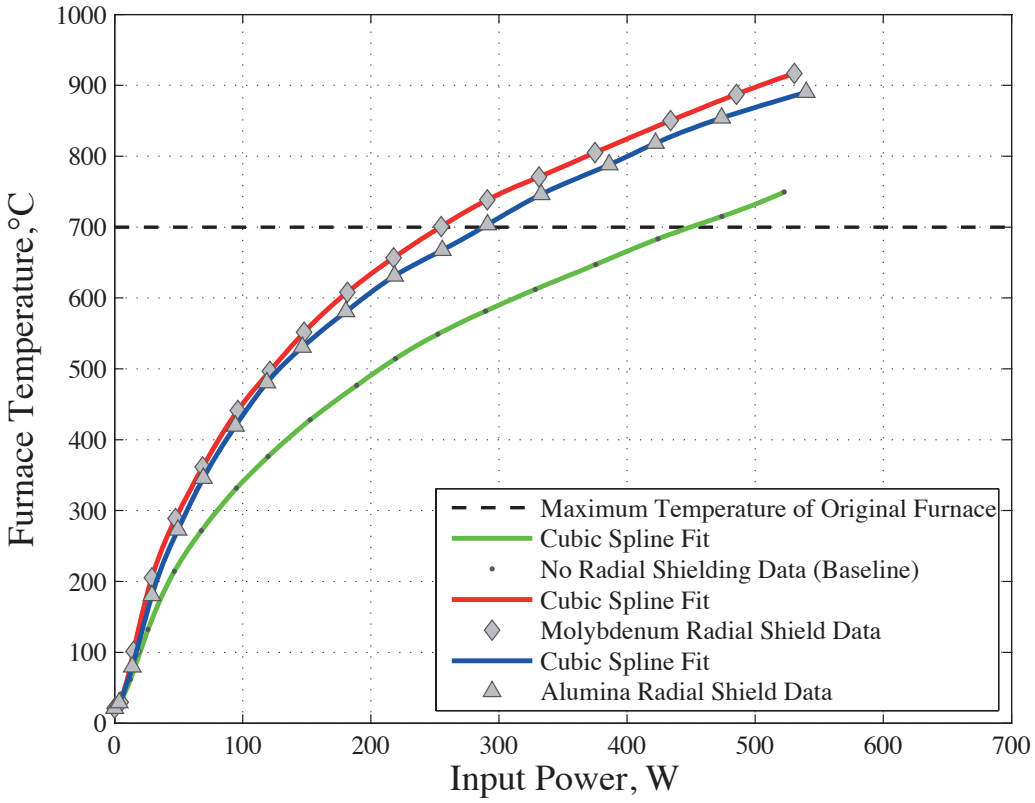

Figure 3.14: Thermal output of "Mark 3" furnace design**.** Figure 3.14 exhibits the relationship between input power and output temperature for the "Mark 3" design for non-shielded and shielded configurations (i.e. alumina and molybdenum).

As mentioned in sections 3.3.5 and 3.3.6, a third variant, the "Mark 3" design, was designed and built. Figure 3.14 displays the outcomes to the same baseline testing scenarios subjected to the previous design iterations. Here, the input power measurements were carried up to 85% of the total input power available. Like the "Mark 2", an unshielded "Mark 3" design was able to exceed the temperature limits of the original substrate heater when 80% input power was applied (715°C at 474 W). The maximum output temperatures at 85% input power of the unshielded, alumina radial shielded, and molybdenum radial shielded variants were 749°C (523 W), 890°C (540 W), and 917°C (530 W), respectively. Once again, the temperature design requirements

were met. When this model was used to grow nanowires, the molybdenum radial shielding was implemented because it performed better and was easier-to-use.

The above figures and discussion demonstrate the efficacy of the modified furnace design at obtaining and maintaining growth temperatures that both exceed the performance of the prior substrate heater and lie in the temperature regime associated with gallium nitride growth. Figure 3.15 summarizes the temperature performance of the different shielding choices across models. All variants meet the minimum temperature threshold and show a positive correlation between input power and output temperature. It is worth noting that molybdenum radial shielding appeared to be more effective in minimizing heat loss in the “Mark 1” and “Mark 2” furnace designs. This result can probably be traced to the change in height of the molybdenum shield between the “Mark 2” and “Mark 3” designs. The height of the shielding was trimmed from 70 mm to 50 mm to facilitate heater assembly prior to each growth. This reduction in height would correspond to a loss of surface area able to reflect outgoing radiation generated by the tungsten filament. It is also worth mentioning that neither of the “Mark 2” nor the “Mark 3” designs ever failed like their predecessor.

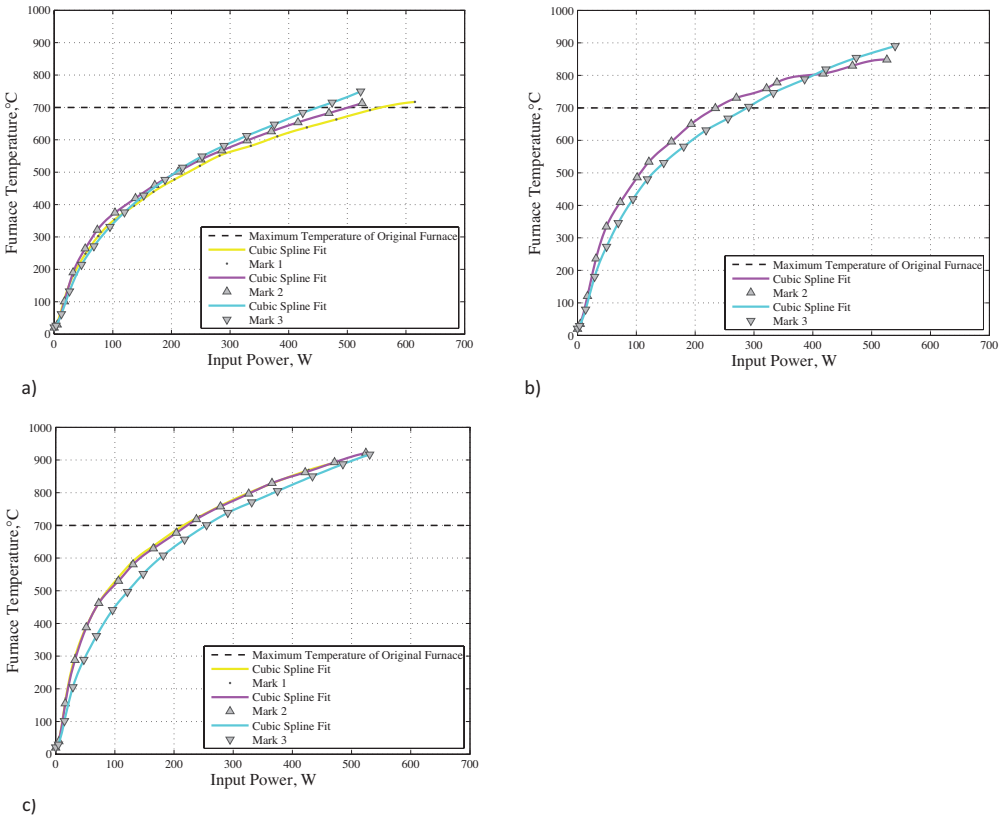

Figure 3.15: Comparison of Shielding Performance Across Different Designs. Figure 3.15a to 3.15c compare the temperature outputs across different furnace designs for a given shield arrangement.

3.4.2 Contaminants Performance

This section examines the proficiency of the new furnace designs to eliminate extraneous contaminants.

As mentioned previously, the mechanical failure of the “Mark 1” design resulted in the fracture of the alumina support plates. Pieces of the top plate were collected and analyzed. Figure 3.16 suggests that outgassing of the tungsten filament occurred during heating. Here, the portion of the top support plate that would have been located

beneath the alumina crucible during operation appears discernibly cleaner (and whiter) than areas outside of the crucible where the tungsten filament would have resided. There is also a gradient of deposited grey material present outside the crucible's edge. A thin layer of gold was deposited onto this piece of alumina to prevent charging and then it was analyzed using SEM. Figure 3.17 summarizes the findings of this analysis. The surface morphology of the area that was housed within the alumina crucible was noticeably smoother in appearance than that of regions within the grey gradation. Point EDS measurements consistently identified the presence of tungsten within the grey region, but not within the inner crucible region. Subsequent EDS measurements of thin films and nanowires grown using the "Mark 2" and "Mark 3" furnace designs also did not identify the premise of tungsten contamination within samples. These facts lend credence to the overall effectiveness of the furnace designs to reduce tungsten contamination to negligible levels.

Over the course of early growth experiments using the "Mark 2" furnace design, it became apparent that there was also copper contamination present in samples following a deposition. Through the process of elimination, the source of the copper was discovered to be the copper target holder that housed the gallium target. This problem was overcome by substituting a customized graphite holder as discussed in section 3.3.6. Once this new holder was introduced, the copper peaks disappeared from SEM EDS measurements. Incidentally, quantifying copper contamination levels using TEM EDS linescans was not pursued because the grids on the TEM samples were composed of copper themselves. **Figure 3.18** shows SEM EDS measurements from a growth that

occurred after switching to the graphite target holder. Growths such as this one did not possess any copper EDS peaks.

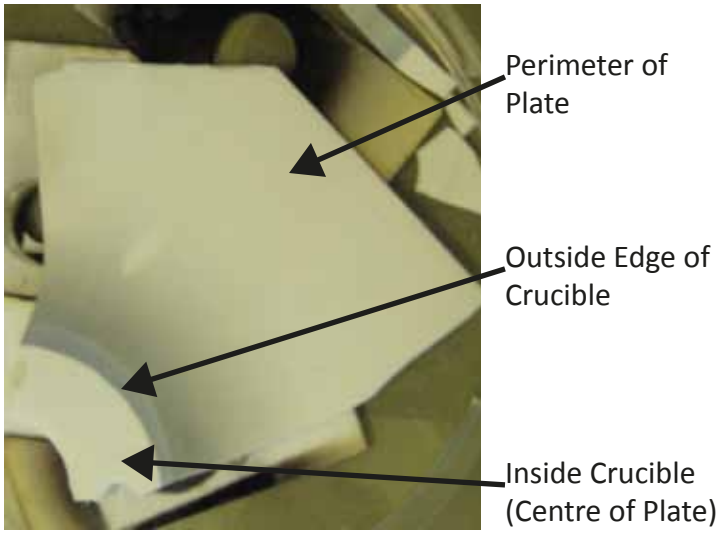

Figure 3.16: A retrieved piece of the fractured top alumina plate from the "Mark 1" design. This photograph provides visual evidence of tungsten outgassing during heating of the furnace. The portion of the plate shielded by the crucible appears visibly whiter compared to the graduation of grey material present outside the crucible edge.

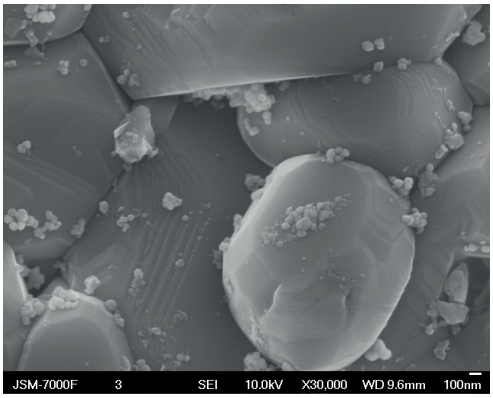

a)

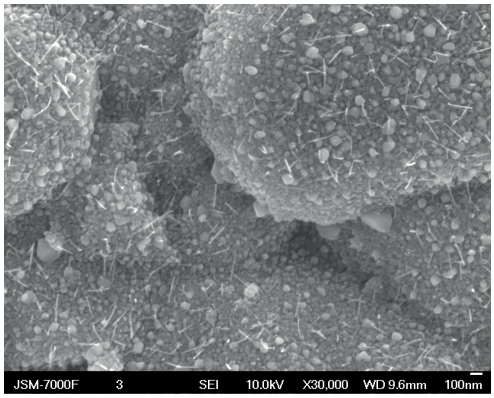

b)

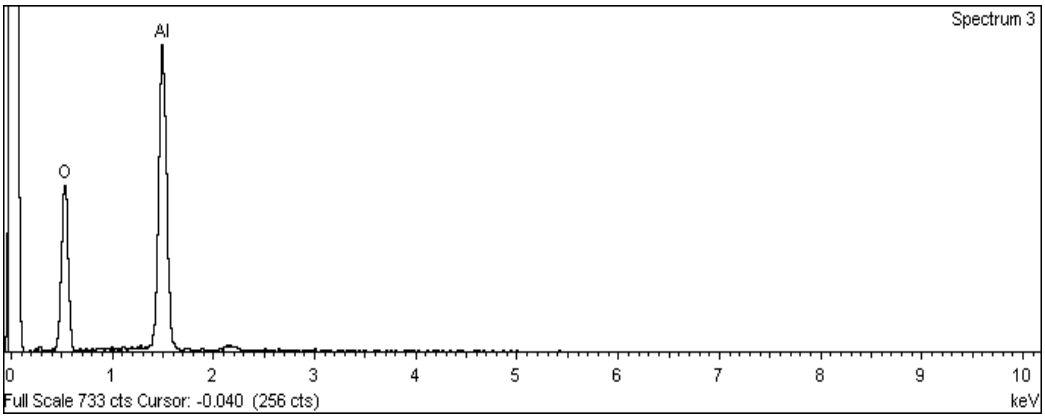

c)

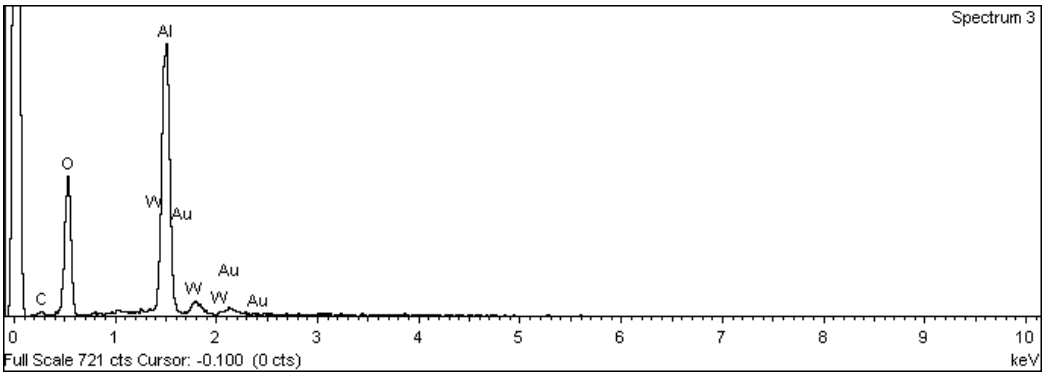

d)

Figure 3.17: SEM Images and EDS Spectra of Fractured Alumina Plate shown in Figure 3.16. Figures 3.17a and 3.17b show SEM images representative of surfaces located within the crucible region and grey material gradation, respectively. Figures 3.17c and 3.17d contain point EDS spectra corresponding to these regions.

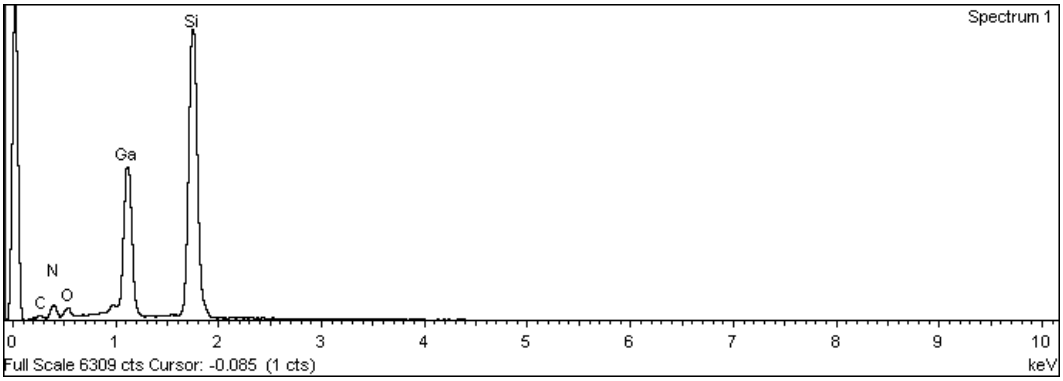

Figure 3.18: Example of SEM EDS Measurements Following the Installation of the Graphite Target Holder. Figure 3.18 illustrates a typical EDS spectrum from growths conducted after the introduction of a graphite target holder. Point EDS measurements such as these lacked copper peaks. This spectrum was taken from nickel region of sample 45 (748°C, 425 W).

4. Experiments

4.1 Introduction

In this chapter, results from nanowire growth experiments using gold, platinum, and nickel catalysts are discussed in sections 4.2 to 4.4.

4.2 Gold Catalyst Experiments

4.2.1 Growth Conditions

Twenty-four experiments were conducted in which gold was employed as a possible VLS catalyst in order to sweep a large multivariate growth parameter matrix for potential conditions conducive to gallium nitride nanowire growth. Of these twenty-four attempts, eighteen were completed, while six instances had to be curtailed prematurely due to equipment problems. The experimental variables that were systematically iterated through include: substrate temperature, DC magnetron power, growth length, and incident flux composition. The five initial experiments used a 1 nm thick layer of gold; this was changed to 4 nm for the remainder of experiments. A summary of the permutations of growth parameters investigated is shown in **Table 4.1**. All gold catalyst experiments were conducted on (111) silicon wafers while using the Mark 2 furnace design with the molybdenum radial shielding.

	Experimental Values
Substrate Growth Temperature [°C]	743 – 892
DC Magnetron Power [W]	65, 70, 75, 80, or 100
Growth Duration [minutes]	15 (n=8), 30 (n=6), or 60 (n=4)
Flux Composition	Gallium + Nitrogen, or Gallium followed by Gallium + Nitrogen
Catalyst thickness [nm]	1 or 4

Table 4.1: Summary of Growth Parameters for Gold Catalyst Experiments. Here, the number of samples is represented by the variable "n".

4.2.2 Experimental Results

As mentioned previously, the gold cohort experiments set out to explore a wide parameter space for suitable growth conditions. In doing so, a large number of experiments did not yield any gallium nitride nanowires. In these cases, there was thin film growth in both the exposed gold and non-gold regions. Figure 4.1 showcases examples of observed gallium nitride thin film growth at different temperatures. Figure 4.1a displays a thin film from sample 7 (743°C, 381 W), an experiment in which gold was not deposited, as it was designed to verify the ability of the Mark 2 furnace to grow gallium nitride thin films. Here, the grain sizes appear in the 100-to-200 nm range, after a 30-minute growth. Figure 4.1b, in contrast, highlights gallium nitride thin film growth in the non-gold region of sample 15 (430 W). The exact temperature of this growth is unknown as there were problems with the thermocouple during the experiment. In this experiment (and two others where similar problems occurred), input furnace power was used a surrogate measurement for temperature. These input powers were compared to the Mark 2 furnace temperature calibration curve shown in Figure 3.13 and the growth temperature was estimated. In the case of sample 15, the input power corresponded to

a growth temperature of approximately 868°C. The thin film shown in Figure 4.1b also had grain sizes ranging between 100-200 nm after a 30-minute growth. The point EDS measurements of such films (see Figure 4.1c) produced demonstrable gallium, nitrogen, oxygen and silicon peaks, lending credibility to the fact that these films may be gallium nitride. The lack of tungsten peaks also support the efficacy of the Mark 2 design to prevent such contamination. An interesting development was the identification of a copper peak at approximately 1 keV mark, preceding the gallium peak, while performing EDS on samples. While a small peak at this energy in a sample containing gallium is typically also correlated with gallium, INCA software found many instances of copper across samples. These copper results prompted the consideration of copper debasement from somewhere in the deposition system. As mentioned in chapter 3, this source of copper contamination was eventually determined to be the gallium target holder, and was replaced with a graphite holder following the gold catalyst experiments. At this time, INCA ceased to identify copper as a probable constituent.

Five growth experiments resulted in nanowire-like structures growing only in the regions where gold had been deposited. In these samples, these nanowires grew only near the edge of the aperture; these regions extended no more than approximately 100 microns in from the edge. Progressing inwards from the aperture edge, thin film growth tended to dominate in the gold region. Of the five samples, only four produced reasonable amounts of nanowires to warrant TEM analysis: sample 13 (794°C, 414 W), sample 15 (430 W), sample 17 (455 W), and sample 19 (478 W). Using Figure 3.13, the estimated temperatures for the latter three growth experiments were 868°C, 883°C,

and 897°C respectively. Of these three growths, nanowires were only successfully isolated for TEM analysis from samples 15 and 17.

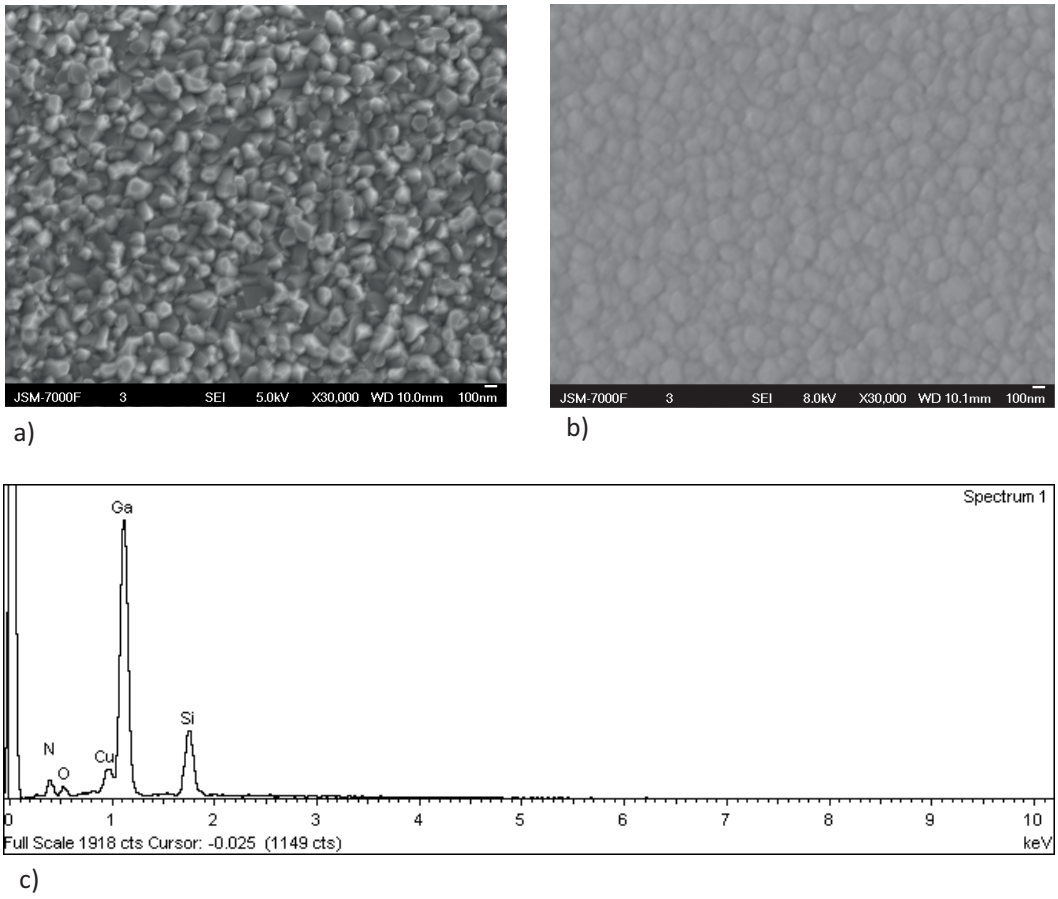

Figure 4.1: SEM Images of Some Gallium Nitride Thin Films Grown During Gold Catalyst Experiments**.** Figure 4.1a shows a SEM image of a thin film that grew on sample 7 (743°C, 381 W) after 30 minutes (0° tilt angle). Sample 7 was grown catalyst-free. Figure 4.1b shows a resulting thin film that grew in the non-gold region of sample 15 (estimated temperature of 868°C, 430 W) (0° tilt angle). Sample 15 was a 30-minute experiment involving a variation of the DC magnetron power: the first 15 minutes were at 100 W, and the last 15 minutes were at 80 W. Figure 4.1c shows the SEM EDS results of the thin films in Figure 4.1a.

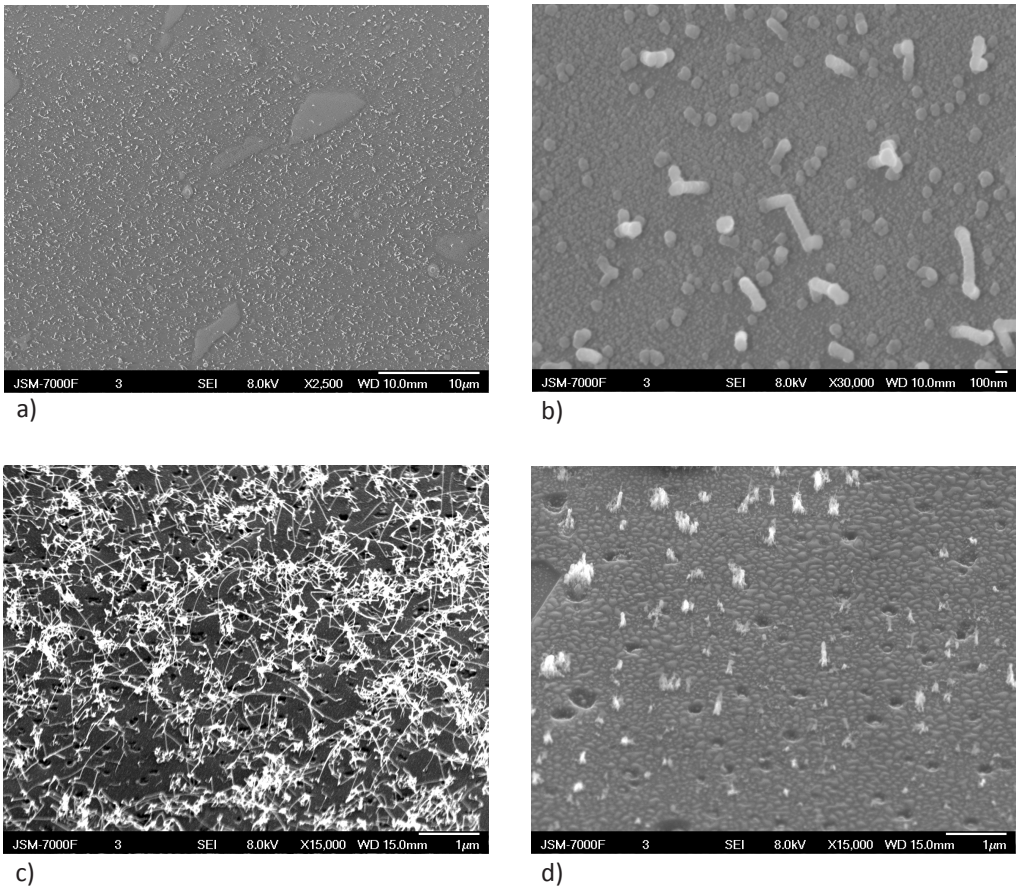

Figure 4.2: Nanowire-like Structures Found in Gold Catalyst Experiments. Figures 4.2a-b and figures 4.2c-d contain 45° tilt angle SEM images of nanowire-like structures found near the aperture edge on samples 15 (estimated temperature of 868°C, 430 W) and 17 (estimated temperature of 883°C, 455 W), respectively. Figure 4.2d presents nanowires located further inwards from the edge on sample 17.

Figure 4.2 presents examples of the nanowire-like structures observed in samples 15 and 17. At some point during the experiment (most likely during loading), sample 15 moved with respect to the aperture and caused only a small portion of the gold region to be exposed to incident fluxes. This area was ubiquitously covered with randomly oriented, nanowire-like structures shown in Figures 4.2a-b. These structures showed visually rough appearances under SEM. Nanowires found near the aperture

edge in sample 17 are shown Figure 4.2c; the diameter of these structures appeared to be less than 50 nm, much smaller than those found further inwards on the same sample (Figure 4.2) and in sample 15. In fact, a number of nanowires on sample 17 were found to have diameters between 10 and 20 nm while using TEM. TEM analysis of nanowire structures from sample 15 and 17 corroborated that the surfaces of the wires were indeed rough (see Figure 4.3). More evidence to suggest that these wires were not single crystalline can be seen by the annular SAD patterns taken along the shaft of a nanowire, such as that shown in Figure 4.4. EDS and EELS measurements, such as those shown in Figures 4.5 and 4.6, confirmed the presence of gallium and nitrogen within the nanowire-like structures, respectively. While no tungsten being detected promising, gold was also not found to be present at discernable levels within the wires. Finally, the presence of copper in the TEM grids themselves precluded the ability to accurately assess whether or not copper contaminated the nanostructures.

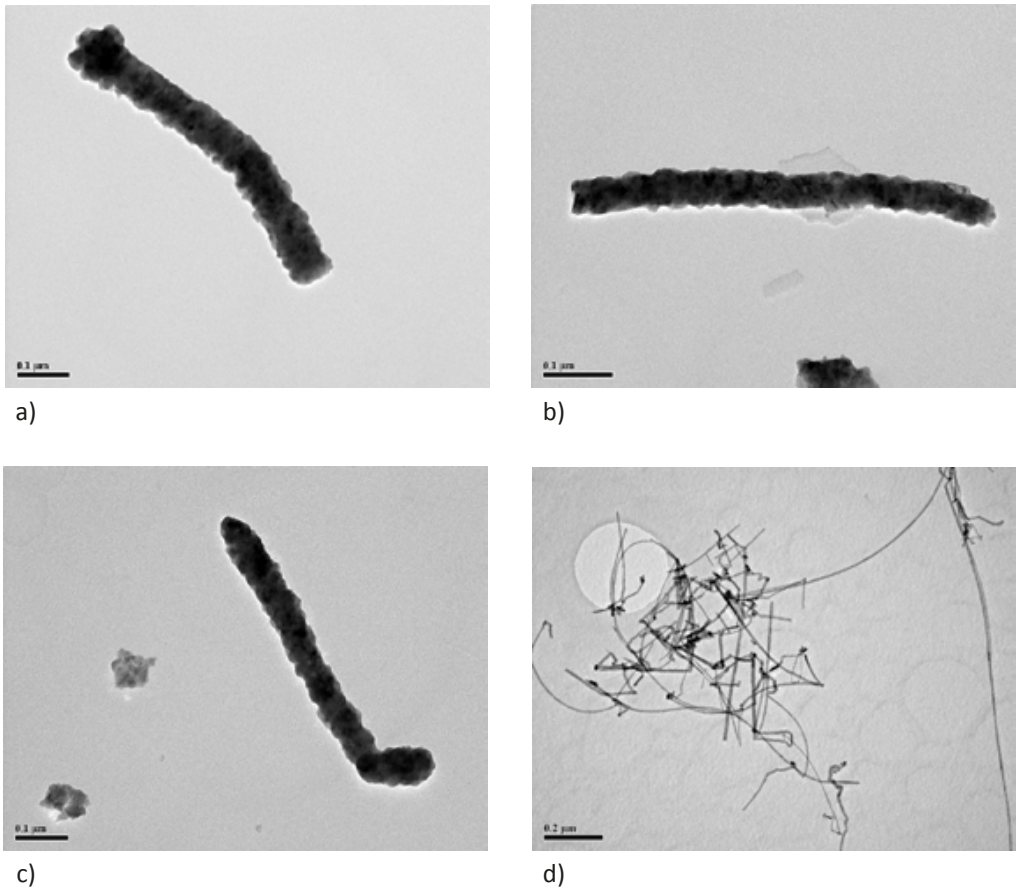

a) b)

c) d)

Figure 4.3: Bright-field TEM images of Nanowire-like Structures Found During Gold Catalyst Experiments. Figures 4.3a-c display examples of individual nanowires from sample 15 (estimated temperature of 868°C, 430 W). Figure 4.3d shows an aggregate of nanowires from sample 17 (estimated temperature of 883°C, 455 W).

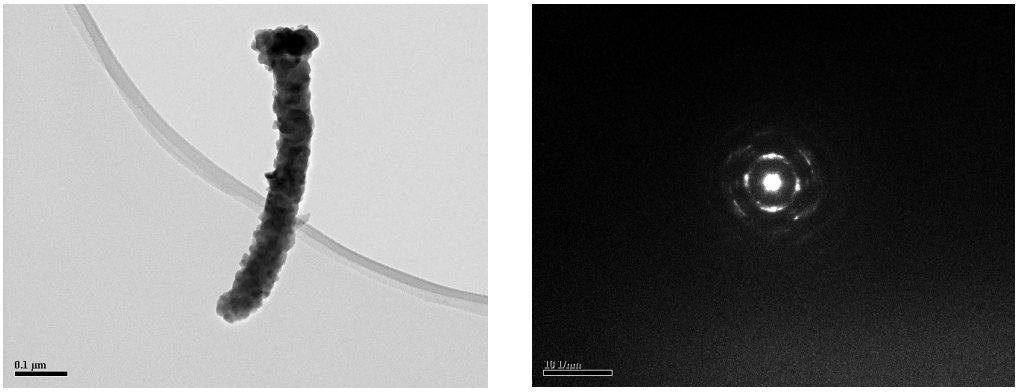

a) b)

Figure 4.4: Isolated Nanowire-like Structure and its Selective Area Diffraction Pattern. Figure 4.4a shows an isolated nanowire from sample 15 (estimated temperature of 868°C, 430 W). Figure 4.4b shows a SAD pattern taken from its shaft.

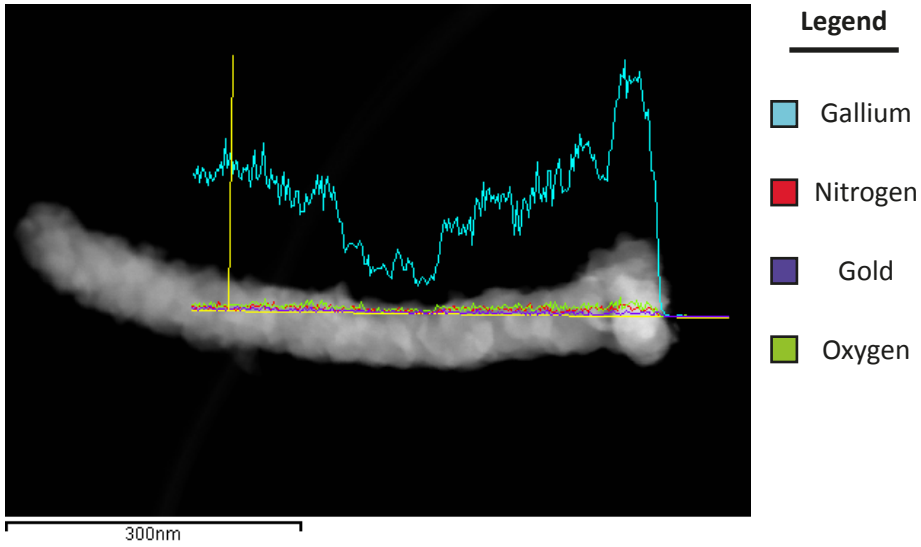

a)

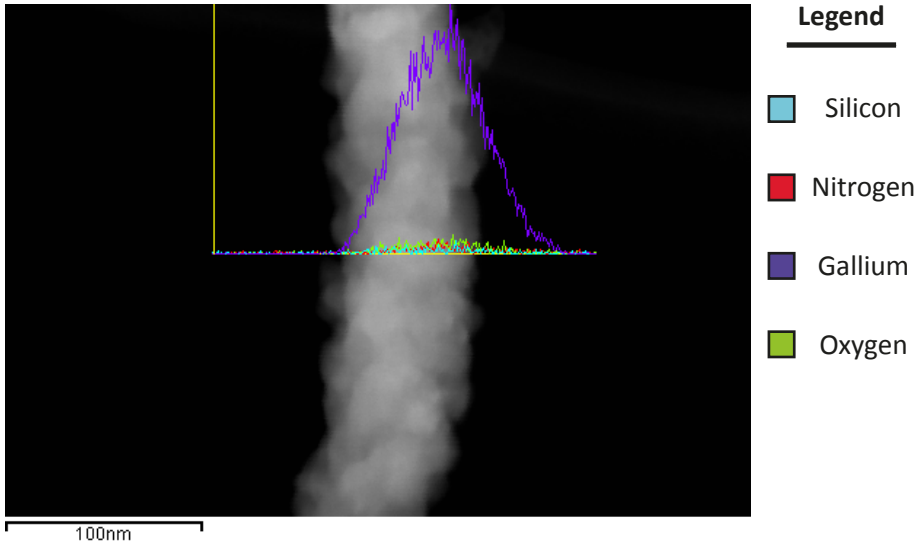

b)

Figure 4.5: Longitudinal and Transversal EDS Linescans of Isolated Nanowire. This figure shows EDS linescans on the same nanowire shown in Figure 4.4. Figure 4.5a shows the longitudinal EDS linescan, while figure 4.5b depicts the transversal EDS linescan, as captured by INCA software.

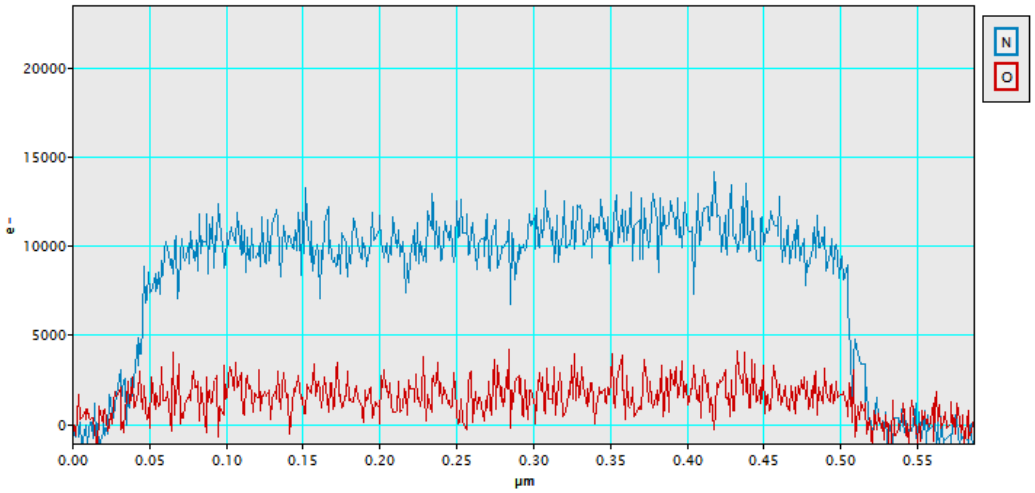

Figure 4.6: Nitrogen and Oxygen EELS Spectrum Example. This figure shows the longitudinal nitrogen and oxygen composite EELS spectra for a nanowire isolated from sample 15 (estimated temperature of 868°C, 430 W).

In summary, some of the experimental conditions using gold as a catalyst did produce nanowires. However, there were many shortcomings to these results. While there is evidence to suggest that resulting one-dimensional nanostructures are composed of gallium nitride, these structures are not single crystalline and possessed trace levels of contaminants. Moreover, their density was typically sparse.

4.2.3 Experimental Limitations

The gold catalyst experiments showed that gallium nitride nanowires could be grown via sputtering, albeit not of single crystal quality. The results for gold were inconclusive due to the presence of contaminants when the tests were performed. The optimal growth conditions may have also not have been tested. No growths were pursued using gold as a catalyst once the graphite holder had been installed due to time and resource constraints.

4.3 Platinum Catalyst Experiments

4.3.1 Growth Conditions

Platinum was used for eleven experiments as a catalyst for gallium nitride nanowire growth. One of these experiments could not be completed due to equipment problems. In this experimental cohort, the following conditions were used: a 4 nm thick catalyst layer, molybdenum radial heat shielding, Mark 3 furnace, 80 W DC magnetron power setting, a working pressure of approximately 10 mTorr, and argon and nitrogen settings on the rotameter corresponding to 24.8 std. mL/minute and 113.7 std. mL/minute, respectively. All growths were performed on platinum patterned (111) silicon wafers. Of the completed growth experiments, the initial eight experiments were performed for 30 minutes, while the final two experiments were 15 minutes in length. The final two experiments also were conducted following the replacement of the heating filament. Growth temperature effects on nanowire growth were explored by adjusting the input power from between 70% to 85% its maximum value; these settings correspond to an average output temperature ranging between 744°C and 898°C. Figure 4.7 outlines the input furnace power, furnace temperature, and duration of the growth experiments using platinum that were successfully completed.

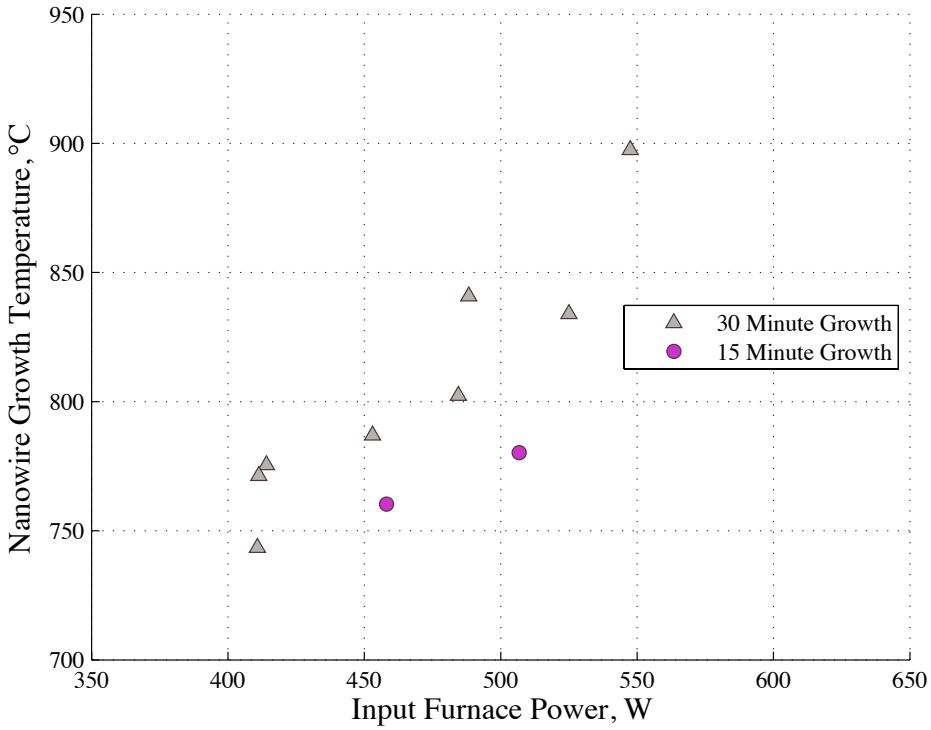

Figure 4.7: Input Furnace Power and Growth Temperature Plot for Platinum-Catalyst Nanowire Growth Experiments. Figure 4.X compares the input power to the substrate furnace and the realized growth temperature for platinum-catalyst nanowire experiments.

4.3.2 Experimental Results

The platinum catalyst experiments yielded mixed results. Each growth resulted conformal thin film coverage of both the platinum and non-platinum patterned regions of the (111) silicon substrate. Examples of typical thin films near the aperture edge are shown in Figure 4.8a-b for non-platinum and platinum areas. As illustrated in this figure, the surface morphologies of these different areas tended to be similar in appearance within a given sample. Also, point qualitative EDS measurements of these areas across different samples consistently showed definitive gallium and nitrogen peaks.

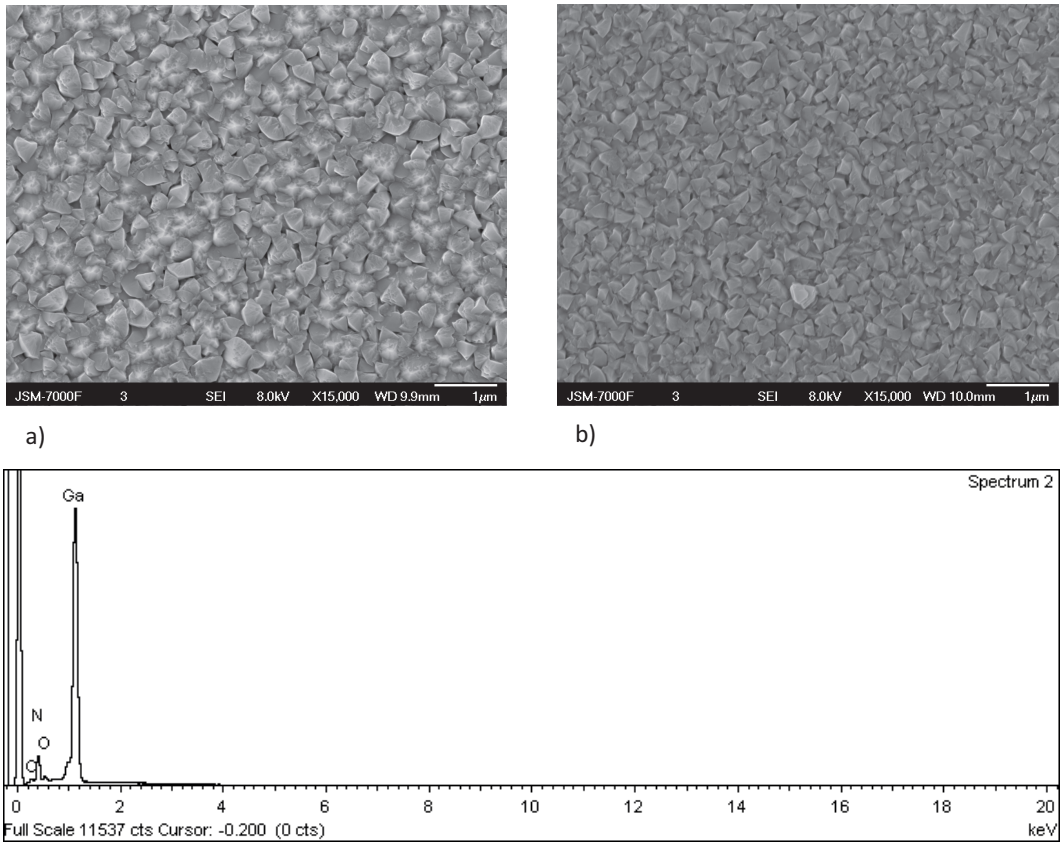

Figure 4.8: Typical Experimental Growth Results for Platinum and Non-Platinum Regions on (111) Silicon Substrate. Figure 4.8a and 4.8b depict the thin film growth observed near the aperture edges of sample 33 (898°C, 547 W) at 0° tilt angle. Figure 4.8c show the SEM point EDS spectrum taken from a thin film in the platinum region of the same sample.

Only two samples were found to have any nanowire-like structures. Figure 4.9 displays such structures found on samples 32 (841°C, 488 W) and 33 (898°C, 547 W). While these results were tantalizing, the relative sparseness of these structures precluded the desire to perform any TEM analysis.

In summary, there may be some potential for platinum as catalyst for the sputtering growth of gallium nitride nanowire. The experimental results from this cohort

were predominately negative, showing only probable gallium nitride thin film growth. However, given the limited number of trials, more investigation is required to fully assess other growth conditions.

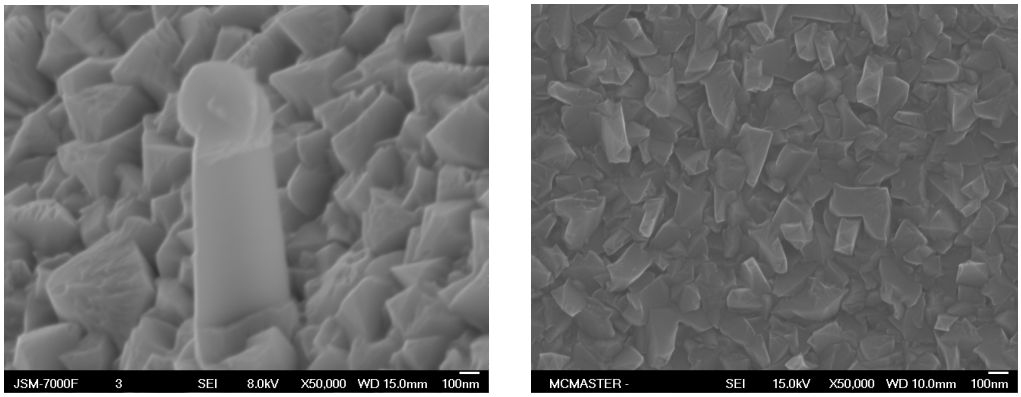

a) b)

Figure 4.9: Nanowire-like Structures Found in Platinum Catalyst Experiments. Figures 4.9a and 4.9b exhibit possible nanowire structures found in platinum covered regions in samples 32 (841°C, 488 W) and 33 (898°C, 547 W), respectively.

4.3.3 Experimental Limitations

Following the final four gold catalyst experiments, it was thought that a 60 minute-growth experiment was too long; a 30-minute growth window for selected for the new platinum catalyst cohort. After eight growths, it was adjusted to 15 minutes. In retrospect, it may have been prudent to examine shorter growth periods given the success observed during nickel catalyst experiments. Unfortunately, the shorter growths were restricted to cooler temperatures (i.e. 760°C and 780°C) due to time constraints. Subsequent experiments at higher temperatures were never performed and the research focus was shifted to nickel as a possible catalyst for gallium nitride nanowire growth. As can be seen Figure 4.9, some nanowire-like structures were observed during

the platinum experiments, but they were never at a sufficient density to warrant TEM analysis.

4.4 Nickel Catalyst Experiments

4.4.1 Growth Conditions

Ten experiments were carried out using nickel as a catalyst for gallium nitride nanowire growth; two of these investigations were curtailed prematurely due to equipment malfunction. During these experiments, the furnace configuration was the same as that used during previous platinum catalyst nanowire experiments (i.e. 4 nm thick catalyst layer, molybdenum shielding type, a magnetron power setting of 80 W, a working pressure of about 10 mTorr, argon and nitrogen flow settings, etc…). All growths that were successfully performed used nickel patterned (111) silicon wafers and were 15 minutes in length. The effect of growth temperature on gallium nitride nanowire growth was probed by varying the input power to the substrate furnace from 75% to 95% of its maximum input value. The resulting average temperature used during a growth ranged between 692°C and 860°C, based on the given input power setting. Figure 4.10 summarizes the relationship between average input power to the furnace and the average output temperature realized during deposition for the nickel catalyst experiments that were not terminated prematurely. All nickel-based nanowire growth experiments were performed using the Mark 3 furnace model.

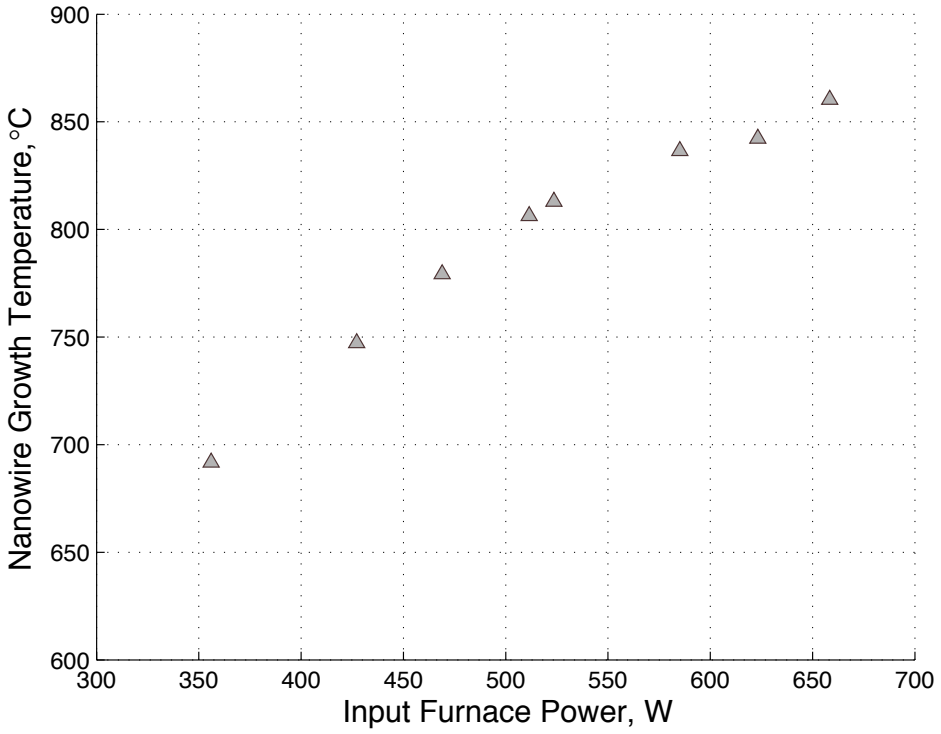

Figure 4.10: Input Furnace Power and Growth Temperature Plot for Nickel-Catalyst Nanowire Growths. Figure 4.10 compares the input power to the substrate furnace and the realized growth temperature for nickel-catalyst nanowire experiments.

4.4.2 Experimental Results

The introduction of nickel as a catalyst layer proved to be fruitful than gold and platinum. Each sample within the nickel cohort produced nanowires only in the regions covered with nickel that had been exposed to gallium and nitrogen fluxes during sputtering. The non-nickel covered region produced thin films of gallium nitride. This phenomenon is most aptly witnessed at the interface between the nickel and non-nickel covered regions. Figure 4.11 showcases this interface for three growths at 806°C, 837°C, and 860°C. These SEM images clearly illustrate the fact that the nanowire structures

arising from sputtering growths only occur in the nickel regions. In areas lacking the presence of nickel, only thin film growth occurred. Qualitative EDS measurements made on the SEM confirm that these thin film areas possess gallium and nitrogen peaks. Examining the nickel side of the interface, there is extensive coverage of nanowires. There also appears to be a temperature dependence on nanowire density. Beyond a certain temperature, both the quantity and density of nanowires decrease. An example of this phenomenon can be seen across samples that differed in growth temperature in the contrast between Figure 4.11a and 4.11d.

There is also evidence to suggest that a temperature gradient exists across an individual sample as well. The highest density of nanowires were concentrated near the aperture edge of the substrate holder and it decreased radially inwards. The size of this high-growth region varied with different growth temperature. Qualitatively, it was found to range from approximately a few hundred microns from the aperture edge in sample 37 (692°C at an input power of 356 W) to millimeters from the edge in sample 41 (807°C at an input power of 512 W) while using SEM. This region was seen to regress in subsequent growths at higher temperatures and input powers. These assertions are corroborated by Figure 4.12, which shows SEM images of nanowires from sample 41 at progressively more inward locations from the aperture edge. Here, the lengths, density, and absolute numbers of nanowires decreased radially towards the centre. At the centre of the nickel region exposed to the sputtering fluxes, film growth dominated nanowire growth. This was observed for all samples within the nickel cohort. Any nanowire populations found in the centre regions tended to be in their nascency and

were much sparser then those closer to the aperture edge. Figure 4.13 illustrates the film growth typically found at the centre of the nickel-region.

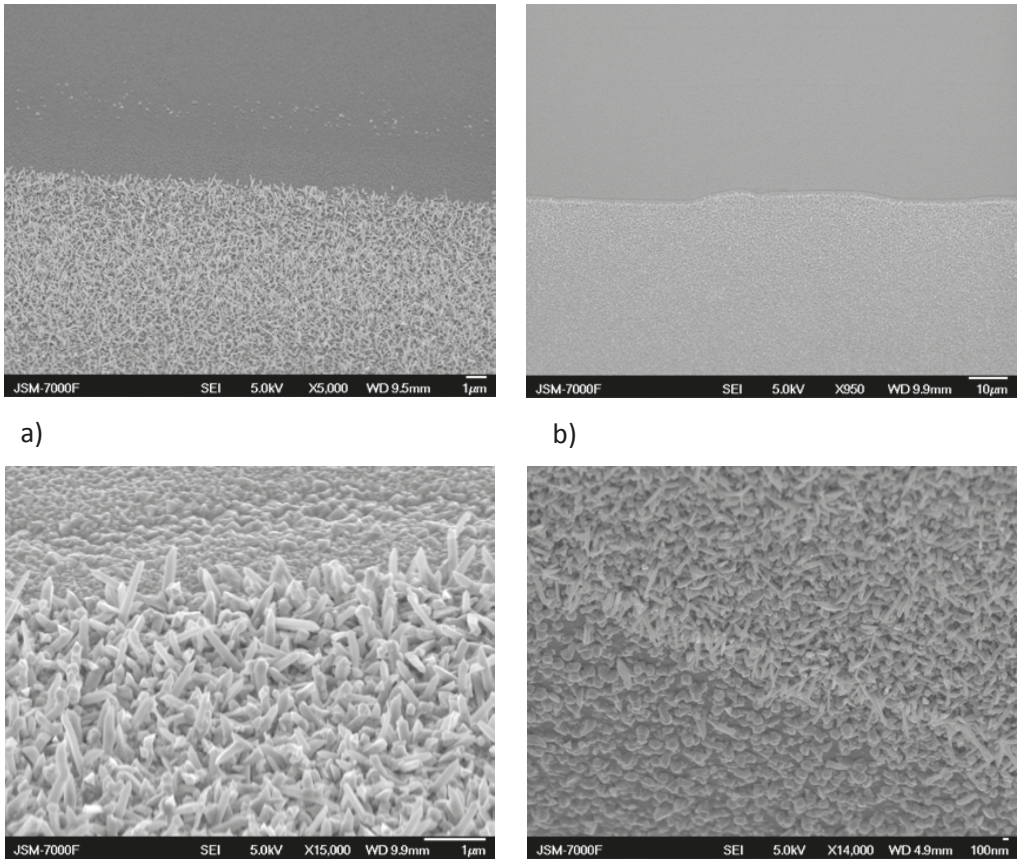

Figure 4.11: SEM images of the Nickel/No-Nickel Interface at 45° angle tilt. Figure 4.11a shows the nickel/no-nickel for sample 41, which was grown at 806°C. Here, the nickel region containing the nanowires is located below the interface. Figure 4.11b shows the nickel/no-nickel interface for sample 42, which was grown at 837°C. The nickel region is also found below the interface. Figure 4.11c depicts the interface from Figure 4.11b at a higher magnification. Figure 4.11d shows the interface for sample 44, which was grown at 860°C. Here, the nickel region is located above the interface.

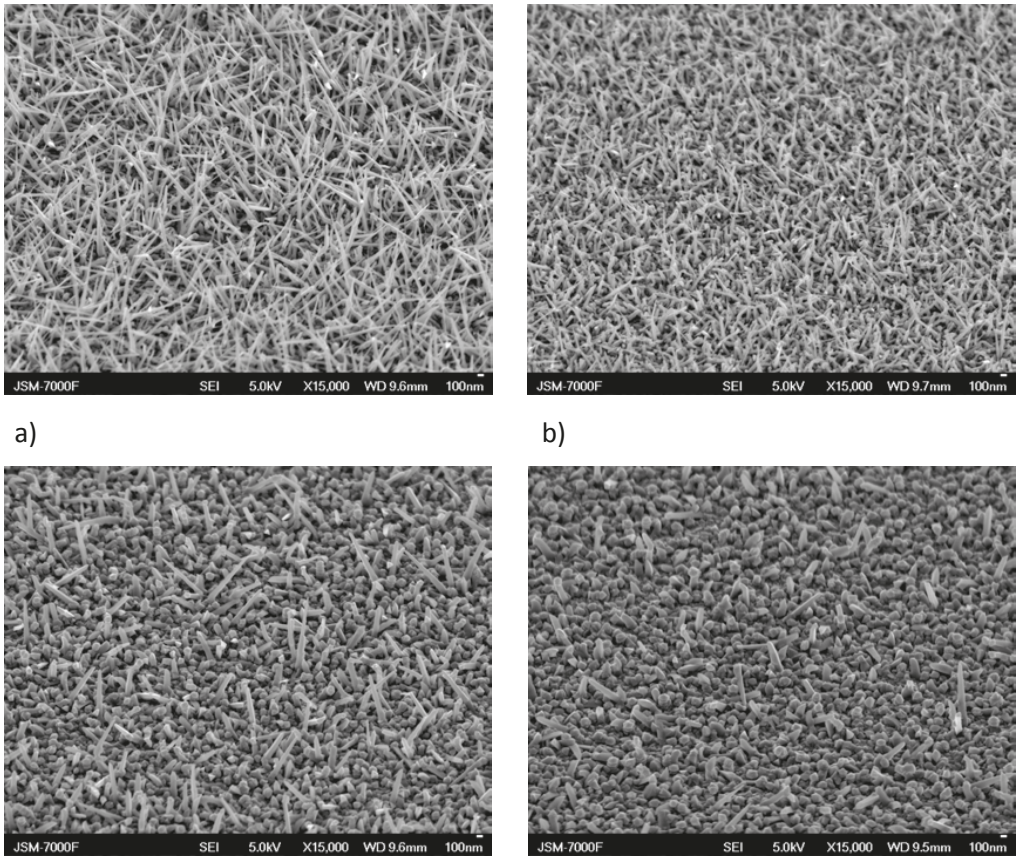

Figure 4.12: SEM Images of Nanowires on Nickel Region of Sample 41 (806°C, 15 minutes) at a 45° angle tilt. This figure presents SEM images of nanowires taken across approximately millimetres, from the aperture edge inwards. Figure 4.12a depicts nanowires near the edge of the aperture, while figures 4.12b-d show images progressively towards the centre of the sample.

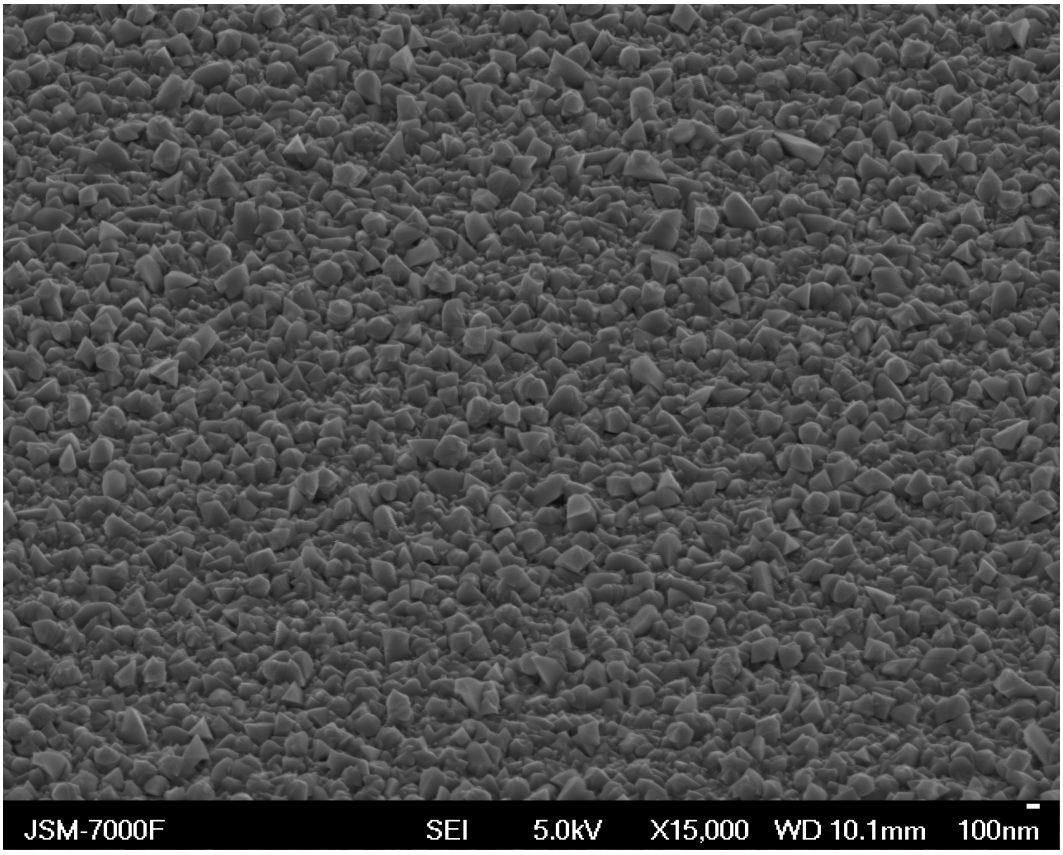

Figure 4.13: SEM Images of Thin Film Growth at Centre of Nickel Region at a 45° angle tilt. This image is taken from sample 39, which is a 15-minute growth at 745°C. The film growth shown above illustrates what was typical for the central portion of the nickel region of samples.

Examination using SEM showed that the resulting nickel cohort nanowires were visually smooth in appearance, much more so than those isolated during previous gold catalyst experiments while using the new substrate furnace. Figure 4.14 illustrates the random growth directions of the resulting nanowires to the (111) silicon wafer surface. There were a considerable number of instances in the collected SEM images, regardless of growth temperature, where the nanowires were witnessed to typically possess triangular cross-sections, such as those shown in Figure 4.14d. This particular image was chosen to show the cross-sectional shape because it showed the shape clearly at a

growth direction that was not perpendicular to the wafer surface. The presence of triangular nanowire cross-sections is worth mentioning because gallium nitride nanowires have been grown with such cross-sections[77]. Another characteristic of the resulting nanowires was tapering. These were various degrees of tapering, from subtle tapering effects to tapering to extremely fine tips that appeared almost translucent under SEM. This tapering effect seemed to exhibit a temperature relationship: the number and density of completely tapered nanowires increased from sample 37 (692°C, 356 W) and peaked in sample 41 (806°C, 512 W). Higher growth temperatures than those used for sample 41 showed increased amounts of subtle tapering. The tapering effect was also more prominent towards the aperture edge, closer to the heating element. Figure 4.14a to 4.14c showcase these tapering effects in sample 41 and in sample 42 (837C, 585 W). The random orientation and the tapering nature of the nanowires made it difficult to accurately measure the lengths and diameters of nanowires following a growth. Qualitatively, the lengths of nanowires increased from a couple hundred nanowires at colder temperatures to well over microns at elevated ones used in subsequent growths. Finally, there was no conclusive evidence from SEM analysis to show nickel at the nanowire tips.

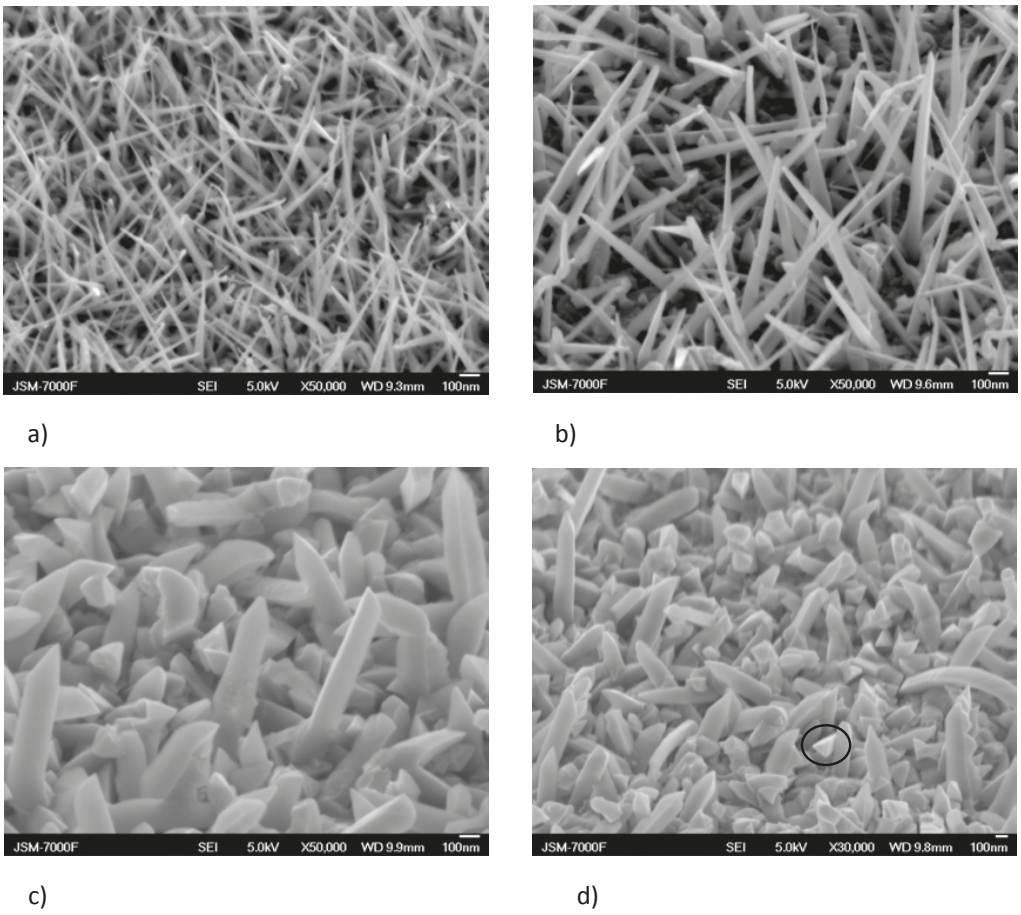

Figure 4.14: SEM Exposition of Nickel Experiment Nanowires**.** All images are taken at a 45° angle tilt. Figures 4.14a and 4.14b show the resulting nanowires in the high growth region of sample 41 (806°C, 512 W). Higher degrees of nanowire tapering can be seen in Figure 4.14a, which was taken closer to the aperture. Figures 4.14c and 4.14d show the resulting nanowires in the high growth region of sample 42 (837°C, 585 W). The circular annotation on Figure 4.14d is placed to clearly show the triangular cross-section of a nanowire.

Once SEM analysis verified the presence of nanowires following a growth experiment, the nanowires were isolated and examined using TEM to investigate their quality and composition. In total, nineteen nanowires from three experiments were analyzed. Selective area diffraction (SAD) patterns of individual nanowires were collected to determine crystalline quality. Each of these patterns consistently showed

that the nanowires were single crystalline, rather than polycrystalline like earlier gold experiments. Figure 4.15 shows SAD patterns of three different nanowires from three different growth temperature experiments 747°C (Sample 39), or 806°C (Sample 41), or 813°C (Sample 40). Following SAD collection, the TEM was then operated in STEM mode to probe the chemical composition of the isolated nanowires. EELS spectroscopy consistently identified discernable levels of nitrogen within the nanowires. The nitrogen peak of a non-integrated EELS spectrum and the integrated EELS spectrum along the nanowire in Figure 4.15c is shown in Figure 4.16 as an example of this analysis. Moreover, EDS linescans determined that gallium was also presence in the nanowires. Figure 4.17 depicts longitudinal and transversal EDS linescans of the same nanowire as Figure 4.15c. Unfortunately, negligible amounts of nickel were detected during EDS scans within nanowires.

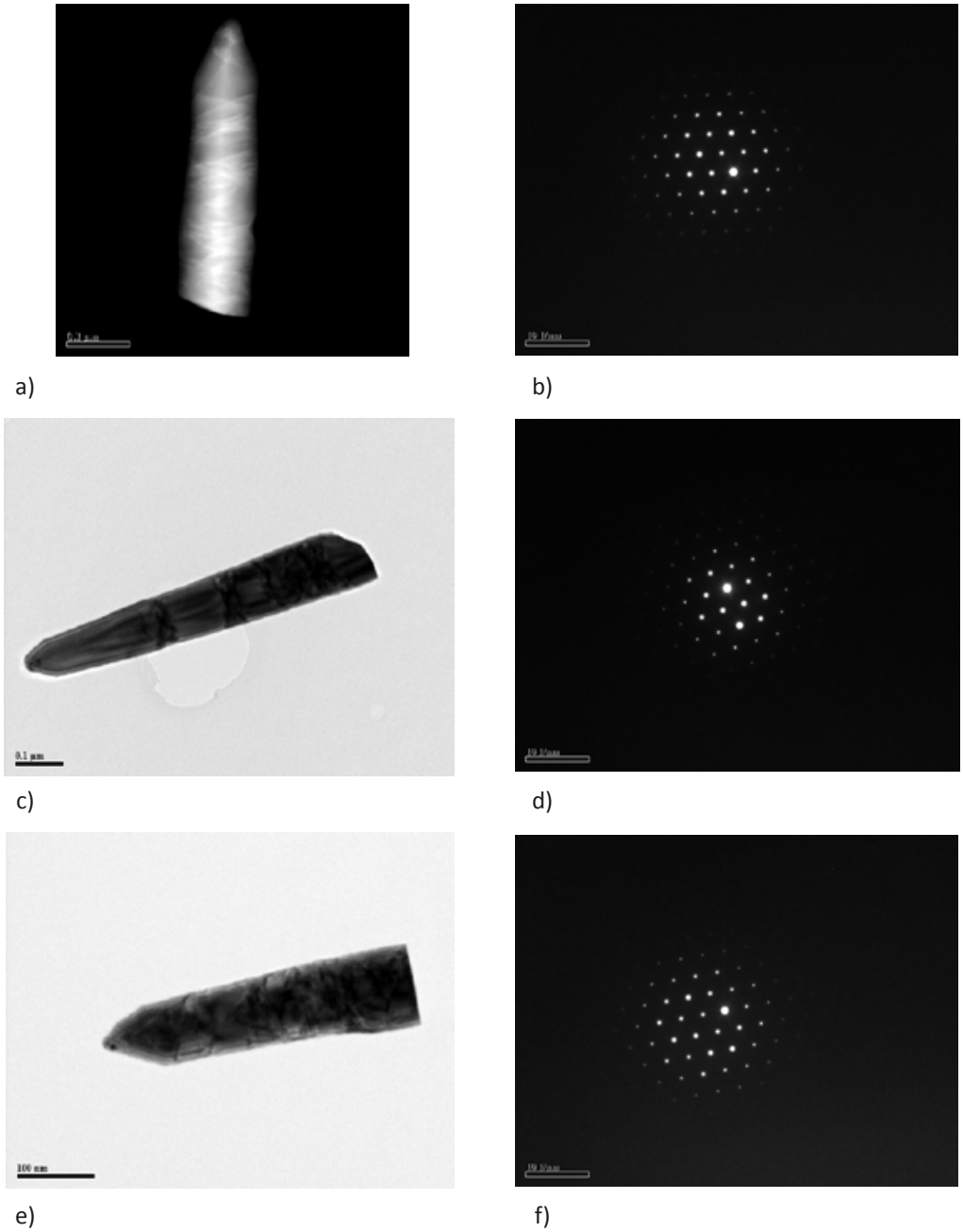

Figure 4.15: Single Crystal Selective Area Diffraction Patterns of Isolated Nanowires. Figures 4.15a-b show a high-angle annular dark-field STEM image of a nanowire from sample 39 (745°C, 427 W) and its corresponding SAD pattern. Figures 4.15c-d show a bright-field TEM image of a nanowire from sample 40 (813°C, 524 W) and its corresponding SAD pattern. Figures 4.15e-f show a bright-field TEM image of a nanowire from sample 41 (806°C, 512 W) and its corresponding SAD pattern.

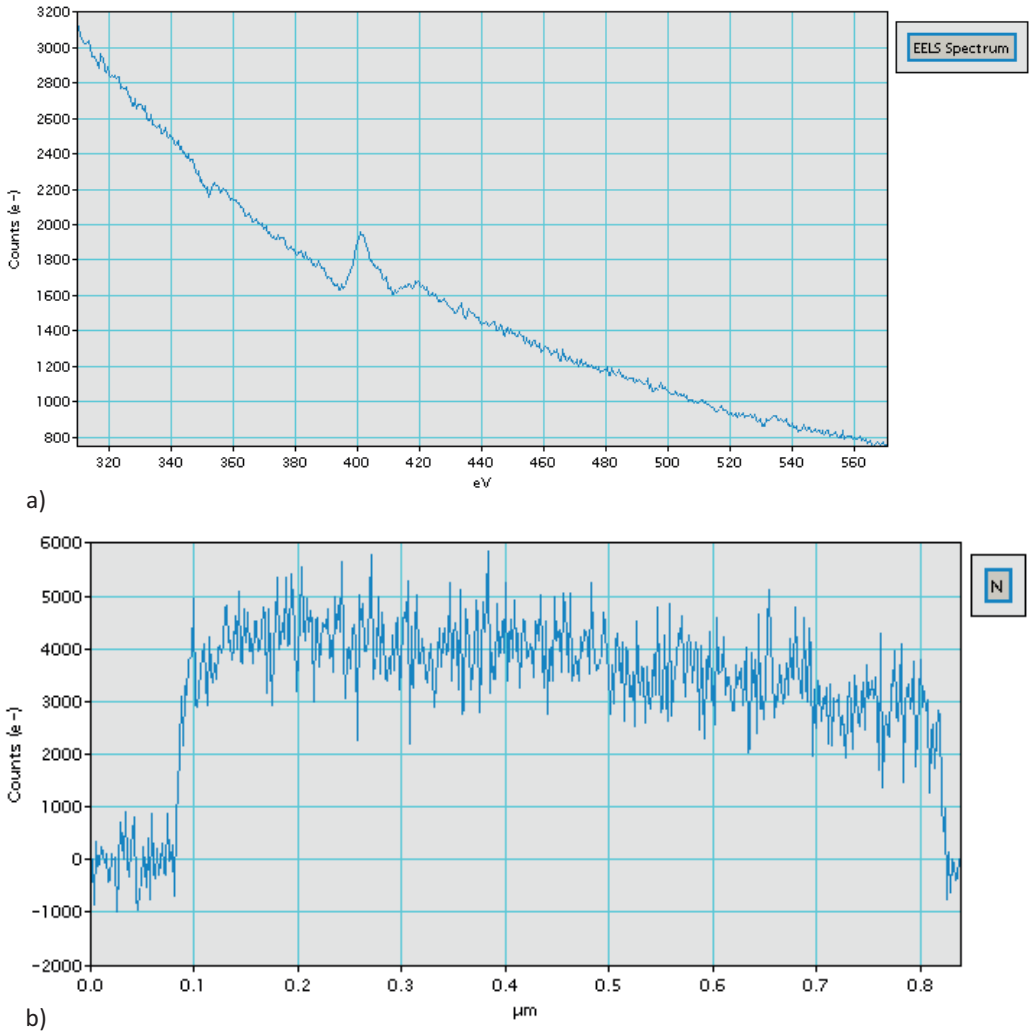

Figure 4.16: EELS Spectrum of Isolated Nanowire. This figure shows the nitrogen EELS spectrum for a nanowire isolated from sample 40 (813°C, 524 W). This wire was approximately 730 nm in length. Figure 4.16a shows the non-integrated EELS spectrum with the nitrogen peak at about 403 eV. Figure 4.16b shows the integrated composite EELS spectrum for nitrogen along the length of this nanowire.

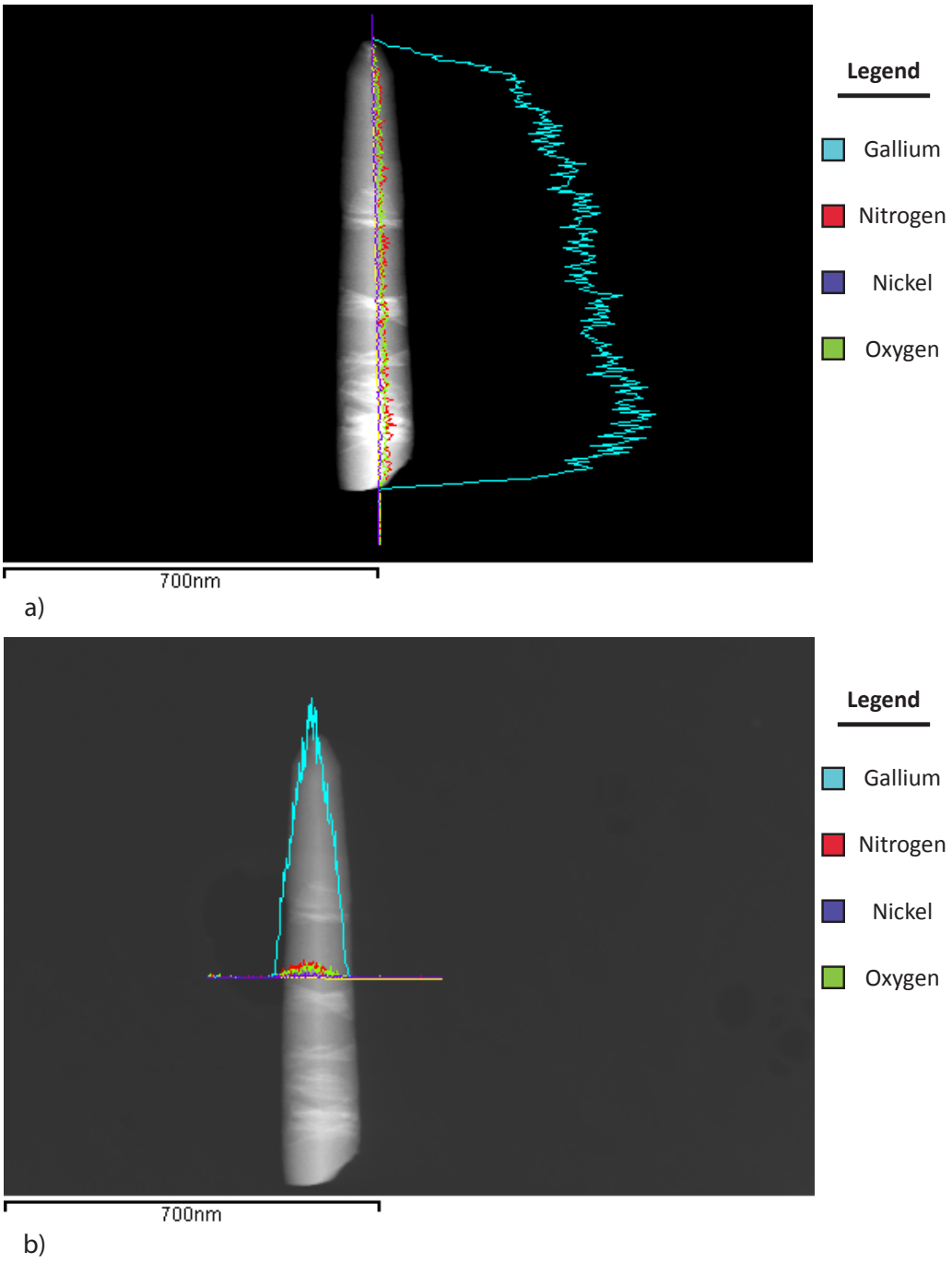

Figure 4.17: Longitudinal and Transversal EDS Linescans of Isolated Nanowire. This figure shows EDS linescans on the same nanowire that had the EELS performed on it in the previous figure. Figure 4.17a shows the longitudinal EDS linescan, while figure 4.17b depicts the transversal EDS linescan, as captured by INCA software.

There is further evidence to suggest that the nanowires from the nickel catalyst experiments were gallium nitride in composition. Selected area diffraction patterns were collected from a total of nineteen nanowires across three experiments using TEM. These single crystal nanowires were grown at either 747°C, or 806°C, or 813°C. resulting SAD patterns were analyzed using Gatan Digital Micrograph software to determine the average spacing between diffraction planes; These results were then compared with hexagonal gallium nitride reference data from the 2003 JCPDS International Centre for Diffraction Data provided by the Canadian Centre for Electron Microscopy at McMaster University. The results for each of these three samples are summarized in Table 4.2. The measured diffraction plane distances appear to correspond reasonably well to (100), (101), (102), (103), and (104) crystal planes found in a hexagonal gallium nitride crystal. The average measured distances and those of comparable planes differed by 1.76% or less. These discrepancies may have arisen from operator error during the alignment of the nanowire for SAD collection or when measuring the reciprocal lattice spacings. Nevertheless, these diffraction data provide more credence to the hypothesis that these nanowires are likely wurtzite gallium nitride.

In summary, both SEM and TEM analysis of multiple nanowires from nickel experiments provide reasonable evidence that gallium nitride nanowires did indeed grow via DC reactive magnetron sputtering of nitrogen gas and elemental gallium. These resulting nanowires appear to be single crystal and wurtzite. They only grew in regions where nickel had been deposited prior to growth and no nickel particles were found on the tips of nanowires.

Reference		Experimental Results			
Plane (hkl)	Plane Spacing (nm)	Sample Number	Number of Wires Examined	Average Plane Spacing (nm)	Percentage Difference Between Values (%)
100	0.2762	39	3	0.280 ± 0.002	1.38
103	0.14649	39	3	0.149 ± 0.012	1.71
100	0.2762	40	5	0.280 ± 0.001	1.38
102	0.1891	40	5	0.190 ± 0.006	0.48
103	0.14649	40	5	0.148 ± 0.001	1.03
104	0.11737	40	5	0.117 ± 0.028	0.32
100	0.2762	41	11	0.279 ± 0.001	1.01
101	0.2437	41	11	0.248 ± 0.002	1.76
102	0.1891	41	11	0.192 ± 0.001	1.53
103	0.14649	41	11	0.149 ± 0.001	1.71

Table 4.2: Comparison of the crystal plane spacings of GaN nanowires grown using a nickel catalyst to bulk GaN reference data. Table 4.2 compares the average spacing of crystal planes extracted from single crystal selective area diffraction patterns of gallium nitride nanowires grown by sputtering to bulk reference data from the 2003 JCPDS International Centre for Diffraction Data.

4.4.3 Experimental Limitations

While these experiments showed that the nickel catalyst layer was critical to the sputtering growth of gallium nitride nanowires, the exact nature of the catalyst during growth was not examined in detail. The two final nickel catalyst growth experiments were to be the initial parts of a series of experiments that investigated nanowire growth at shorter intervals than 15 minutes (i.e. 30 seconds, one minute, five minutes, etc…). The use of shorter growth durations was posited as a means to determine how the nickel layer changes with different exposures to incoming gallium and nitrogen fluxes.

However, as mentioned previously, both of these experiments had to be stopped prematurely during to a malfunction within the sputtering system. Further experiments were not pursued due to a multitude of reasons, including time and resource constraints.

Another limitation was related to the TEM analysis of the resulting nanowires. While all samples were examined using scanning electron microscopy techniques, not all of the samples were prepared for transmission electron microscopy. This is in large part due to volume considerations (i.e. the number of samples and the corresponding number of nanowires isolated from a sample) and time constraints. That being said, the TEM images of nanowires across samples tended to be similar.

5. Closing Remarks and Future Work

5.1 Closing Remarks

The primary objective of this thesis was to growth single-crystal gallium nitride nanowires using DC reactive magnetron sputtering. This objective was achieved through the design and development of a customized furnace and iteratively investigating different growth conditions. The ability to conduct growth experiments at temperatures in excess of 800°C and the removal of impurities, such as tungsten and copper, facilitated these goals. Nanowires grew only in regions where metal catalysts were present. Of the catalysts employed, nickel was the only catalyst to produce single crystal gallium nitride nanowires over large areas. It is quite possible that the optimal growth conditions for gold and platinum catalysts were not investigated given the time and resource constraints inherent to a Master's thesis. While the experimental results retrieved clearly suggest that catalysts are required for nanowire growth, no catalyst tips or discernable concentrations of the metals were found in nanowires examined using TEM. The exact nature of the catalyst remains elusive and is beyond the objectives of this thesis.

5.2 Future Work Suggestions

The results of this thesis provide motivation to further investigate and optimize large-area deposition techniques for the commercialized production of gallium nitride nanowires. While this thesis demonstrated that it is possible to use DC reactive magnetron sputtering to grow gallium nitride nanowires, there is still more work to be done before it can be a serious competitor to entrenched technologies.

Going forward, the exact role of the metal catalyst in growing nanowires under sputtering conditions needs to be elucidated. As previously mentioned, shorter growth experiments were attempted during this thesis as a means to investigate this process, but they were never successfully completed, nor were they prioritized. Perhaps, conducting growth experiments over very short time intervals will allow one to see the changes in the catalyst with increasing exposure to discrete amounts of the incident fluxes. The concatenation of these results may provide insight into the transient behaviour of the metal particle during the nanowire growth process. This process can be repeated for different metal catalysts and at different temperatures. Once these goals are completed, studying the behaviour of gallium as a potential self-catalyst for gallium nitride nanowires would be a step towards realizing the creation of sputtered GaN nanowire devices that are compatible with conventional CMOS processes.

Ultimately, there needs to be research relating to the production of devices via this procedure. As such, the development of heterostructures is another logical avenue to pursue. The current deposition chamber consists of two sputtering magnetrons. This will permit the use of two targets, such as gallium and indium, during a given

experiment. A growth parameter matrix for these experiments can be constructed according to the literature and then evaluated. It would be of great interest to replace the current rudimentary rotameters with mass flow meters prior to starting this experiments, in order to allow for more meticulous control of the V/III ratio. A study of the ternary catalyst alloy may also be of interest. In addition to examining the electronic and optical properties of these devices once they have been grown, creating device arrays may be another tangent worth investigating. The incorporation of pre-growth techniques, such as selective area epitaxy, may also allow one to standardize the dimensions of the devices and their direction of growth. These research suggestions are some of the many possible avenues to pursue going forward.

6. Bibliography

1. Ambacher, O., *Growth and applications of Group III-nitrides.* Journal of Physics D: Applied Physics, 1998. 31: p. 2653-2710.

2. Hardy, M.T., et al., *Group III-nitride lasers: a materials perspective.* Materials Today, 2011. 14(9): p. 408-415.

3. Kikuchi, A., H. Hoshi, and K. Kishino, *Substrate Nitridation Effects on GaN Grown on GaAs Substrates by Molecular Beam Epitaxy Using RF-Radical Nitrogen Source.* Japanese Journal of Applied Physics, 1994. 33: p. 688-693.

4. Lin, M.E., et al., *p-type zincblende GaN on GaAs substrates.* Applied Physics Letters, 1993. 63: p. 932-933.

5. Nakamura, S., *GaN Growth Using GaN Buffer Layer.* Japanese Journal of Applied Physics, 1991. 30: p. L1705-L1707.

6. Wu, J., *When group-III nitrides go infrared: New properties and perspectives.* Journal of Applied Physics, 2009. 106.

7. Maruska, H.P. and J.J. Tietjen, *The Preparation and Properties of Vapor Deposited Single Crystalline GaN.* Applied Physics Letters, 1969. 15(10): p. 327-329.

8. Seghier, D. and H.P. Gislason, *Electrical characterization of Mg-related energy levels and the compensation mechanism in GaN:Mg.* Journal of Applied Physics, 2000. 88(11): p. 6483-6487.

9. Fritze, S., et al., *High Si and Ge n-type doping of GaN doping - Limits and impact on stress.* Applied Physics Letters, 2012. 100: p. 122104-1 - 122104-4.

10. Gotz, W., et al., *Activation energies of Si donors in GaN.* Applied Physics Letters, 1996. 68: p. 3144-3146.

11. Xu, X., et al., *Residual donors and compensation in metalorganic chemical vapor deposition as-grown n-GaN.* Journal of Applied Physics, 2001. 90(12): p. 6130-6134.

12. Steckl, A.J., et al., *Rare-Earth-Doped GaN: Growth, Properties, and Fabrication of Electroluminescent Devices.* IEEE Journal of Selected Topics in Quantum Electronics, 2002. 8(4): p. 749-766.

13. Xue, C., et al., *Fabrication of GaN nanowires by ammoniating Ga2O3 thin films deposited on quartz with radio frequency magnetron sputtering.* Nanotechnology, 2003. 14: p. 50-52.

14. Dong, Z., et al., *Synthesis of three kinds of GaN nanowires through Ga2O3 films' reaction with ammonia.* Physica E, 2005. 27: p. 32-37.

15. Dingle, R., et al., *Stimulated Emission and Laser Action in Gallium Nitride.* Applied Physics Letters, 1971. 19(5-7).

16. Akasaki, I., et al., *Effects of AlN Buffer Layer on Crystallographic Structure and on Electrical and Optical Properties of GaN and Ga1-xAlxN (0<x<0.4) Films Grown on Sapphire Substrate by MOVPE.* Journal of Crystal Growth, 1989. 98: p. 209-219.

17. O'Mahony, D., et al., *Free-standing gallium nitride Schottky diode characteristics and stability in a high-temperature environment.* Semiconductor Science and Technology, 2009. 24: p. 1-8.

18. Vetury, R., et al., *The Impact of Surface States on the DC and RF Characteristics of AlGaN/GaN HFETs.* IEEE Transactions on Electron Devices, 2001. 48(3): p. 560-566.

19. Asbeck, P.M., et al., *Piezoelectric charge densities in AlGaN/GaN HFETs.* Electronics Letters, 1997. 33(14): p. 1230-1231.

20. Sheppard, S.T., et al., *High-power microwave GaN/AlGaN HEMTs on semi-insulating silicon carbide substrates.* IEEE Electron Device Letters, 1999. 20(4): p. 161-163.

21. Wu, Y.-F., et al., *30-W/mm GaN HEMTs by field plate optimization.* IEEE Electron Device Letters, 2004. 25(3): p. 117-119.

22. Neufeld, C.J., et al., *High quantum efficiency InGaN/GaN solar cells with 2.95 eV band gap.* Applied Physics Letters, 2008. 93(143502-1 - 143502-3).

23. Matioli, E., et al., *High internal and external quantum efficiency InGaN/GaN solar cells.* Applied Physics Letters, 2011. 98(021102-1 - 021102-3).

24. Akasaki, I., et al., *Shortest wavelength semiconductor laser diode.* Electronics Letters, 1996. 32(12): p. 1105-1106.

25. Nakamura, S., et al., *InGaN/GaN/AlGaN-based laser diodes with modulation-doped strained-layer superlattices grown on an epitaxially laterally overgrown GaN substrate.* Applied Physics Letters, 1998. 72(2): p. 211-213.

26. Stevens, K.S., M. Kinniburgh, and R. Beresford, *Photoconductive ultraviolet sensor using Mg-doped GaN on Si(111).* Applied Physics Letters, 1995. 66(25): p. 3518-3520.

27. Nakamura, S., *Current Status of GaN-Based Solid-State Lighting.* MRS Bulletin, 2009. 34: p. 101-107.

28. Morkoc, H. and S.N. Mohammad, *High-Luminosity Blue and Blue-Green Gallium Nitride Light-Emitting Diodes.* Science, 1995. 267(5194): p. 51-55.

29. Kim, S.T., et al., *Preparation and properties of free-standing HVPE grown GaN substrates.* Journal of Crystal Growth, 1998. 194: p. 37-42.

30. Andre, Y., et al., *Low dislocation density high-quality thick hydride vapour phase epitaxy (HVPE) GaN layers* Journal of Crystal Growth, 2007. 306: p. 86-93.

31. Kim, D., et al., *Fabrication of C-Doped p-AlGaInN Light-Emitting Diodes by the Insertion of Al4C3.* Japanese Journal of Applied Physics, 2013. 52.

32. Lugani, L., et al., *Ultrathin InAlN/GaN heterostructures on sapphire for high on/off current ratio high electron mobility transistors.* Journal of Applied Physics, 2013. 113.

33. Araki, M., K. Hoshino, and K. Tadatomo, *Direct growth of a-plane GaN on r-plane sapphire substrate by metalorganic vapor phase epitaxy.* Physica status solidi c, 2007. 4(7): p. 2540-2543.

34. Beaumont, B., et al., *High quality GaN grown by MOVPE.* Journal of Crystal Growth, 1997. 170: p. 316-320.

35. Parikh, R.P. and R.A. Adomaitis, *An overview of gallium nitride growth chemistry and its effect on reactor design: Application to a planetary radial-flow CVD system.* Journal of Crystal Growth, 2006. 286: p. 259-278.

36. Koblmuller, G., et al., *Influence of Ga/N ratio on morphology, vacancies, and electrical transport in GaN grown by molecular beam epitaxy at high temperature.* Applied Physics Letters, 2010. 97.

37. Sanchez-Garcia, M.A., et al., *The effect of the III/V ratio and substrate temperature on the morphology and properties of GaN- and AlN-layers grown by molecular beam epitaxy on Si(1 1 1).* Journal of Crystal Growth, 1998. 183: p. 23-30.

38. Bockowski, M., *Bulk growth of gallium nitride: challenges and difficulties.* Crystal Research and Technology, 2007. 42(12): p. 1162-1175.

39. Amano, H., et al., *P-Type Conduction in Mg-Doped GaN Treated with Low-Energy Electron Beam Irradiation (LEEBI).* Japanese Journal of Applied Physics, 1989. 28(L2112-L2114).

40. Hemmingsson, C., et al., *Springer Handbook of Crystal Growth*, G. Dhanaraj, et al., Editors. 2010, Springer-Verlag Berlin Heidelberg: New York. p. 869-896.

41. Drygas, M., et al., *High temperature chemical and physical changes of the HVPE-prepared GaN semiconductor.* Materials Chemistry and Physics, 2010. 122: p. 537-543.

42. Richter, E., et al., *Hydride vapor phase epitaxy of GaN boules using high growth rates.* Journal of Crystal Growth, 2010. 312: p. 2537-2541.

43. Jacques, C. *Epi-Wafer Market to Grow to $4 Billion in 2020 as LED Lighting Zooms to $80 Billion*. 2013 [cited 2013 11-27-2013]; Available from: http://finance.yahoo.com/news/epi-wafer-market-grow-4-113000523.html.

44. Lucznik, B., et al., *Technology of Gallium Nitride Crystal Growth*, D. Ehrentraut, E. Meissner, and M. Bockowski, Editors. 2010, Springer-Verlag Berling Heidelberg: New York. p. 61-78.

45. Wang, X., et al., *Continuous-Flow MOVPE of Ga-Polar GaN Column Arrays and Core-Shell LED Structures.* Crystal Growth & Design, 2013. 13: p. 3475-3480.

46. Gmili, Y.E., et al., *Multilayered InGaN/GaN structure vs. single InGaN layer for solar cell applications: A comparative study.* Acta Materialia 2013. 61: p. 6587-6596.

47. Ban, V.S., *Mass Spectrometric Studies of Vapor-Phase Crystal Growth II. GaN.* Journal of the Electrochemical Society, 1972. 119(6): p. 761-765.

48. Devi, A., et al., *Materials Chemistry of Group 13 Nitrides.* Topics in Organometallic Chemistry, 2005. 9: p. 49-80.

49. Gibart, P., *Metal organic vapour phase epitaxy of GaN and lateral overgrowth.* Reports on Progress in Physics, 2004. 67: p. 667-715.

50. Jain, S.C., et al., *III-nitrides: Growth, characterization, and properties.* Journal of Applied Physics, 2000. 87: p. 965-1006.

51. Liu, Z., et al., *p-InGaN/AlGaN electron blocking layer for InGaN/GaN blue light-emitting diodes.* Applied Physics Letters, 2012. 101.

52. Kadir, A., et al., *Influence of group III and group V partial pressures on the size and density of InGaN quantum dots in MOVPE.* physica status solidi a, 2012. 209(12): p. 2487-2491.

53. Gamarra, P., et al., *Impact of the substrate and of the nucleation layer on the properties of AlGaN/GaN HEMTs on SiC.* Journal of Crystal Growth, 2013. 370: p. 282-287.

54. Akasaki, I., *GaN-Based p–n Junction Blue-Light-Emitting Devices.* Proceedings of the IEEE, 2013. 101(10): p. 2200-2210.

55. Tang, H. and J. Webb, *Molecular beam epitaxy for III-N materials*, in *III-Nitride Semiconductor Materials*, Z.C. Feng, Editor. 2006, Imperial College Press: London. p. 117-160.

56. Tang, H. and J. Webb, *Growth of high mobility GaN by ammonia-molecular beam epitaxy.* Applied Physics Letters, 1999. 74.

57. Botchkarev, A., et al., *Properties of GaN films grown under Ga and N rich conditions with plasma enhanced molecular beam epitaxy.* Journal of Applied Physics, 1995. 77(9): p. 4555-4458.

58. Heying, B., et al., *Control of GaN surface morphologies using plasma-assisted molecular beam epitaxy.* Journal of Applied Physics, 2000. 88(4): p. 1855-1860.

59. Shen, X.Q., et al., *Essential Change in Crystal Qualities of GaN Films by Controlling Lattice Polarity in Molecular Beam Epitaxy.* 2000. 39: p. L16-L18.

60. Wagner, R.S. and W.C. Ellis, *Vapor-Liquid-Solid Mechanism of Single Crystal Growth.* Applied Physics Letters, 1964. 4(5): p. 89-90.

61. Gomez, J.L. and Tigli, *Zinc oxide nanostructures: from growth to application.* Journal of Materials Science, 2013. 48: p. 612-624.

62. Ihn, S.-G., et al., *Growth of GaAs Nanowires on Si Substrates Using a Molecular Beam Epitaxy.* IEEE Transactions on Nanotechnology, 2007. 6(3): p. 384-389.

63. Hanrath, T. and B.A. Korgel, *Crystallography and Surface Faceting of Germanium Nanowires.* small, 2005. 1(7): p. 717-721.

64. Wu, Y., et al., *Controlled Growth and Structures of Molecular-Scale Silicon Nanowires.* Nano Letters, 2004. 4(3): p. 433-436.

65. Schwalbach, E.J. and P.W. Voorhees, *Phase Equilibrium and Nucleation in VLS-Grown Nanowires.* Nano Letters, 2008. 8(11): p. 3739-3745.

66. Chen, C.-C., et al., *Catalytic Growth and Characterization of Gallium Nitride Nanowires.* Journal of the American Chemical Society, 2001. 123: p. 2791-2798.

67. Wu, Y. and P. Yang, *Direct Observation of Vapor-Liquid-Solid Nanowire Growth.* Journal of the American Chemical Society, 2001. 123: p. 3165-3166.

68. Johansson, J., et al., *Growth related aspects of epitaxial nanowires.* Nanotechnology, 2006. 17: p. S355-S361.

69. Lu, W. and C.M. Lieber, *Semiconductor nanowires.* Journal of Physics D: Applied Physics, 2006. 39: p. R387-R406.

70. Martensson, T., et al., *Epitaxial III-V Nanowires on Silicon.* Nano Letters, 2004. 4(10): p. 1987-1990.

71. Munshi, A.M., et al., *Crystal phase engeering in self-catalyzed GaAs and GaAs/GaAsSb nanowires grown on Si(111).* Journal of Crystal Growth, 2013. 372: p. 163-169.

72. Lauhon, L.J., et al., *Epitaxial core-shell and core-multishell nanowire heterostructures.* Nature, 2002. 420: p. 57-61.

73. Qian, F., et al., *Gallium Nitride-Based Nanowire Radial Heterostructures for Nanophotonics.* Nano Letters, 2004. 4(10): p. 1975-1979.

74. Qian, F., et al., *Core/Multishell Nanowire Heterostructures as Multicolor, High-Efficiency Light-Emitting Diodes.* Nano Letters, 2005. 5(11): p. 2287-2291.

75. Oh, E., et al., *Platinum-Assisted Vapor-Liquid-Solid Growth of GaN Nanowires and Their Properties.* Journal of the Korean Physical Sociey, 2010. 56(1): p. 100-103.

76. Kuykendall, T., et al., *Crystallographic alignment of high-density gallium nitride nanowire arrays.* Nature Materials, 2004. 3: p. 524-528.

77. Kuykendall, T., et al., *Metalorganic Chemical Vapor Deposition Route to GaN Nanowires with Triangular Cross Sections.* 2003. 3(8): p. 1063-1066.

Appendix Furnace Designs and Miscellaneous

A.1 Introduction

In this chapter, the production and assembly details of the furnace designs will be delineated. Section A.2 relays a couple of housekeeping notes. Sections A.3 though A.5 contain assembly instructions, engineering part drawings, and assembly drawings for each of the three furnace designs. The chapter ends with details about the graphite target holder in section A.6.

A.2 Housekeeping Notes

All parts used to construct the three furnace models are shown in the subsequent sections and are identified by a part number on their corresponding engineering part and assembly drawings. Parts that were purchased and not modified were modeled in AutoCAD™ Inventor 2012 for assembly purposes, but they were not included in the engineering part drawing sections; however, these parts are shown in the assembly drawings, along with their manufacturer name and stock number. The manufacturer and stock number labels of parts that were procured through the McMaster University Engineering & Science Machine Shop are both indicated as “n/a”. Finally, it is worth noting that some parts were reused between iterations of furnace designs. The engineering drawings of these parts are not repeated in subsequent drawing sections. Only new or modified parts are listed.

A.3 "Mark 1" Furnace Design

A.3.1 Assembly Instructions

The following steps describe the process of assembling the "Mark 1" furnace:

Weight-bearing Subassembly (A1)

(1) Three 3/32-inch diameter stainless steel rods (Part Number 15) are press fitted into the corresponding holes on a copper rod (Part Number 14) so that approximately 19.7 mm of the stainless steel rods extend out on one side.

(2) Repeat Step (1) for the remaining 3/32-inch stainless steel rods and copper rod. Ensure that the stainless steel rods are press fitted in the opposite direction to those in Step (1).

(3) Align the lateral holes of three CH-84 ceramic blocks (Part Number 16) with the longer protruding portion of the stainless steel rods and insert them. Tighten the perpendicular screws on the CH-84 ceramic blocks using the appropriately sized screwdriver to secure the stainless steel rods.

(4) Repeat Step (3) for the other press fitted stainless steel rods.

Support Plate Subassembly (A2)

(5) Using the top alumina plate (Part Number 1), partially insert four eighth-inch alumina rods (Part Number 4) into the four holes corresponding to their diameter.

(6) Slide two alumina spacers (Part Number 3) onto the alumina rods in a parallel fashion so that they rest against the underside of the top alumina plate.

(7) Align and slide the axial molybdenum shield (Part Number 6) onto the alumina rods so that it touches the underside of the two alumina spacers from Step (6).

(8) Slide two alumina spacers onto the alumina rods in a parallel fashion so that they rest against the underside of the axial molybdenum shield.

(9) Align the bottom alumina plate (Part Number 2) with the holes it shares with the top alumina plate and press it against the underside of the two alumina spacers from Step (8).

(10) Orient the support plate subassembly so that it is horizontal and the protruding alumina rods extend vertically upwards.

(11) Place the alumina sample holder (Part Number 5) on top of the four alumina rods so that its aperture aligns with the 5/8-inch hole through the top alumina plate.

Furnace Assembly

(12) Slide a copper rod connector (Part Number 13) part way up the shorter quarter-inch diameter copper rod segment of the weight-bearing subassembly.

(13) Repeat Step (12) for other copper rod in the weight-bearing subassembly.

(14) Gently, slide the quarter-inch holes of the support plate subassembly onto the shorter quarter-inch copper rod segments of weight-bearing subassembly.

(15) Securely fasten a stainless steel connector (Part Number 17) onto one of the copper rods underneath the support plate subassembly with a 6-32 stainless steel (Part Number 18) screw using the appropriate screwdriver.

(16) Repeat Step (15) for the other side of the weight-bearing subassembly.

(17) Carefully, place the alumina crucible (Part Number 7) about the sample holder on the centre of the support plate subassembly.

(18) Place the tungsten heating coil (Part Number 8) on top of the alumina crucible on the centre of the support plate subassembly. Ensure the leads of the filament are positioned perpendicular to the cutoff sections of the alumina plates.

(19) Place the alumina radial shield (Part Number 9) about the alumina crucible on the centre of the support plate subassembly. Ensure that the shield is oriented so that the leads of the filament pass through the shield's bottom openings.

(20) Place the molybdenum radial shield (Part Number 10) about the alumina crucible on the centre of the support plate subassembly. Ensure that the shield is oriented so that the leads of the filament pass through the shield's openings.

(21) Attach a filament copper connector (Part Number 11) to one of the ends of the tungsten filament by sliding the filament lead into one the non-threaded holes and then securely tighten the adjacent 2-56 stainless steel screw (Part Number 12) using the appropriate screw driver. Ensure that the filament connector end without a screw in it is oriented in the direction towards the closer copper rod connector.

(22) Repeat Step (21) for the other filament end.

(23) Insert a 2.5-inch long stranded 26 AWG (American wire gauge) copper wire into the non-threaded vacant hole of a copper rod connector (Part Number 13).

(24) Insert a 2-56 stainless steel screw (Part Number 12) into the threaded hole of copper rod connector. Tighten the screw using the appropriate screwdriver to ensure a good electrical connection.

(25) Insert the other end of the stranded copper wire from Step (23) into the non-threaded hole of the closer filament copper connector and create a secure electrical connection by tightening the adjacent 2-56 stainless steel screw (Part Number 12) using the appropriate screw driver.

(26) Repeat Steps (23)-(25) for the remaining stranded copper wire and filament copper connector.

A.3.2 Engineering Part Drawings

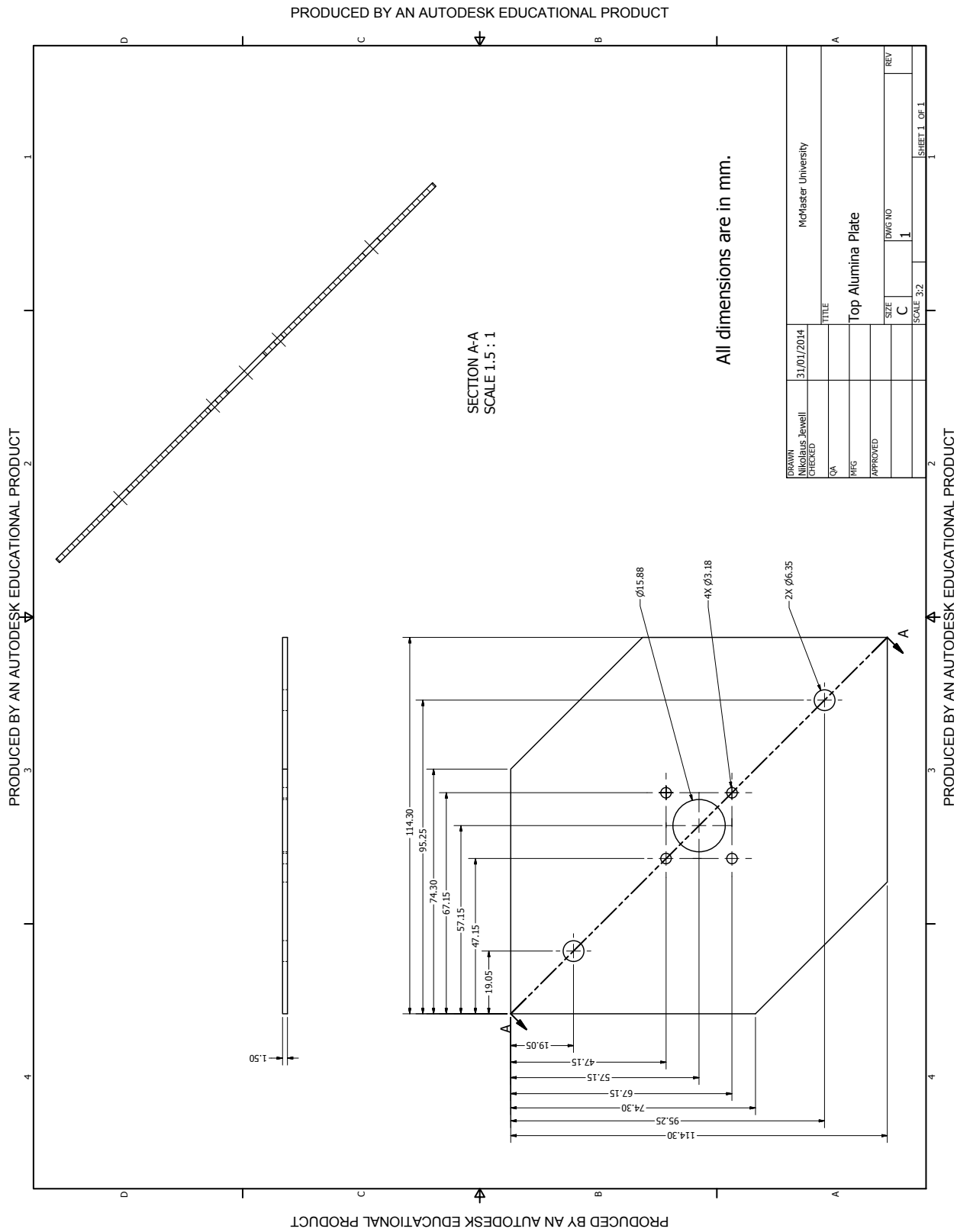

Drawing 1: Mark 1, Top Alumina Plate.

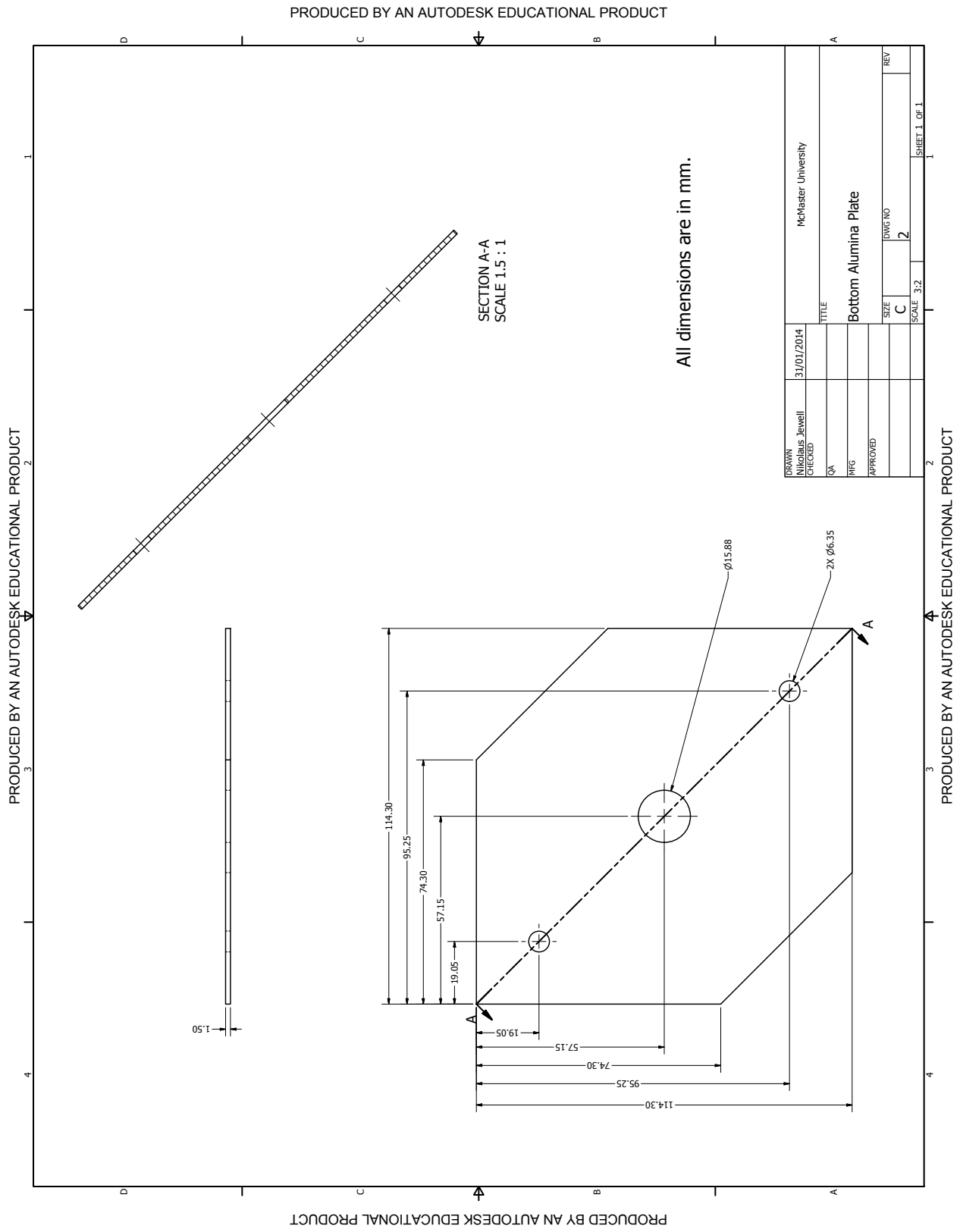

Drawing 2: Mark 1, Bottom Alumina Plate.

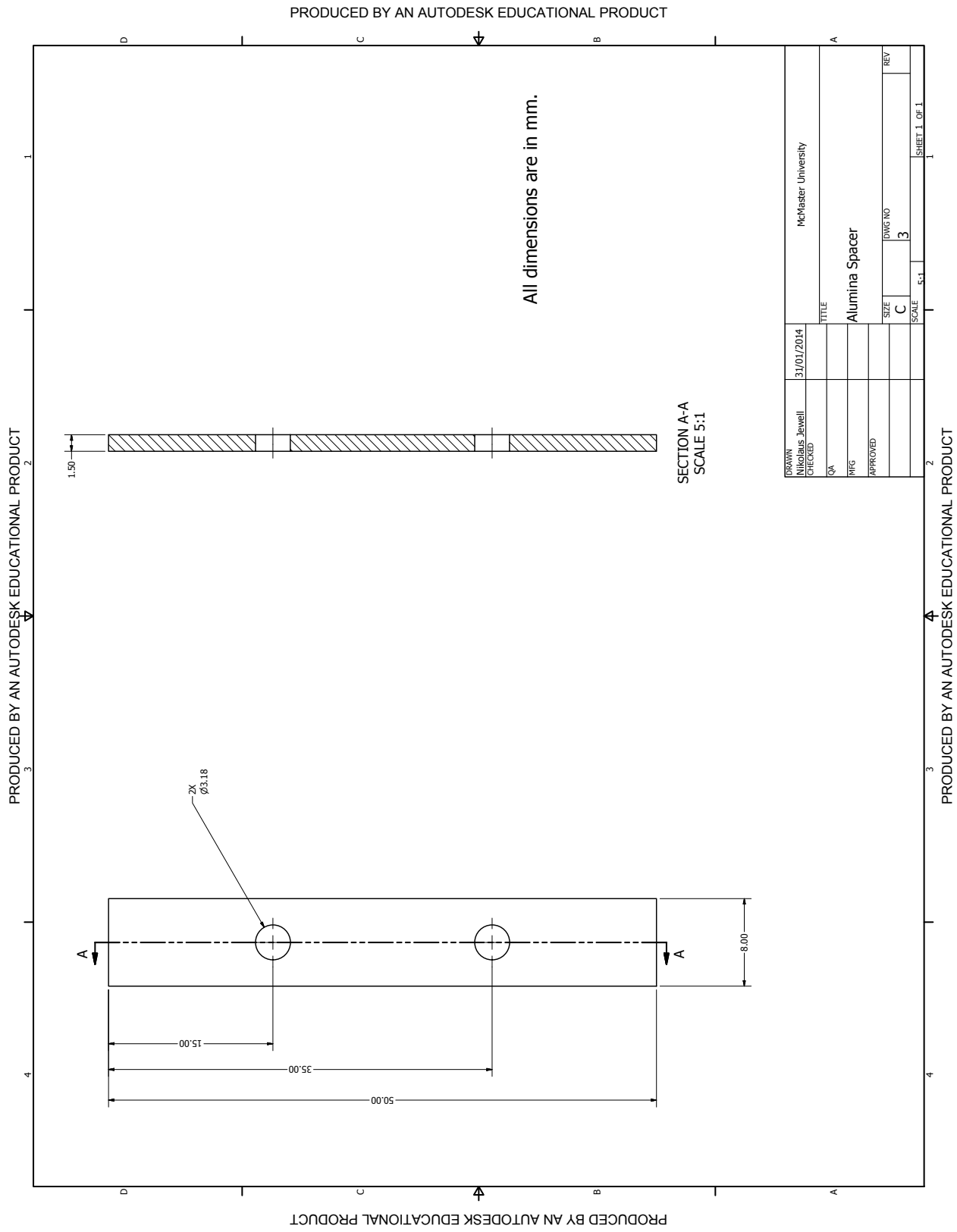

Drawing 3: Mark 1, Alumina Spacer.

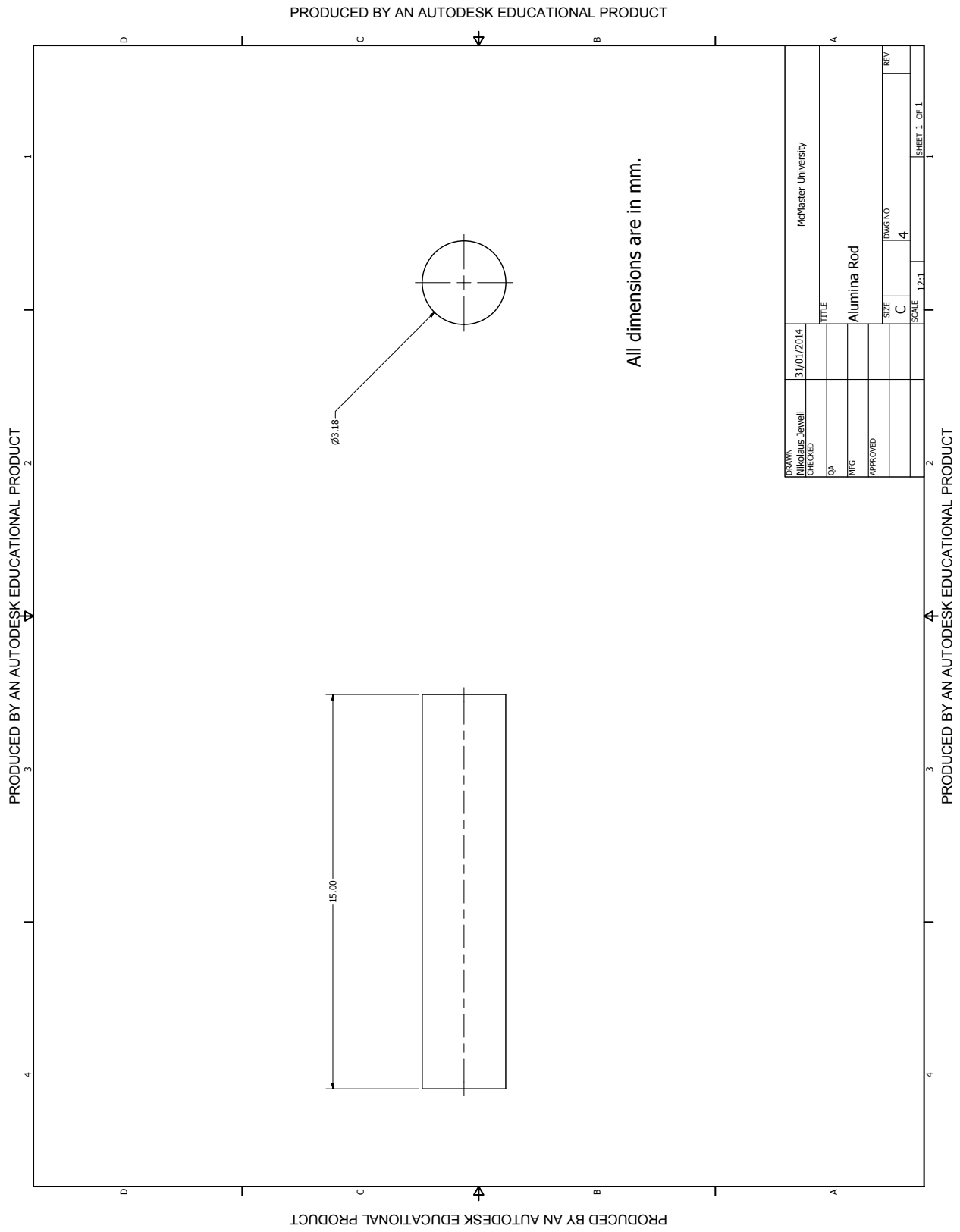

Drawing 4: Mark 1, Alumina Rod.

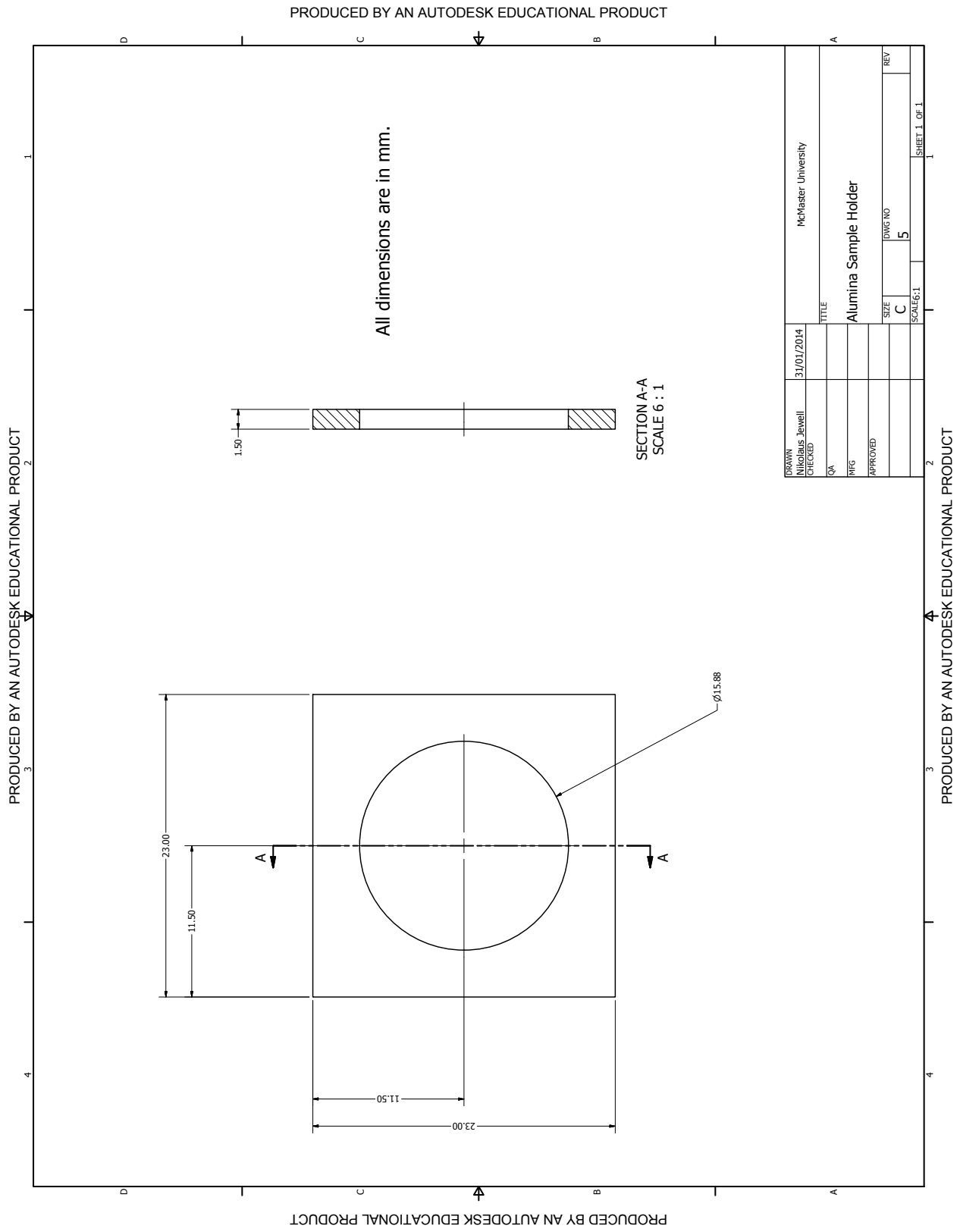

Drawing 5: Mark 1, Alumina Sample Holder.

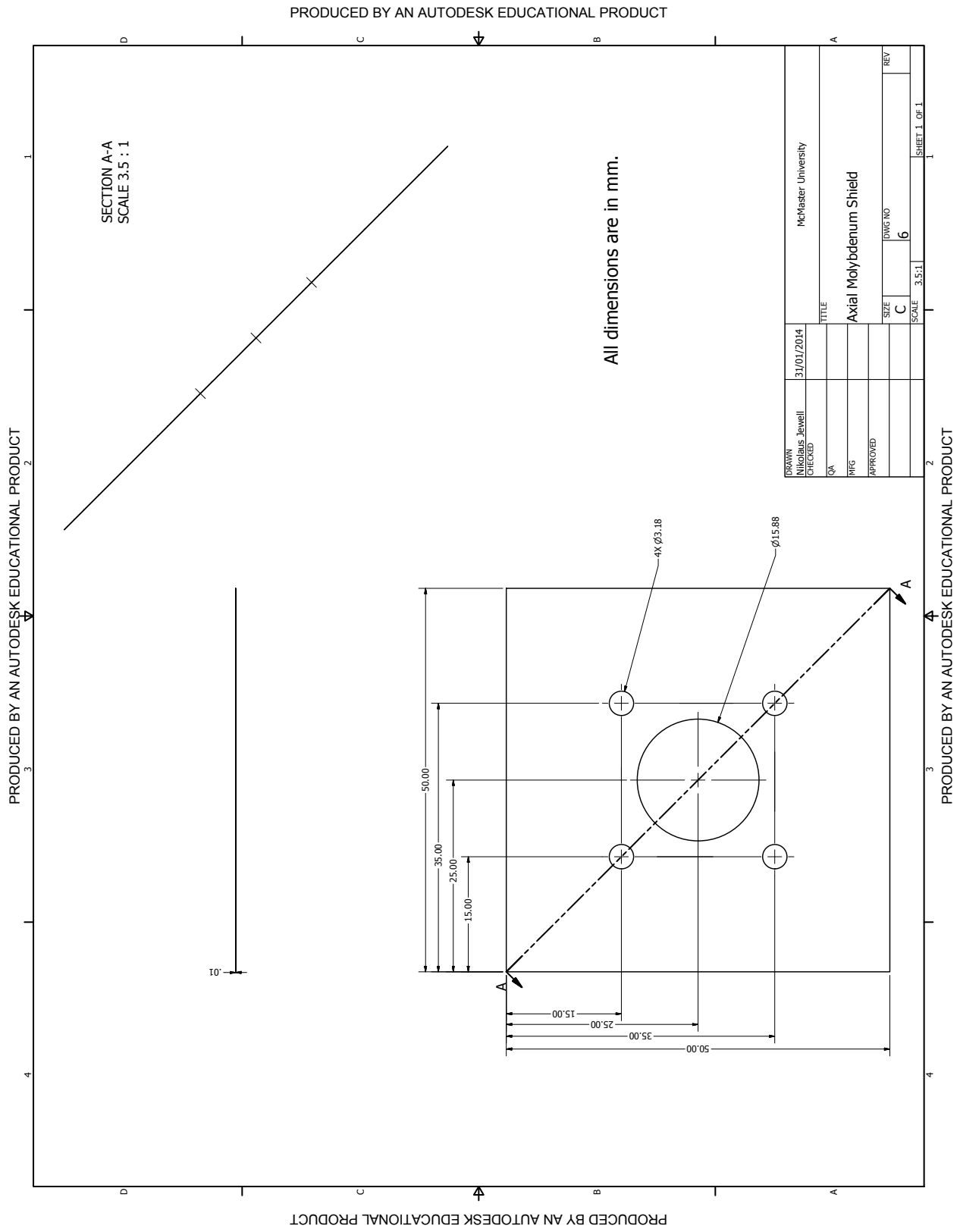

Drawing 6: Mark 1, Axial Molybdenum Shield.

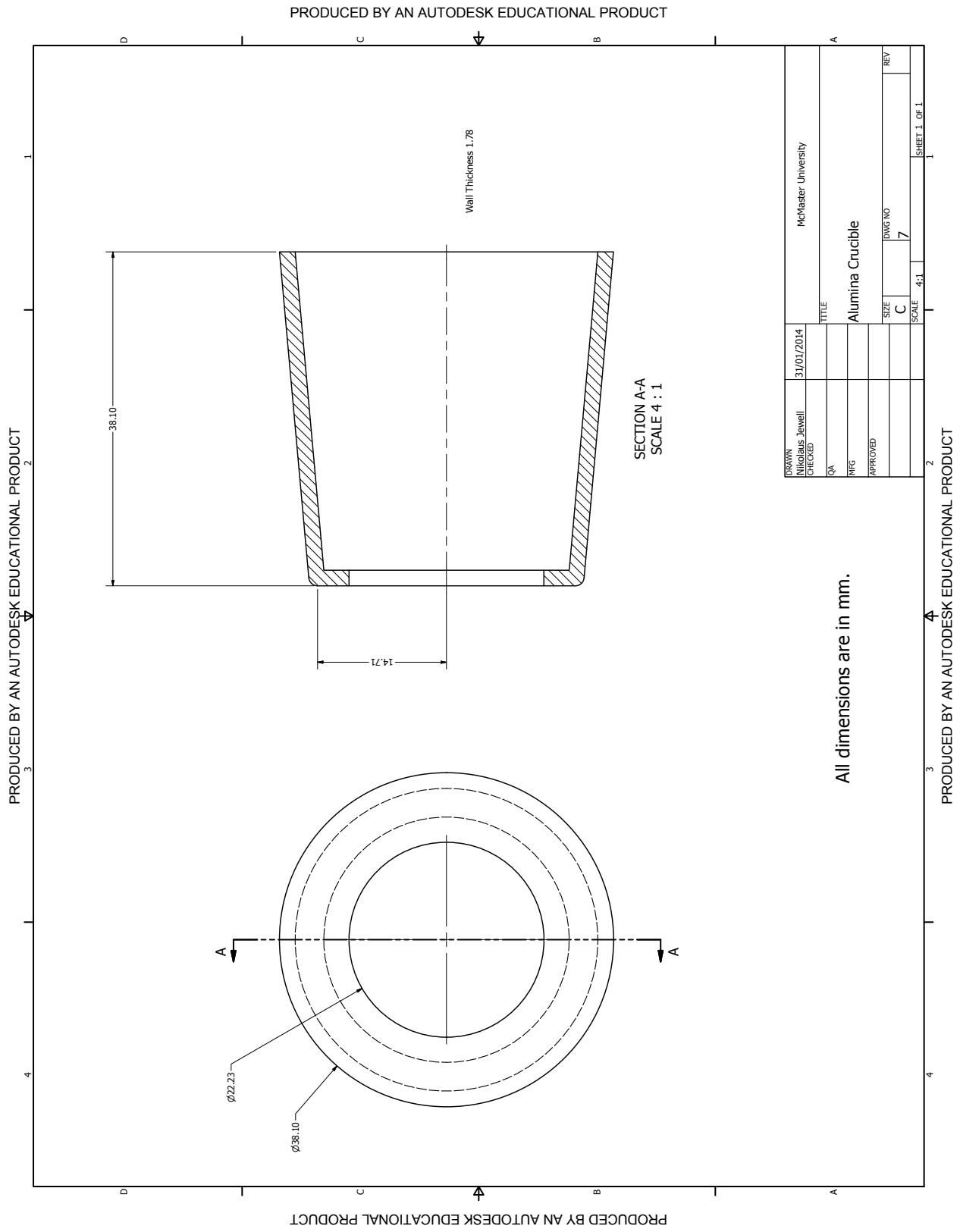

Drawing 7: Mark 1, Alumina Crucible.

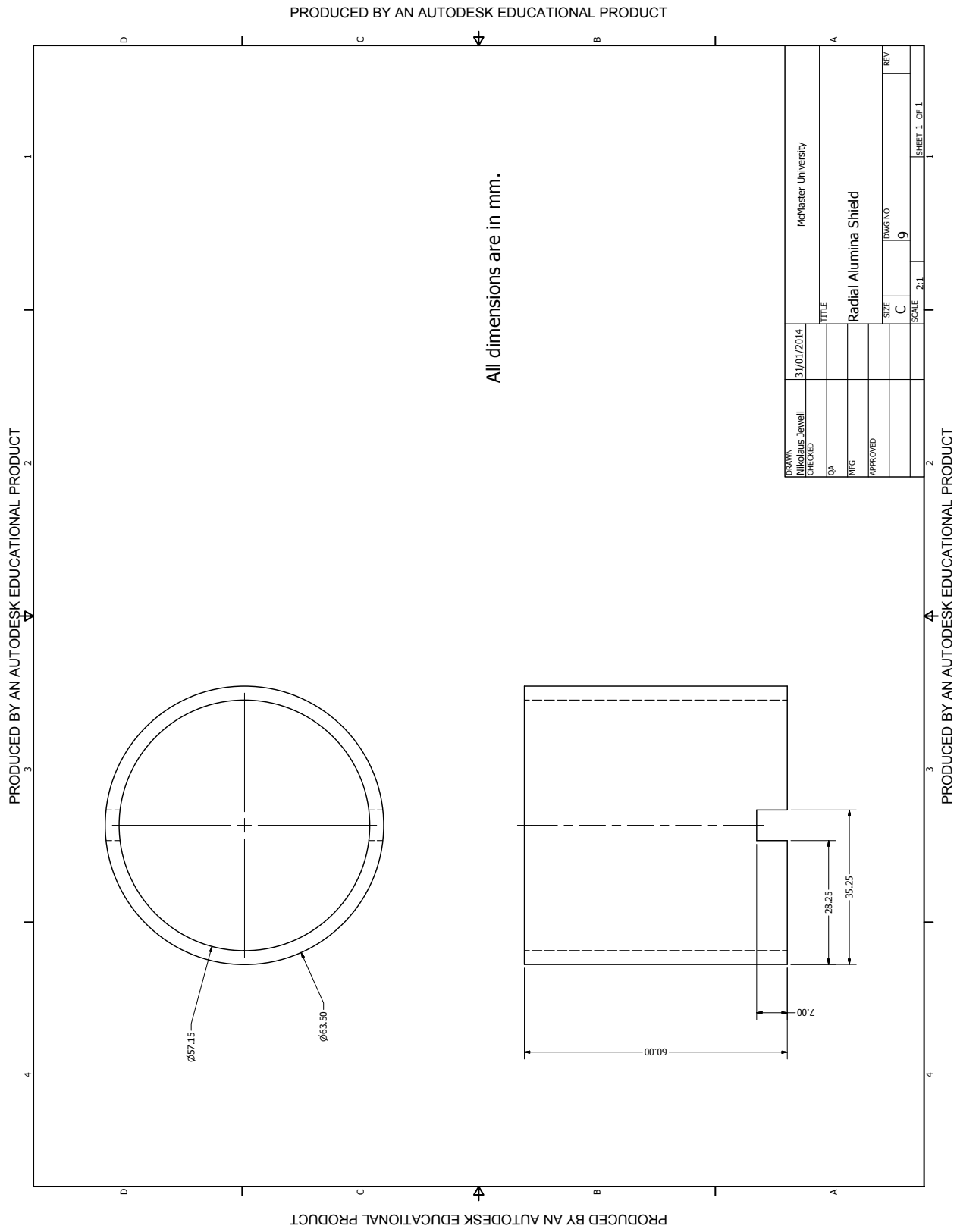

Drawing 8: Mark 1, Radial Alumina Shield.

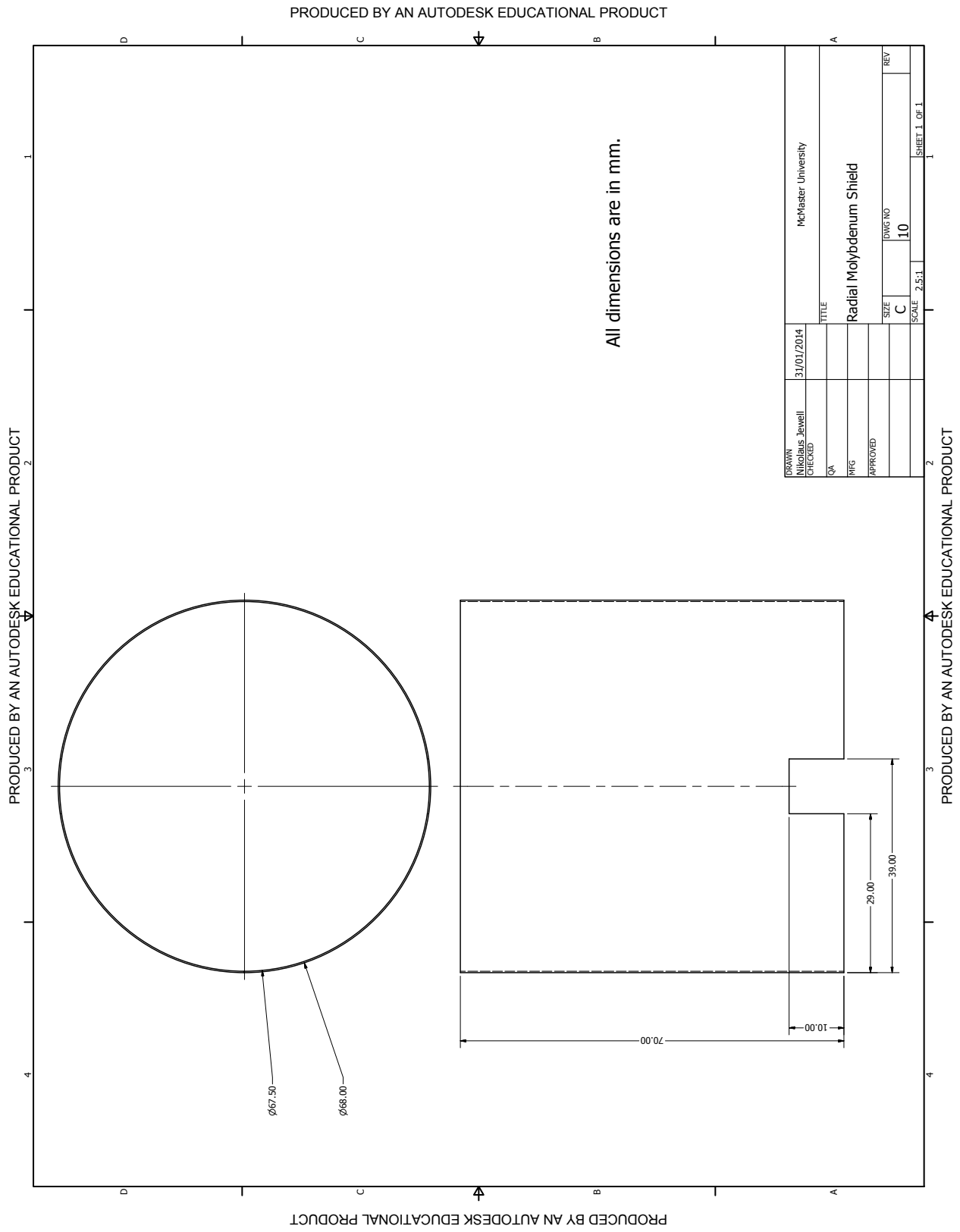

Drawing 9: Mark 1, Radial Molybdenum Shield.

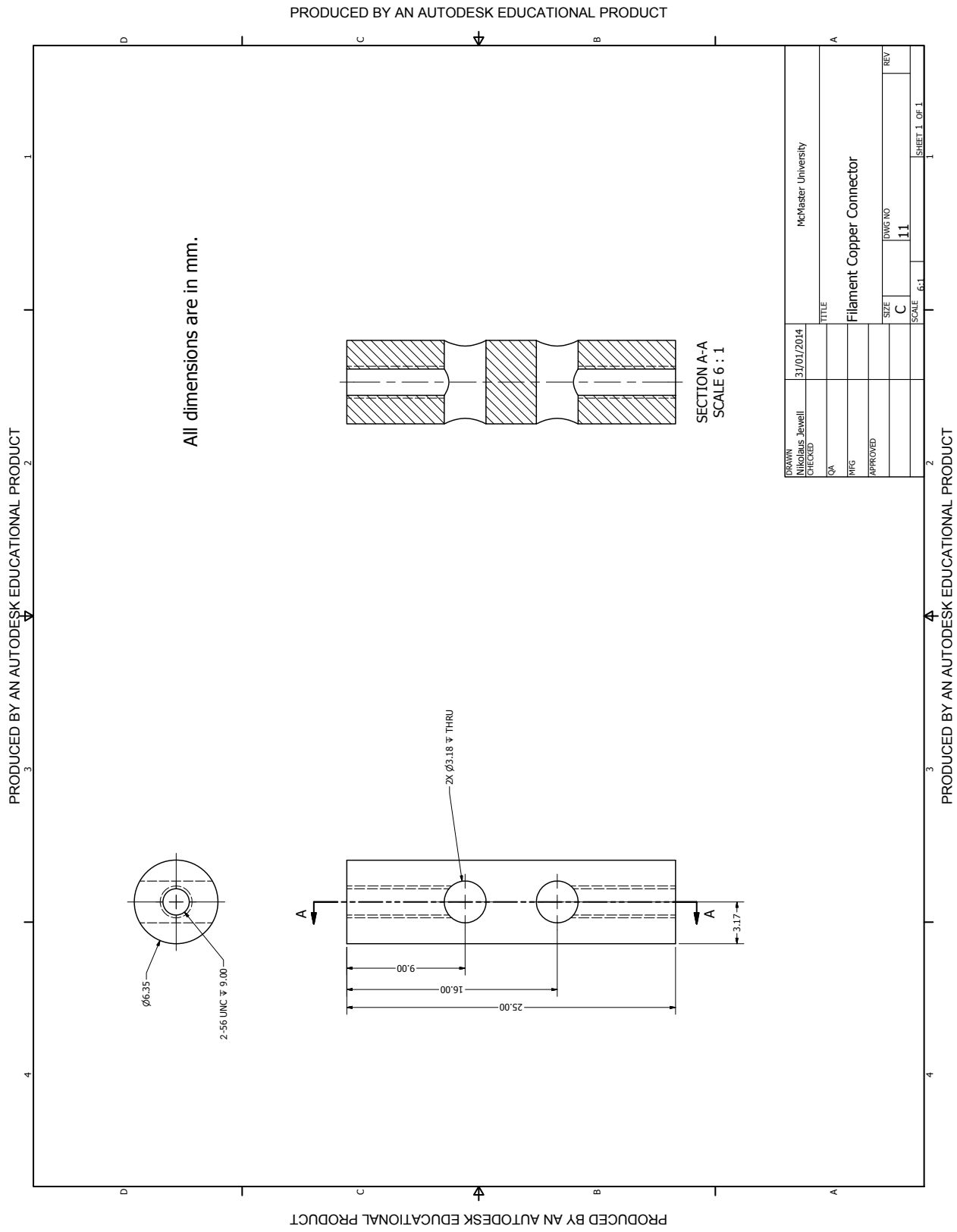

Drawing 10: Mark 1, Filament Copper Connector.

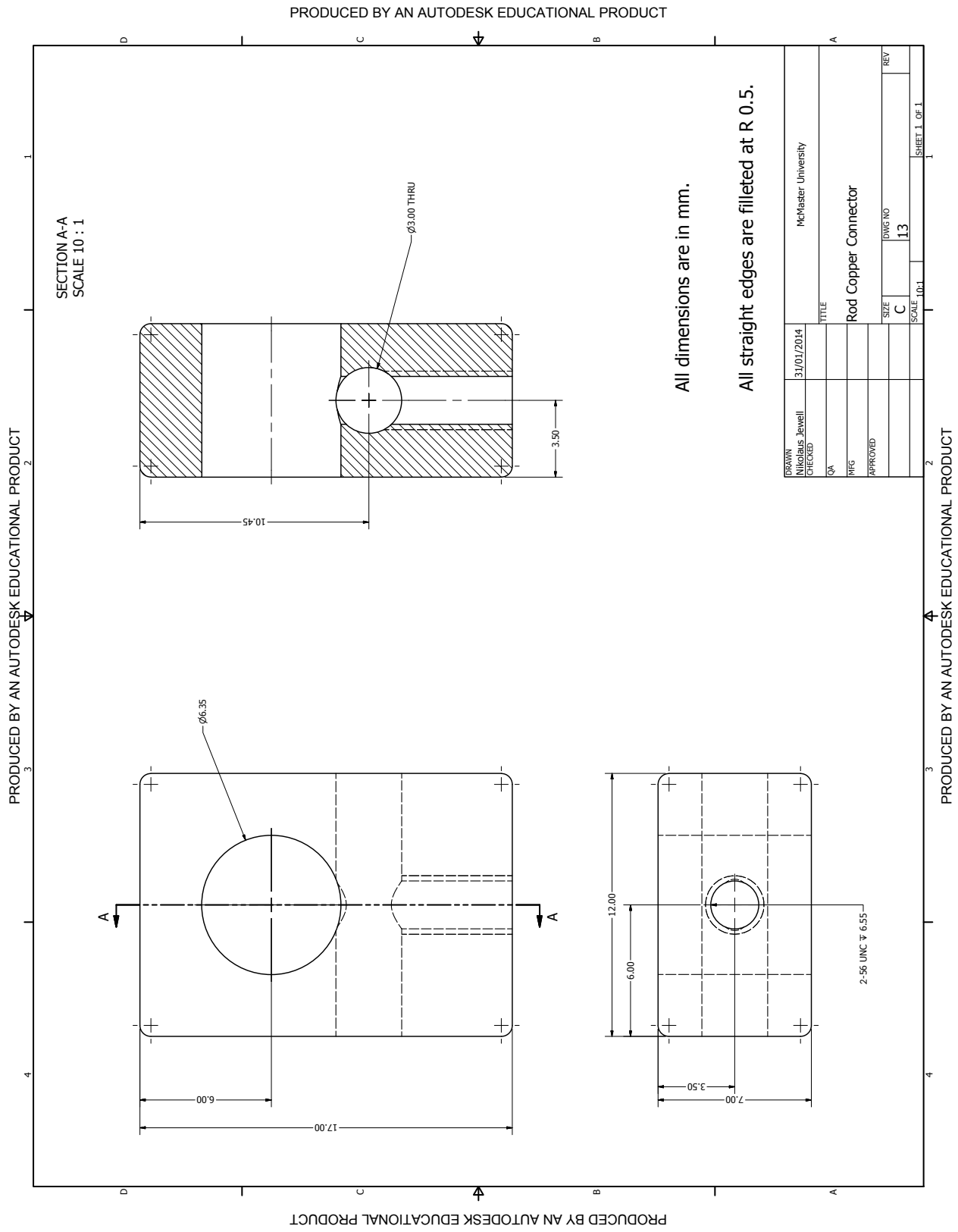

Drawing 11: Mark 1, Filament Copper Connector.

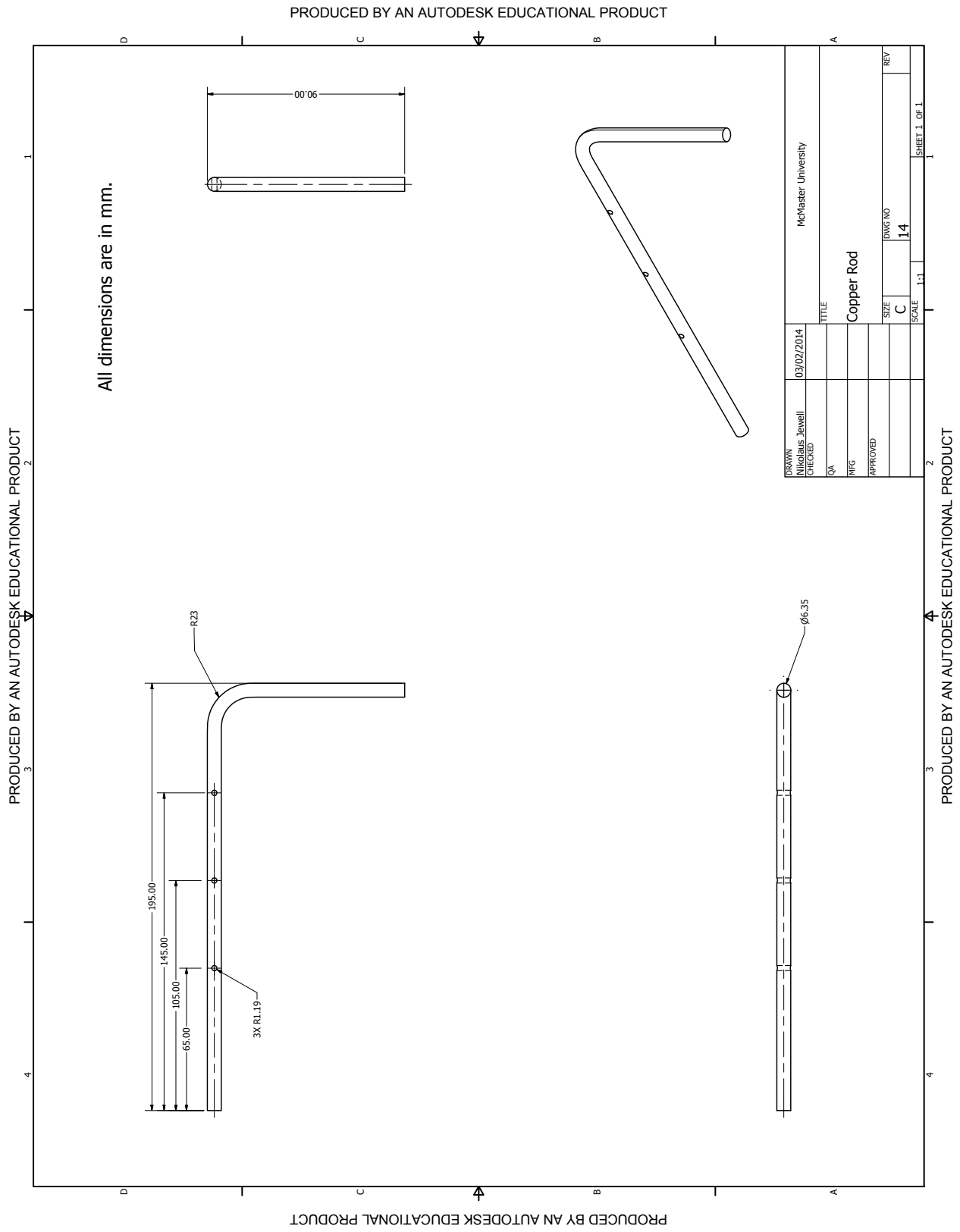

Drawing 12: Mark 1, Copper Rod.

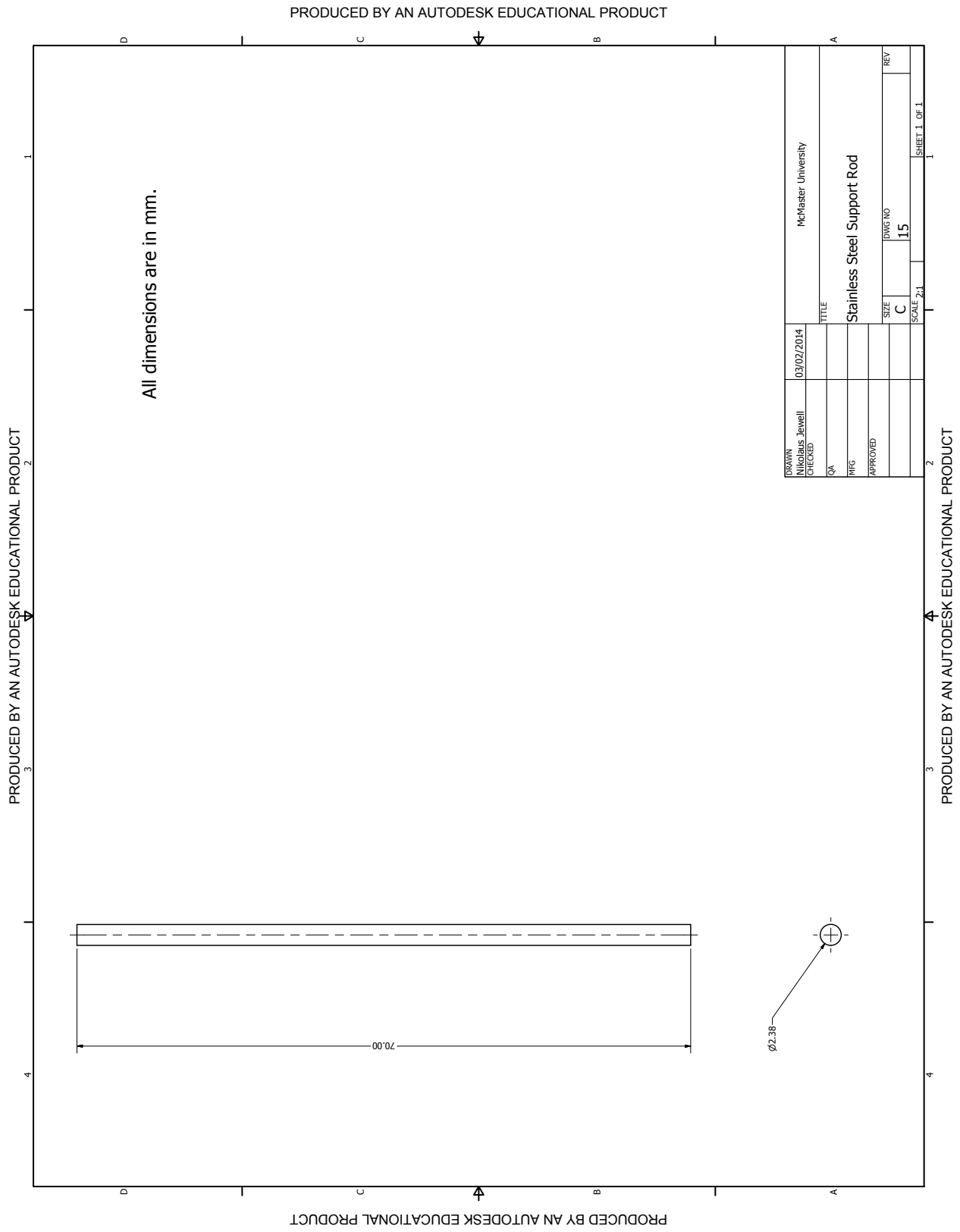

Drawing 13: Mark 1, Stainless Steel Support Rod.

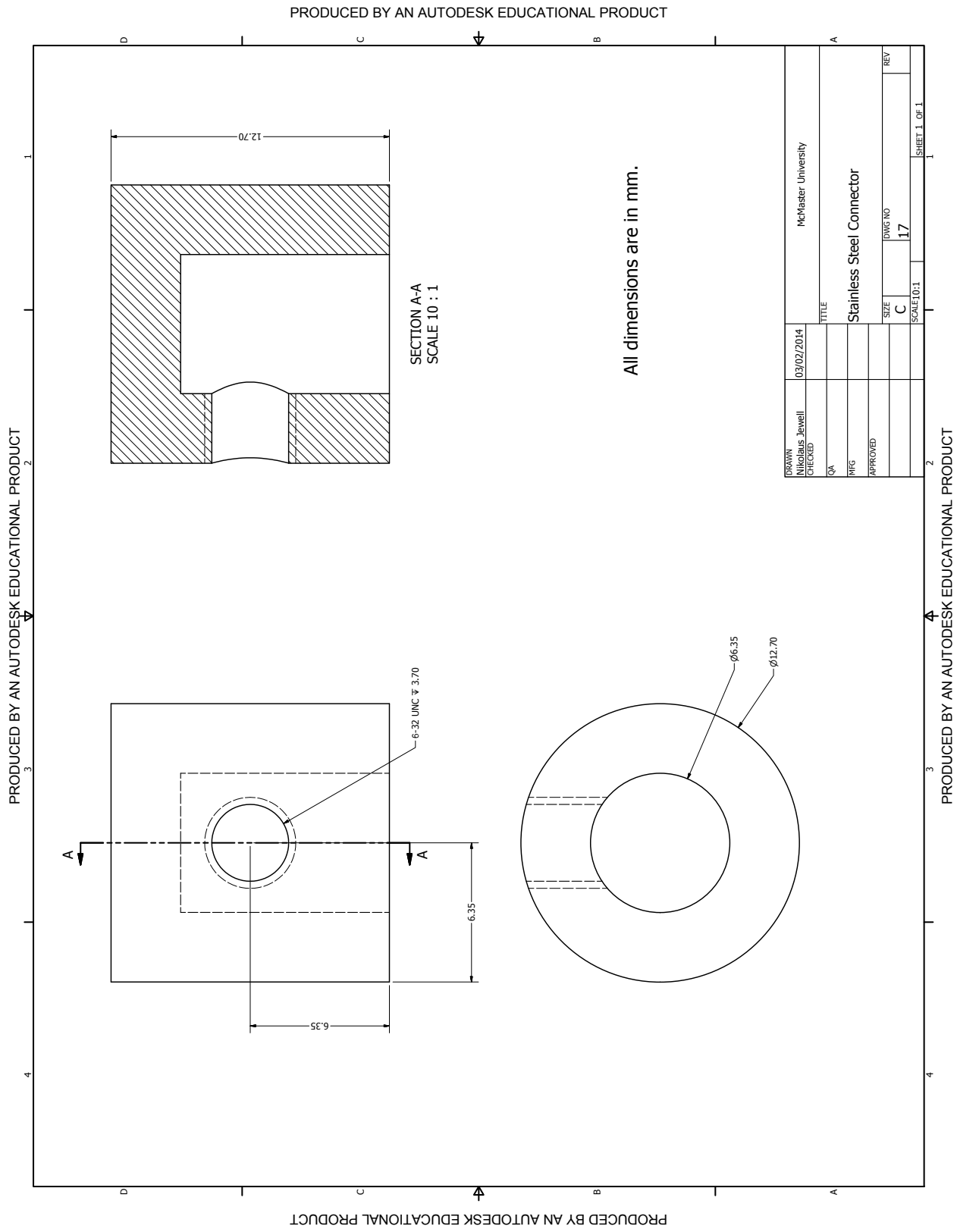

Drawing 14: Mark 1, Stainless Steel Connector.

A.3.3 Assembly Drawings

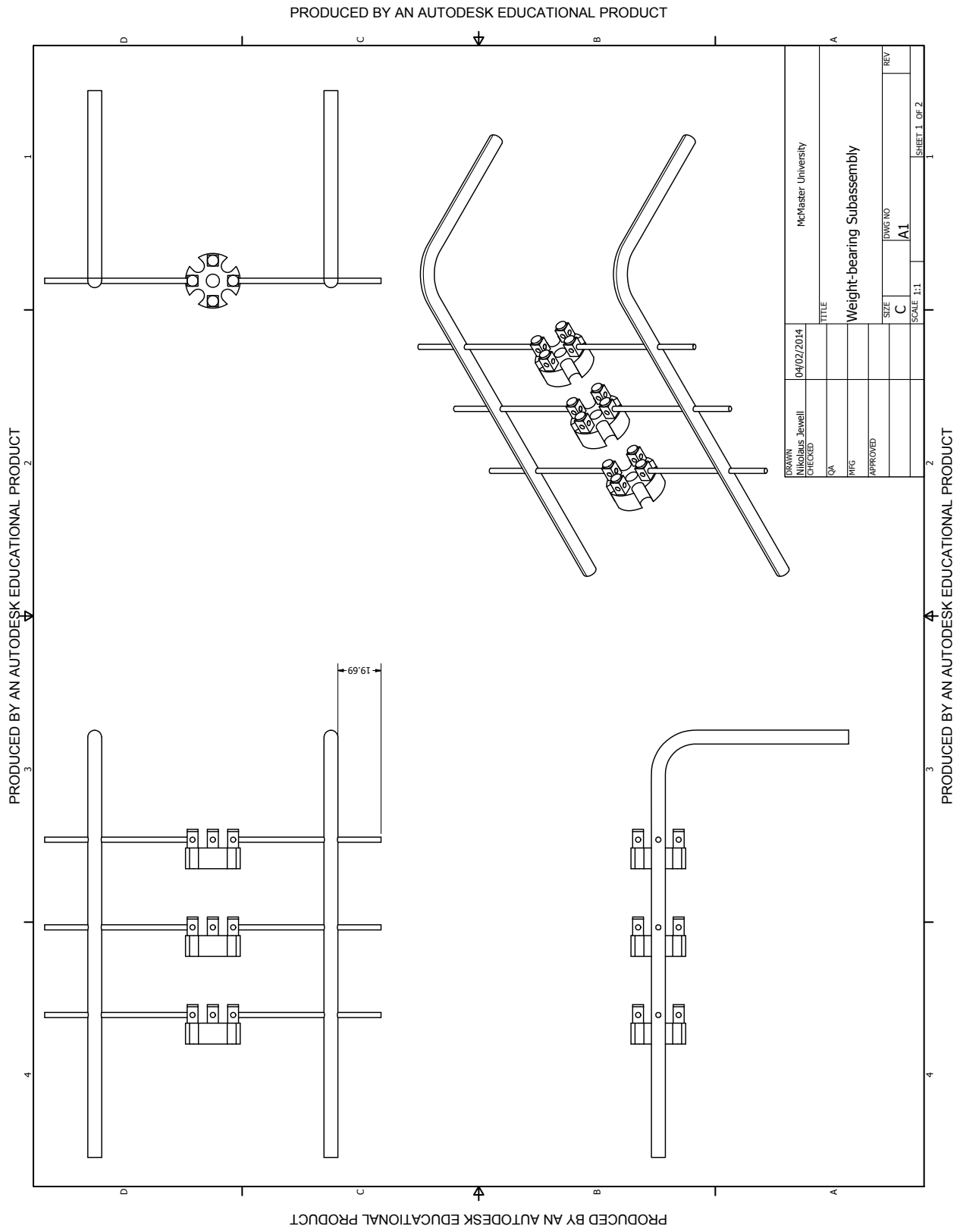

Drawing 15: Mark 1, Weight-bearing Subassembly (A1).

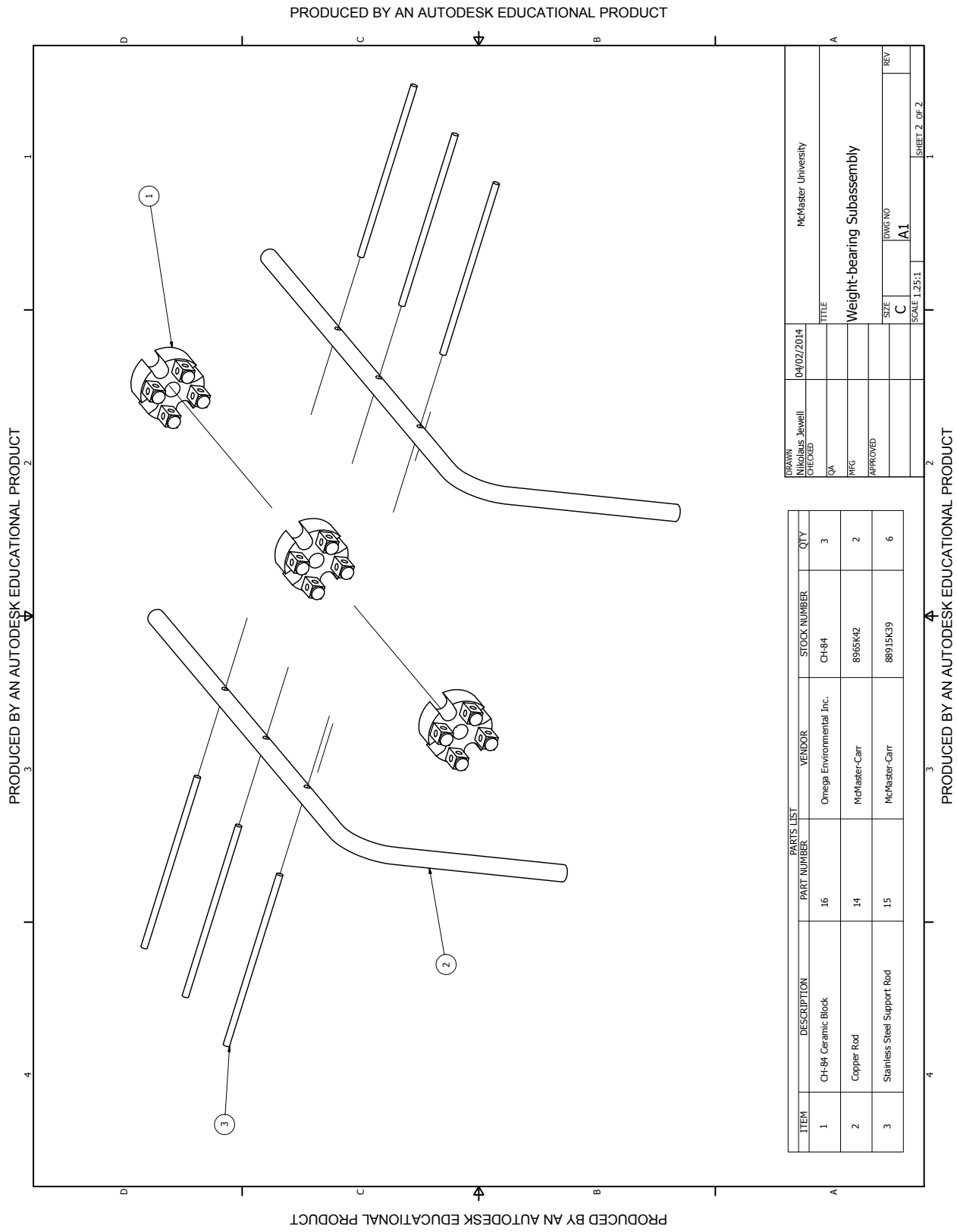
PRODUCED BY AN AUTODESK EDUCATIONAL PRODUCT
PRODUCED BY AN AUTODESK EDUCATIONAL PRODUCT
PRODUCED BY AN AUTODESK EDUCATIONAL PRODUCT
PRODUCED BY AN AUTODESK EDUCATIONAL PRODUCT
PARTS LIST
ITEM | DESCRIPTION | PART NUMBER | VENDOR | STOCK NUMBER | QTY
1 | CH-84 Ceramic Block | 16 | Omega Environmental Inc. | CH-84 | 3
2 | Copper Rod | 14 | McMaster-Carr | 8965K42 | 2
3 | Stainless Steel Support Rod | 15 | McMaster-Carr | 88915K39 | 6
DRAWN Nikolaus Jewell 04/02/2014
CHECKED
QA
MFG
APPROVED
McMaster University
TITLE
Weight-bearing Subassembly
SIZE C
DWG NO A1
REV
SCALE 1.25:1
SHEET 2 OF 2

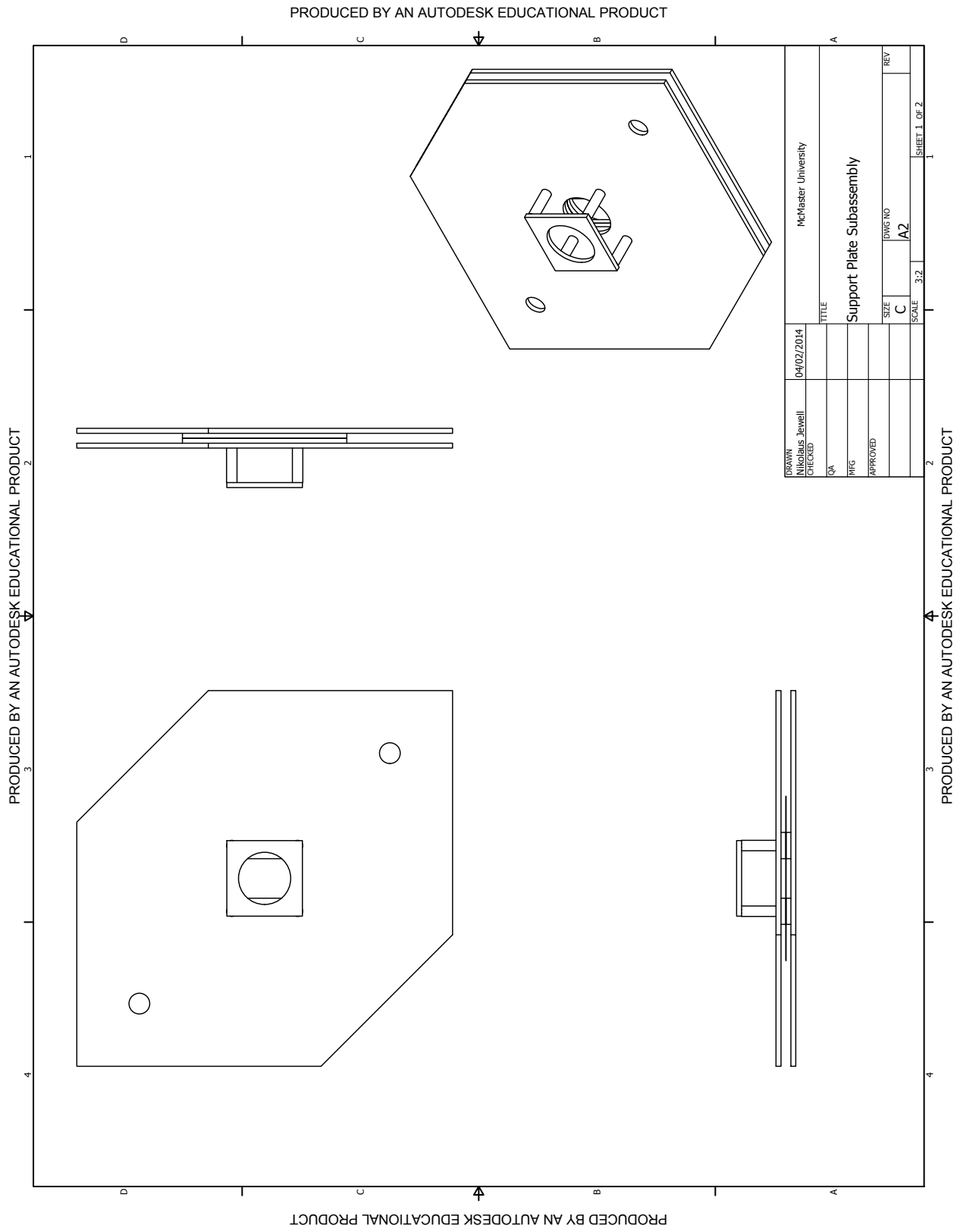

Drawing 16: Mark 1, Support Plate Subassembly (A2).

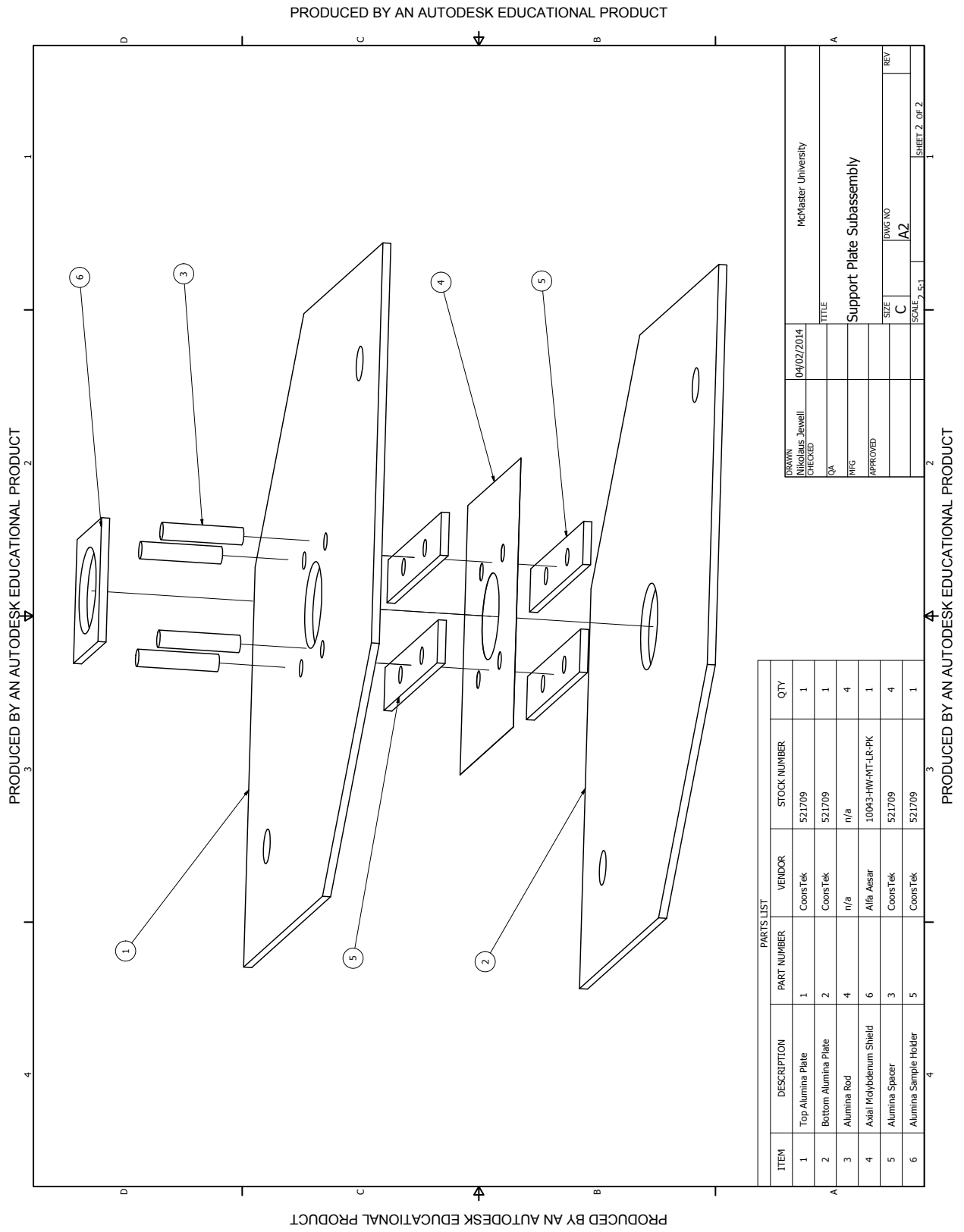
PRODUCED BY AN AUTODESK EDUCATIONAL PRODUCT
PRODUCED BY AN AUTODESK EDUCATIONAL PRODUCT
PRODUCED BY AN AUTODESK EDUCATIONAL PRODUCT
PRODUCED BY AN AUTODESK EDUCATIONAL PRODUCT
PARTS LIST
ITEM DESCRIPTION PART NUMBER VENDOR STOCK NUMBER QTY
1 Top Alumina Plate 1 CoorsTek 521709 1
2 Bottom Alumina Plate 2 CoorsTek 521709 1
3 Alumina Rod 4 n/a n/a 4
4 Axial Molybdenum Shield 6 Alfa Aesar 10043-HW-MT-LR-PK 1
5 Alumina Spacer 3 CoorsTek 521709 4
6 Alumina Sample Holder 5 CoorsTek 521709 1
DRAWN Nikolaus Jewell 04/02/2014
CHECKED
QA
MFG
APPROVED
McMaster University
TITLE
Support Plate Subassembly
SIZE C
DWG NO A2
REV
SCALE 2.5:1
SHEET 2 OF 2

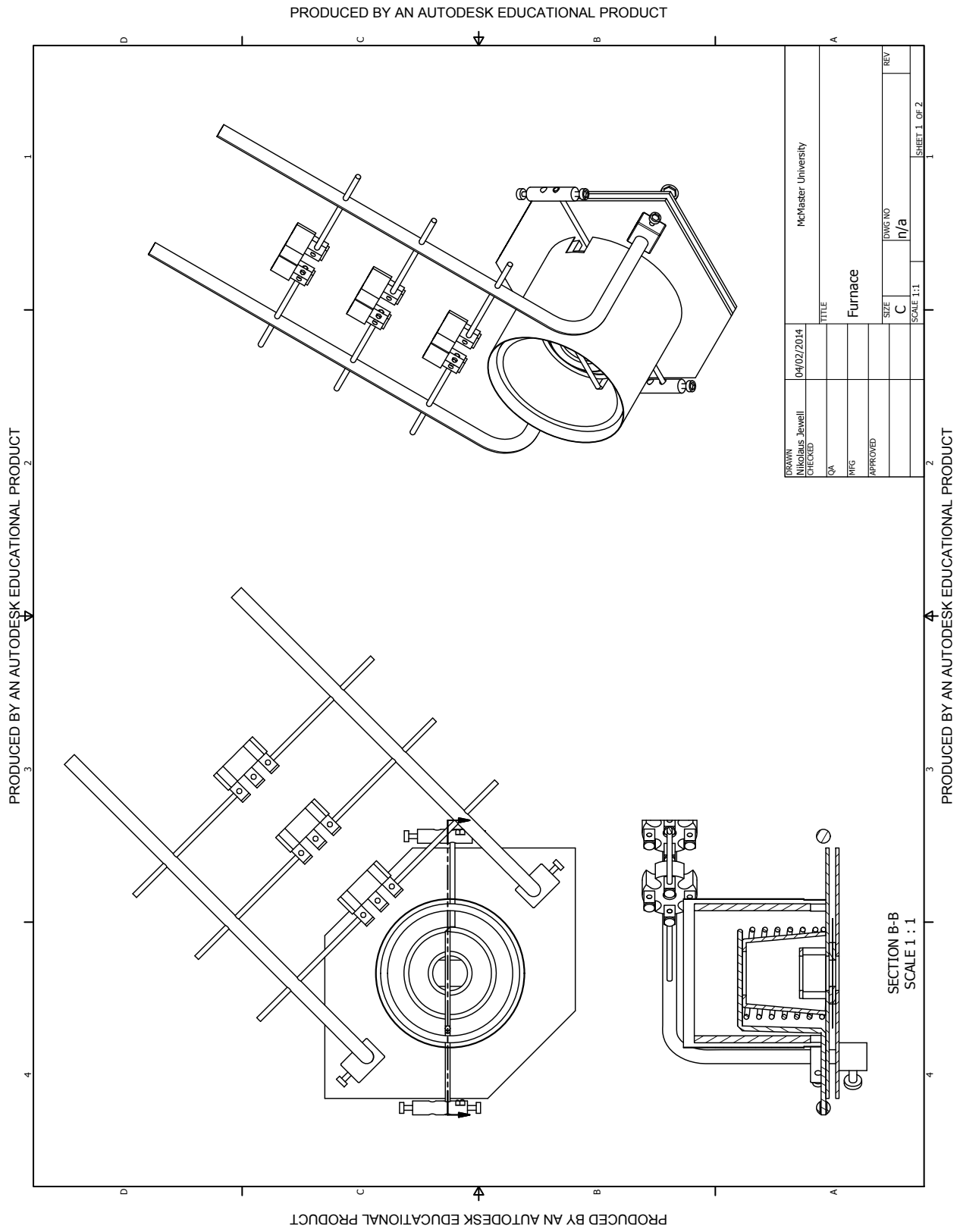

Drawing 17: Mark 1, Furnace Assembly.

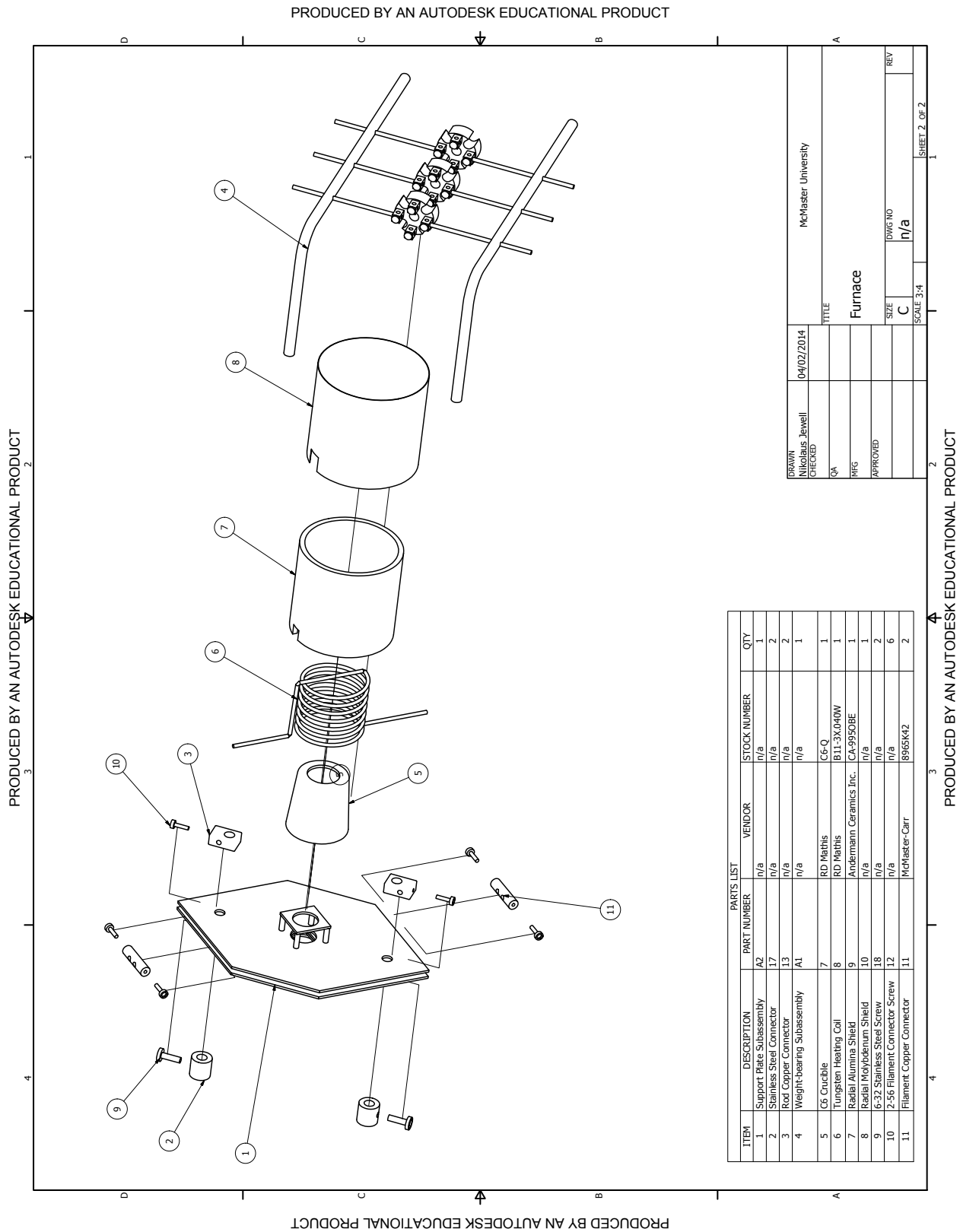
PRODUCED BY AN AUTODESK EDUCATIONAL PRODUCT
PRODUCED BY AN AUTODESK EDUCATIONAL PRODUCT
PRODUCED BY AN AUTODESK EDUCATIONAL PRODUCT
PRODUCED BY AN AUTODESK EDUCATIONAL PRODUCT
PARTS LIST
ITEM | DESCRIPTION | PART NUMBER | VENDOR | STOCK NUMBER | QTY
1 | Support Plate Subassembly | A2 | n/a | n/a | 1
2 | Stainless Steel Connector | 17 | n/a | n/a | 2
3 | Rod Copper Connector | 13 | n/a | n/a | 2
4 | Weight-bearing Subassembly | A1 | n/a | n/a | 1
5 | C6 Crucible | 7 | RD Mathis | C6-Q | 1
6 | Tungsten Heating Coil | 8 | RD Mathis | B11-3X.040W | 1
7 | Radial Alumina Shield | 9 | Andermann Ceramics Inc. | CA-995OBE | 1
8 | Radial Molybdenum Shield | 10 | n/a | n/a | 1
9 | 6-32 Stainless Steel Screw | 18 | n/a | n/a | 2
10 | 2-56 Filament Connector Screw | 12 | n/a | n/a | 6
11 | Filament Copper Connector | 11 | McMaster-Carr | 8965K42 | 2
DRAWN Nikolaus Jewell 04/02/2014
CHECKED
QA
MFG
APPROVED
McMaster University
TITLE
Furnace
SIZE C
DWG NO n/a
REV
SCALE 3:4
SHEET 2 OF 2

A.4 "Mark 2" Furnace Design

A.4.1 Assembly Instructions

The following steps describe the process of assembling the "Mark 2" furnace:

Weight-bearing Subassembly (A3)

(1) Three 3/32-inch diameter stainless steel rods (Part Number 15) are press fitted into the corresponding holes on a copper rod (Part Number 14) so that approximately 28.5 mm of the stainless steel rods extend out on one side.

(2) Repeat Step (1) for the remaining 3/32-inch stainless steel rods and copper rod. Ensure that the stainless steel rods are press fitted in the opposite direction to those in Step (1).

(3) Align the lateral holes of three CH-84 ceramic blocks (Part Number 16) with the longer protruding portion of the stainless steel rods and insert them. Tighten the perpendicular screws on the CH-84 ceramic blocks using the appropriately sized screwdriver to secure the stainless steel rods.

(4) Repeat Step (3) for the other press fitted stainless steel rods.

Ledge Subassembly (A4)

(5) Using the top alumina plate (Part Number 22), partially insert four eighth-inch alumina rods (Part Number 4) into the four holes corresponding to their diameter.

(6) Slide two alumina spacers (Part Number 3) onto the alumina rods in a parallel fashion so that they rest against the underside of the top alumina plate.

(7) Align and slide the axial molybdenum shield (Part Number 6) onto the alumina rods so that it touches the underside of the two alumina spacers from Step (6).

(8) Slide two more alumina spacers onto the alumina rods in a parallel fashion so that they rest against the underside of the axial molybdenum shield.

(9) Align and slide another axial molybdenum shield onto the alumina rods so that it touches the underside of the two alumina spacers from Step (8).

(10) Align the bottom alumina plate (Part Number 21) with the holes it shares with the top alumina plate and press it against the underside of the axial molybdenum shield from Step (9).

(11) Orient these parts so that they are horizontal and the protruding alumina rods extend vertically upwards and place the structure on top of the alumina ledge (Part Number 20) so that the centre 5/8-inch diameter holes align with each other.

(12) Place the alumina sample holder (Part Number 5) on top of the four alumina rods so that its aperture aligns with the 5/8-inch hole through the top alumina plate.

Furnace Assembly

(13) Slide a copper rod connector (Part Number 13) part way up the shorter quarter-inch diameter copper rod segment of the weight-bearing subassembly.

(14) Repeat Step (13) for other copper rod in the weight-bearing subassembly.

(15) Gently, slide the quarter-inch holes of the ledge subassembly onto the shorter quarter-inch copper rod segments of weight-bearing subassembly.

(16) Securely fasten a stainless steel connector (Part Number 17) onto one of the copper rods underneath the ledge subassembly with a 6-32 stainless steel (Part Number 18) screw using the appropriate screwdriver. Ensure that the flat head of the screw faces towards the centre of the ledge subassembly.

(17) Repeat Step (16) for the other side of the weight-bearing subassembly.

(18) Carefully, place the alumina crucible (Part Number 7) about the sample holder on the centre of the ledge subassembly.

(19) Place the tungsten heating coil (Part Number 8) on top of the alumina crucible on the centre of the ledge subassembly. Ensure the leads of the filament are positioned at an approximate 45-degree angle to the length of alumina ledge.

(20) Place the alumina radial shield (Part Number 9) about the alumina crucible on the centre of the ledge subassembly. Ensure that the shield is oriented so that the leads of the filament pass through the shield's bottom openings.

(21) Place the molybdenum radial shield (Part Number 10) about the alumina crucible on the centre of the ledge subassembly. Ensure that the shield is oriented so that the leads of the filament pass through the shield's openings.

(22) Attach a filament copper connector (Part Number 11) to one of the ends of the tungsten filament by sliding the filament lead into one the non-threaded holes and then

securely tighten the adjacent 2-56 stainless steel screw (Part Number 12) using the appropriate screw driver. Ensure that the filament connector end without a screw in it is oriented in the direction towards the closer copper rod connector.

(23) Repeat Step (22) for the other filament end.

(24) Insert a 2.5-inch long stranded 26 AWG (American wire gauge) copper wire into the non-threaded vacant hole of a copper rod connector (Part Number 13).

(25) Insert a 2-56 stainless steel screw (Part Number 12) into the threaded hole of copper rod connector. Tighten the screw using the appropriate screwdriver to ensure a good electrical connection.

(26) Insert the other end of the stranded copper wire from Step (24) into the non-threaded hole of the closer filament copper connector and create a secure electrical connection by tightening the adjacent 2-56 stainless steel screw (Part Number 12) using the appropriate screw driver.

(27) Repeat Steps (24)-(26) for the remaining stranded copper wire and filament copper connector.

A.4.2 Engineering Part Drawings

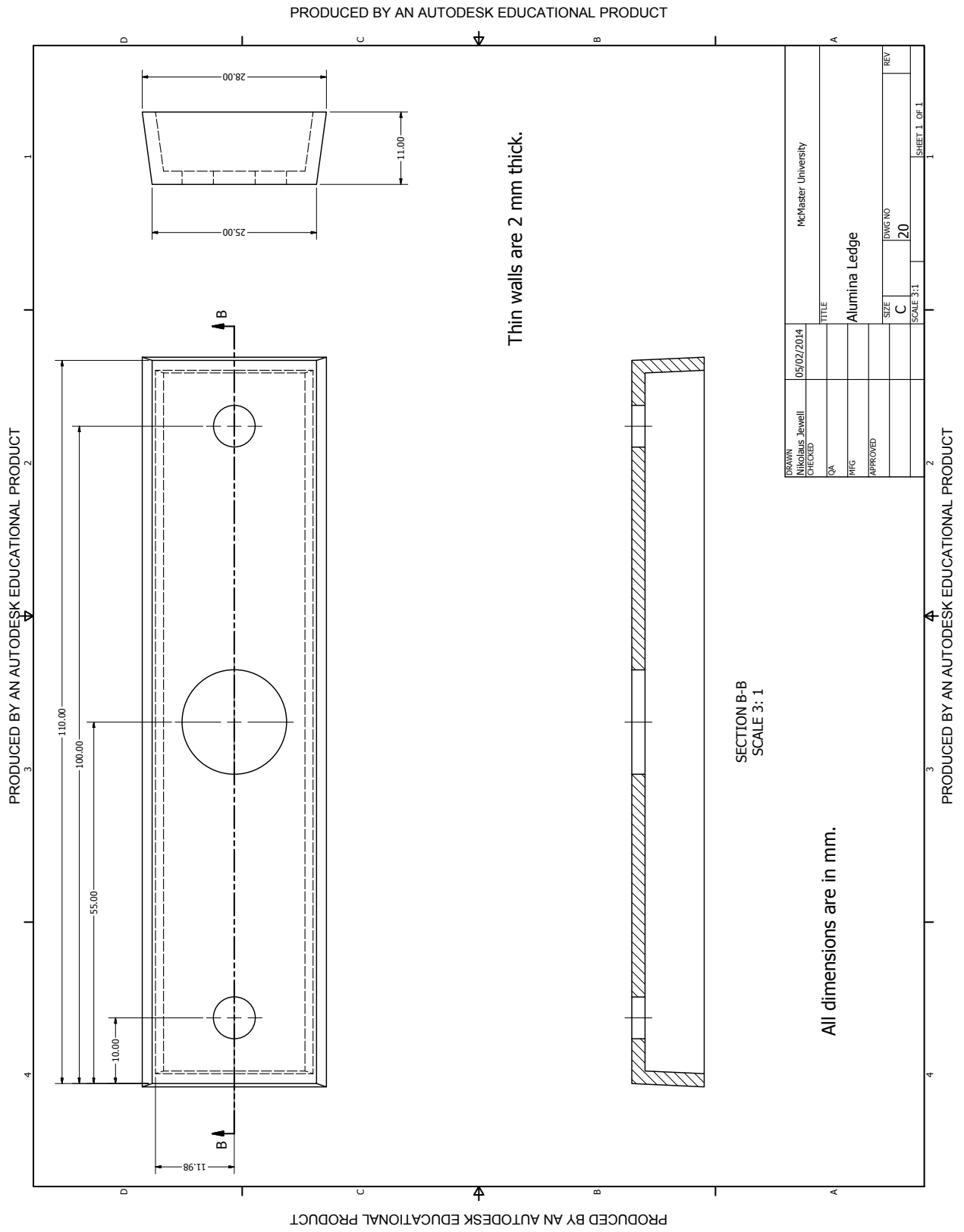

Drawing 18: Mark 2, Alumina Ledge.

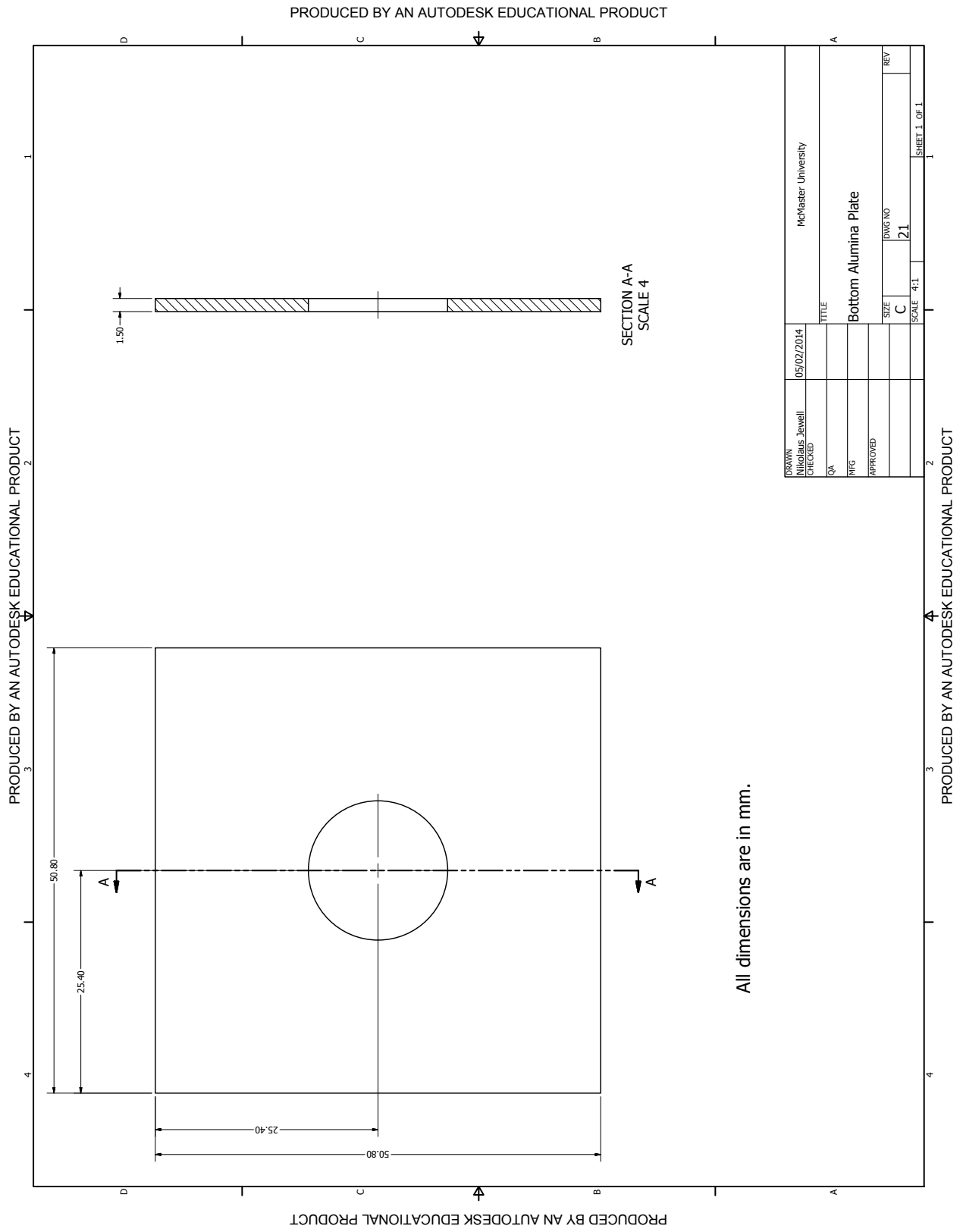

Drawing 19: Mark 2, Bottom Alumina Plate.

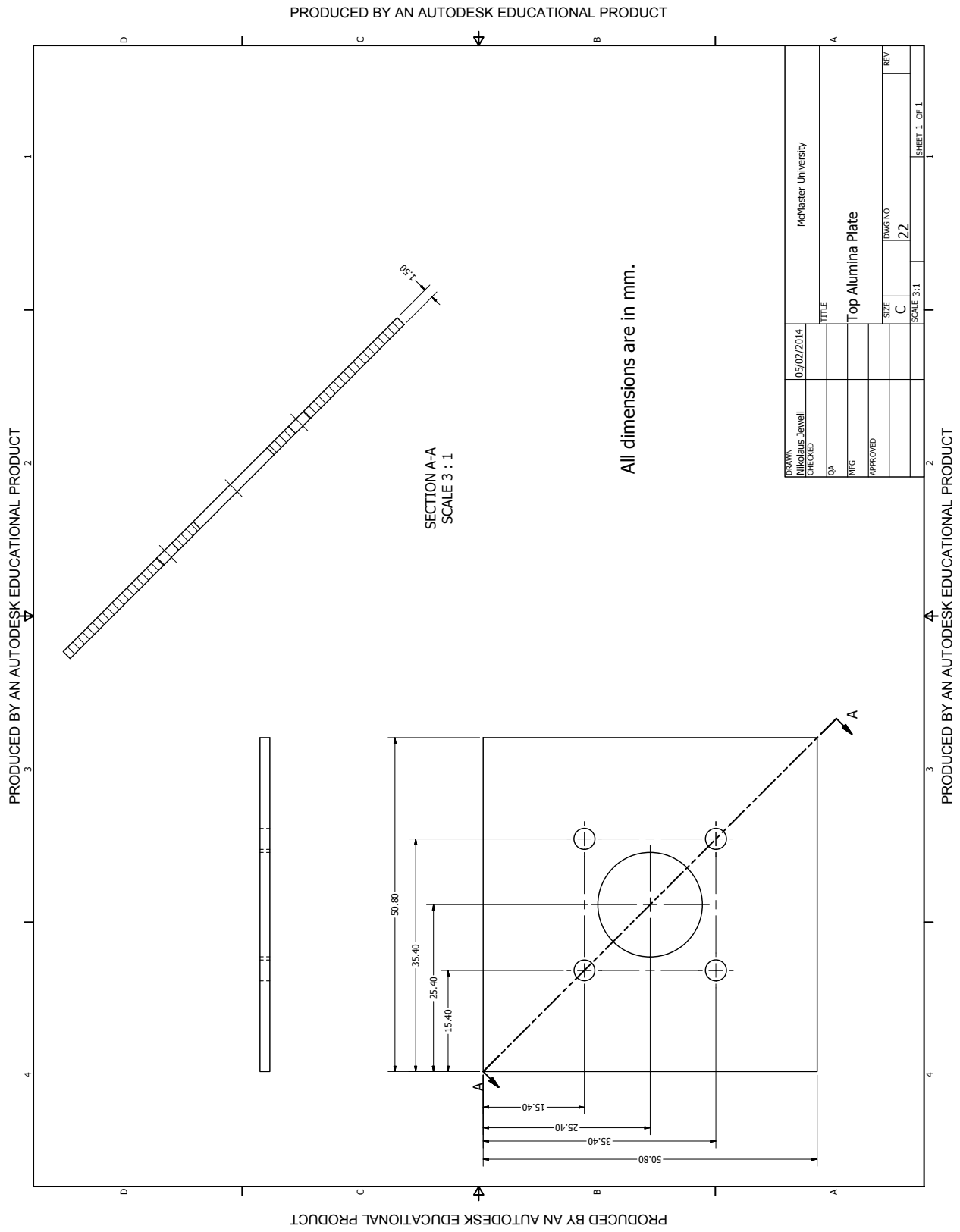

Drawing 20: Mark 2, Top Alumina Plate.

A.4.3 Assembly Drawings

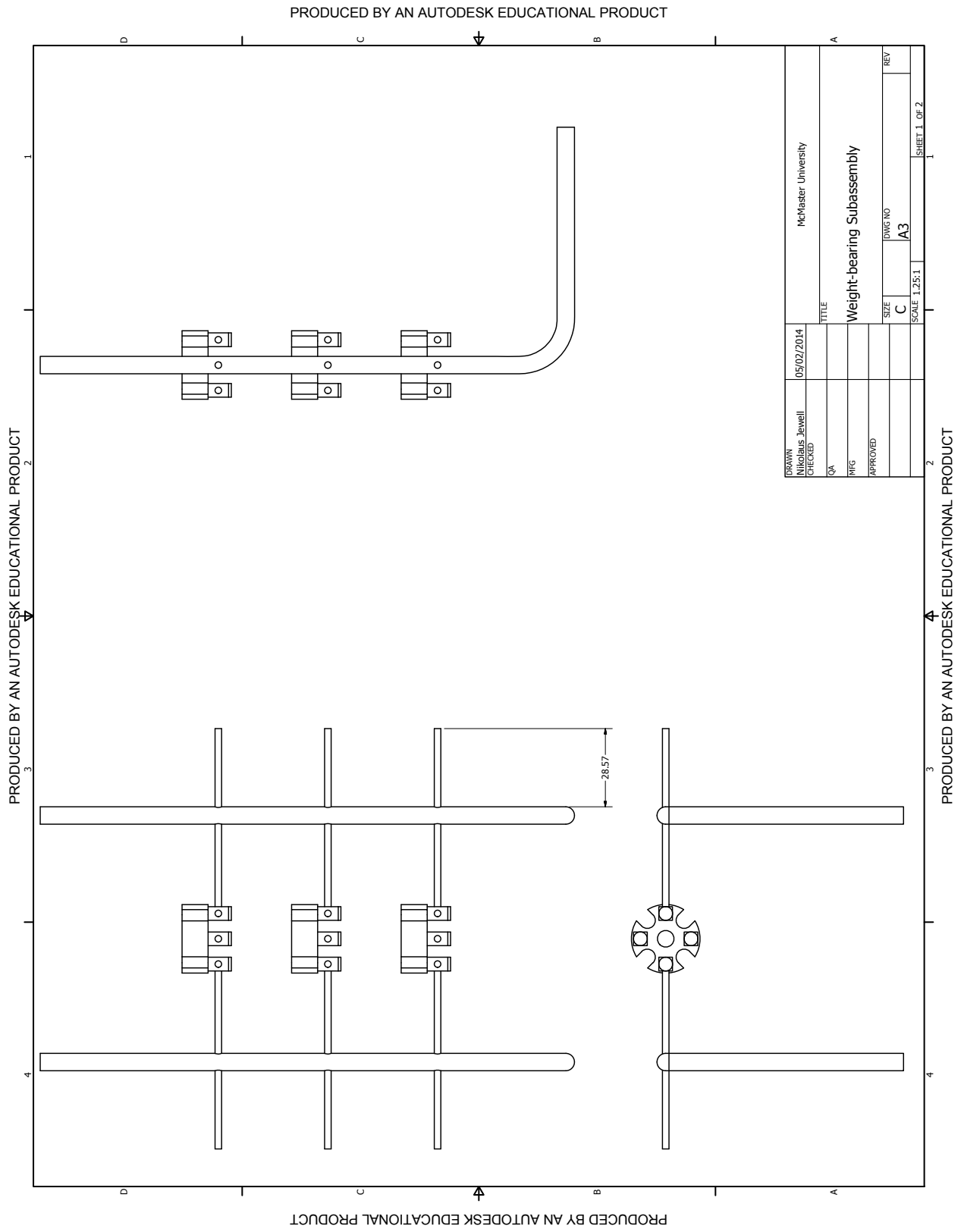

Drawing 21: Mark 2, Weight-bearing Subassembly (A3).

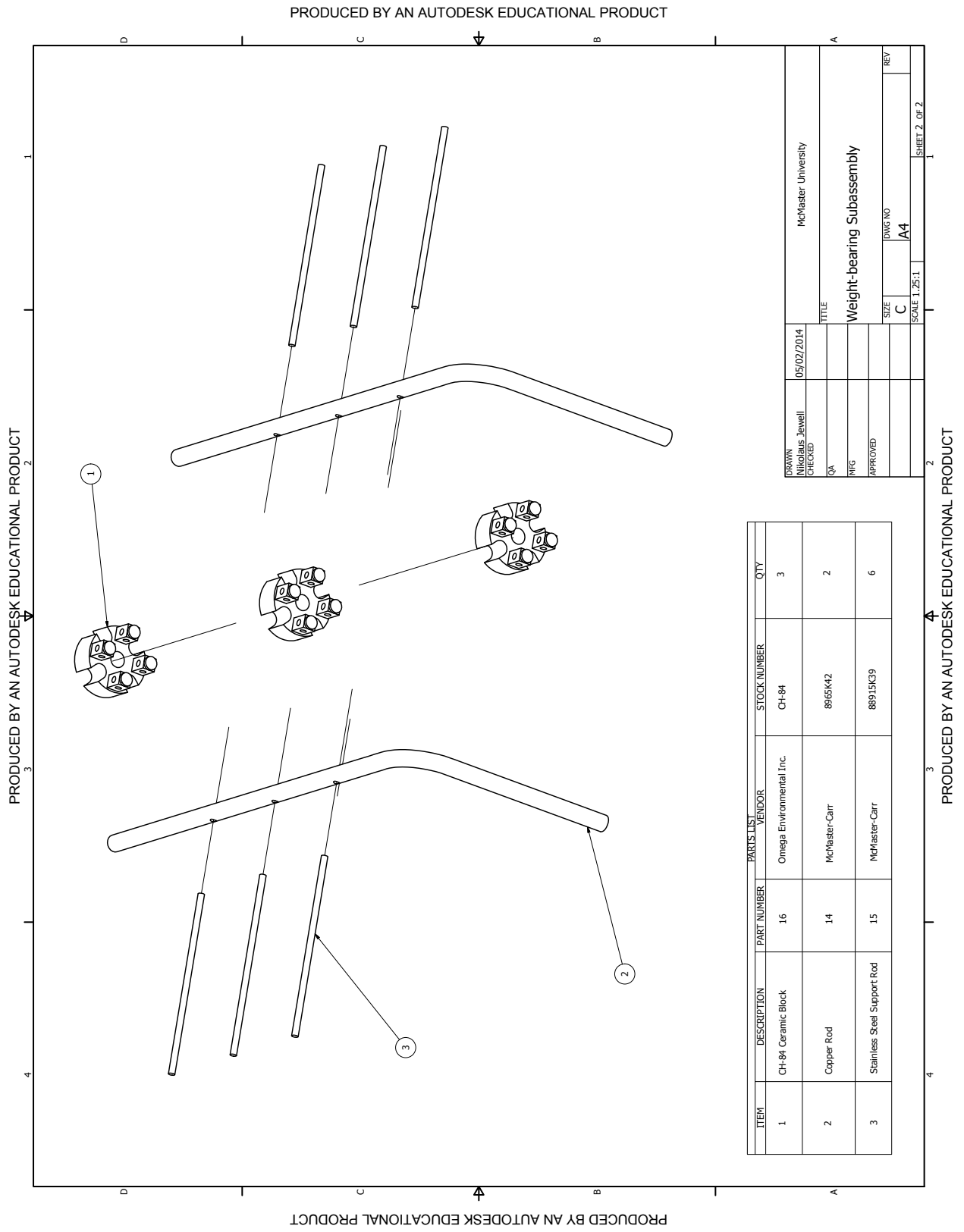
PRODUCED BY AN AUTODESK EDUCATIONAL PRODUCT
PRODUCED BY AN AUTODESK EDUCATIONAL PRODUCT
PRODUCED BY AN AUTODESK EDUCATIONAL PRODUCT
PRODUCED BY AN AUTODESK EDUCATIONAL PRODUCT
PARTS LIST
ITEM | DESCRIPTION | PART NUMBER | VENDOR | STOCK NUMBER | QTY
1 | CH-84 Ceramic Block | 16 | Omega Environmental Inc. | CH-84 | 3
2 | Copper Rod | 14 | McMaster-Carr | 8965K42 | 2
3 | Stainless Steel Support Rod | 15 | McMaster-Carr | 88915K39 | 6
DRAWN Nikolaus Jewell 05/02/2014
CHECKED
QA
MFG
APPROVED
McMaster University
TITLE
Weight-bearing Subassembly
SIZE C
DWG NO A4
REV
SCALE 1.25:1
SHEET 2 OF 2

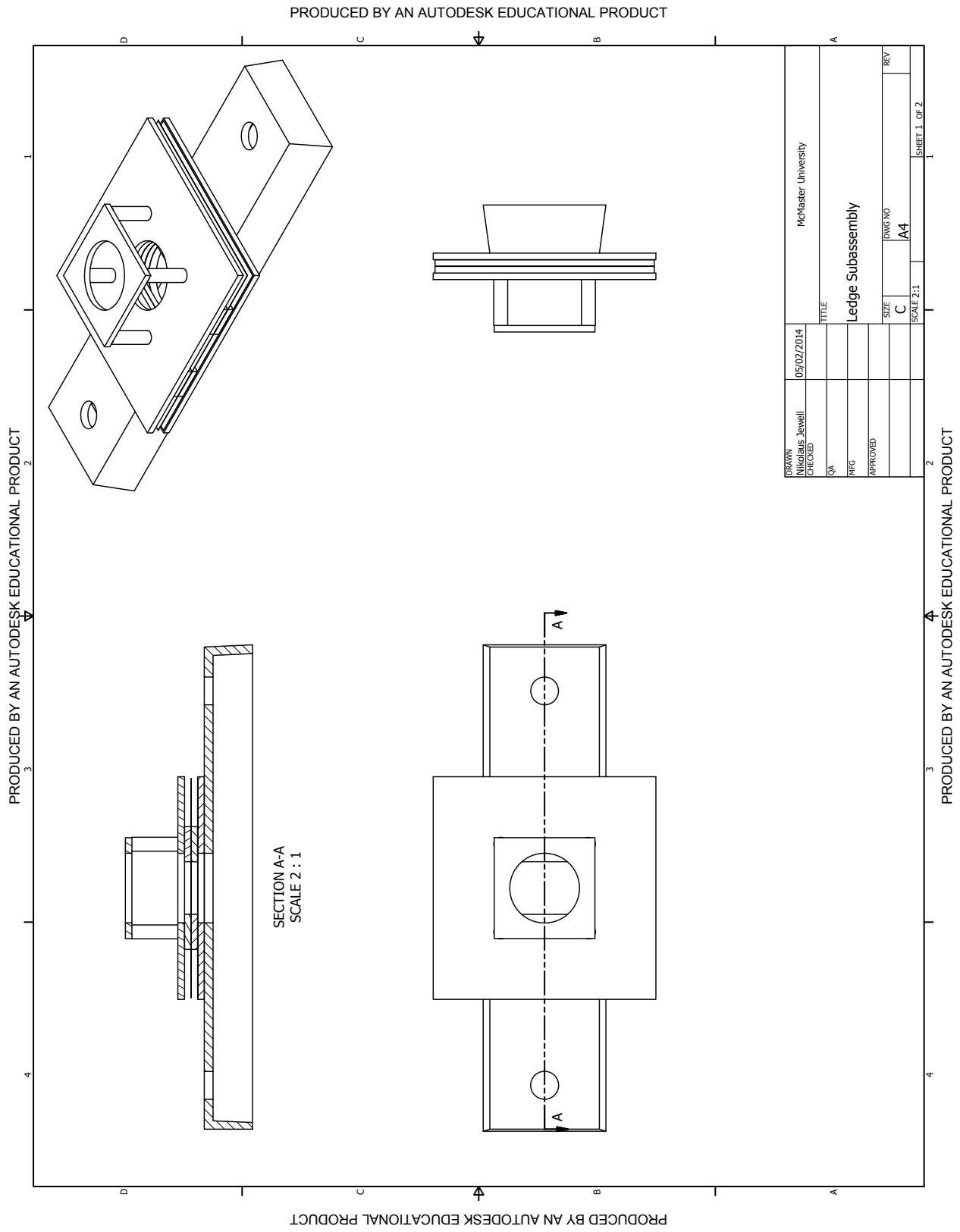

Drawing 22: Mark 2, Ledge Subassembly (A4).

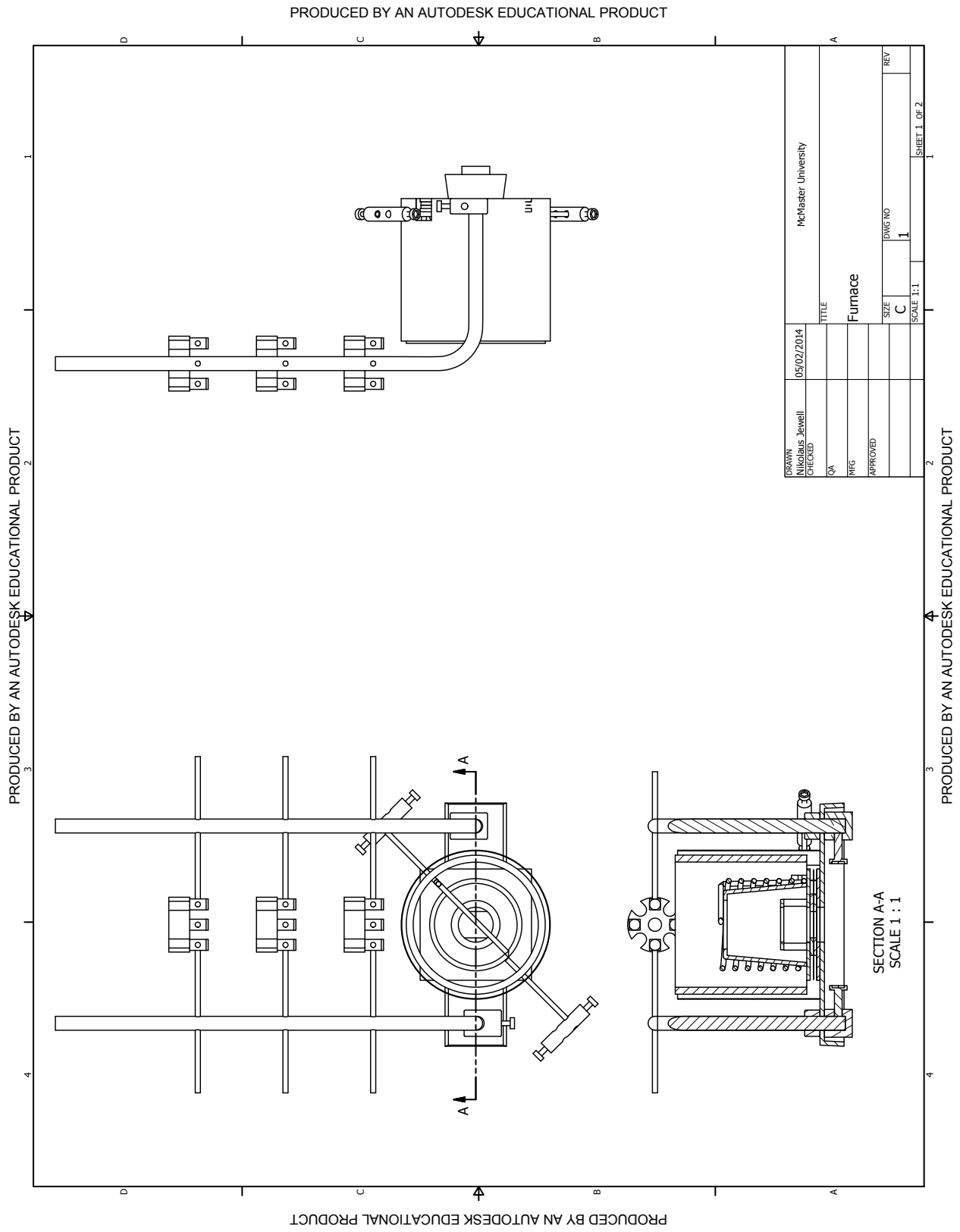

Drawing 23: Mark 2, Furnace Assembly.

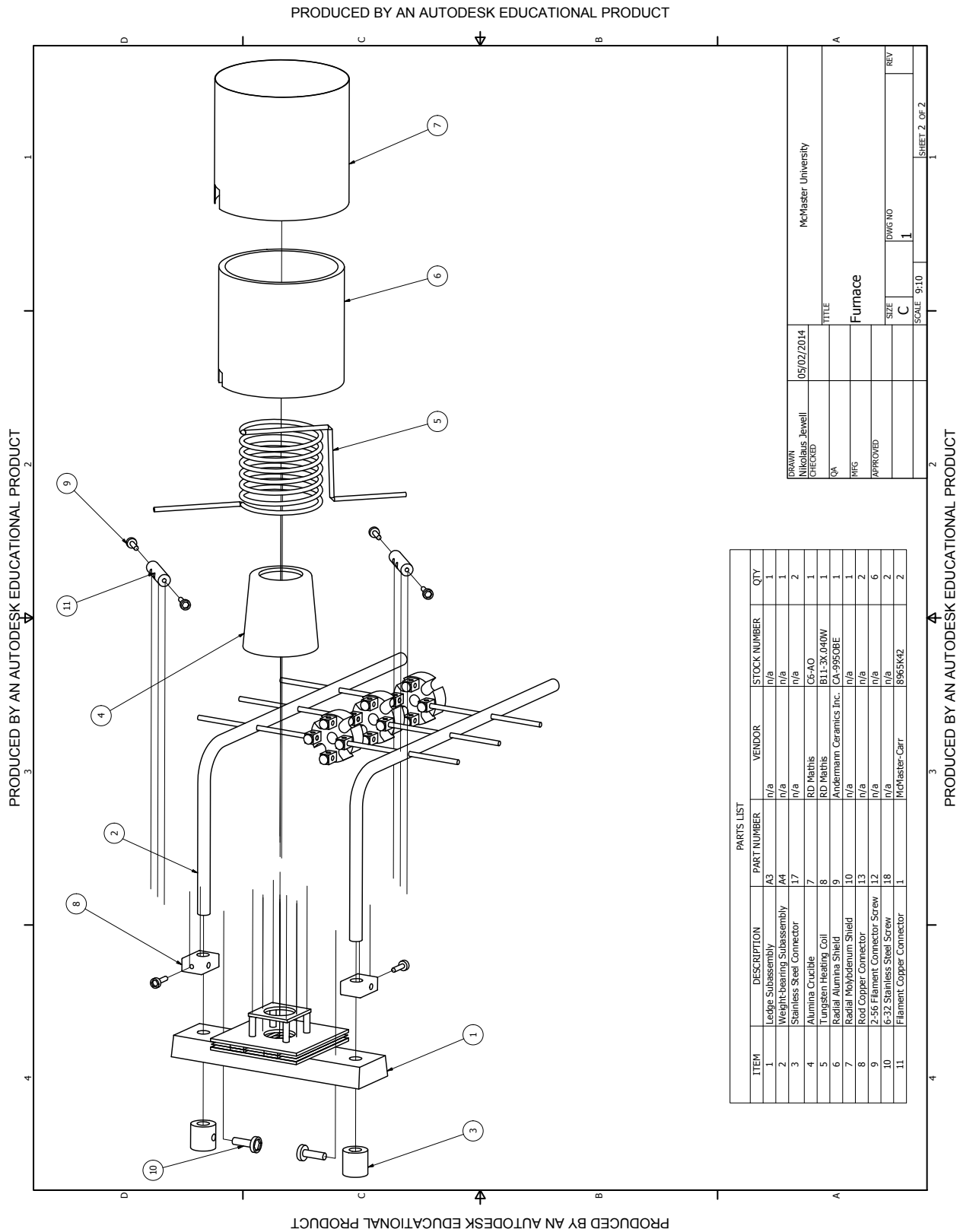
PRODUCED BY AN AUTODESK EDUCATIONAL PRODUCT
PRODUCED BY AN AUTODESK EDUCATIONAL PRODUCT
PRODUCED BY AN AUTODESK EDUCATIONAL PRODUCT
PRODUCED BY AN AUTODESK EDUCATIONAL PRODUCT
PARTS LIST
ITEM | DESCRIPTION | PART NUMBER | VENDOR | STOCK NUMBER | QTY
1 | Ledge Subassembly | A3 | n/a | n/a | 1
2 | Weight-bearing Subassembly | A4 | n/a | n/a | 1
3 | Stainless Steel Connector | 17 | n/a | n/a | 2
4 | Alumina Crucible | 7 | RD Mathis | C6-AO | 1
5 | Tungsten Heating Coil | 8 | RD Mathis | B11-3X.040W | 1
6 | Radial Alumina Shield | 9 | Andermann Ceramics Inc. | CA-995OBE | 1
7 | Radial Molybdenum Shield | 10 | n/a | n/a | 1
8 | Rod Copper Connector | 13 | n/a | n/a | 2
9 | 2-56 Filament Connector Screw | 12 | n/a | n/a | 6
10 | 6-32 Stainless Steel Screw | 18 | n/a | n/a | 2
11 | Filament Copper Connector | 1 | McMaster-Carr | 8965K42 | 2
DRAWN Nikolaus Jewell 05/02/2014
CHECKED
QA
MFG
APPROVED
McMaster University
TITLE
Furnace
SIZE C
DWG NO 1
REV
SCALE 9:10
SHEET 2 OF 2

A.5 "Mark 3" Furnace Design

A.5.1 Assembly Instructions

The following steps describe the process of assembling the "Mark 3" furnace:

Weight-bearing Subassembly (A3)

(1) Three 3/32-inch diameter stainless steel rods (Part Number 15) are press fitted into the corresponding holes on a copper rod (Part Number 14) so that approximately 28.5 mm of the stainless steel rods extend out on one side.

(2) Repeat Step (1) for the remaining 3/32-inch stainless steel rods and copper rod. Ensure that the stainless steel rods are press fitted in the opposite direction to those in Step (1).

(3) Align the lateral holes of three CH-84 ceramic blocks (Part Number 16) with the longer protruding portion of the stainless steel rods and insert them. Tighten the perpendicular screws on the CH-84 ceramic blocks using the appropriately sized screwdriver to secure the stainless steel rods.

(4) Repeat Step (3) for the other press fitted stainless steel rods.

Ledge Subassembly (A5)

(5) Using the top alumina plate (Part Number 23), partially insert four eighth-inch alumina rods (Part Number 4) into the four holes corresponding to their diameter.

(6) Align and slide the axial molybdenum shield (Part Number 6) onto the alumina rods so that it touches the underside of the top alumina plate.

(7) Align the bottom alumina plate (Part Number 21) with the holes it shares with the top alumina plate and press it against the underside of the axial molybdenum shield.

(8) Orient these parts so that they are horizontal and the protruding alumina rods extend vertically upwards. Place the structure on top of the alumina ledge (Part Number 20) so that the centre 5/8-inch diameter holes align with each other.

(9) Place the alumina sample holder (Part Number 5) on top of the four alumina rods so that its aperture aligns with the 5/8-inch hole through the top alumina plate.

Furnace Assembly

(10) Slide a copper rod connector (Part Number 24) part way up the shorter quarter-inch diameter copper rod segment of the weight-bearing subassembly.

(11) Repeat Step (10) for other copper rod in the weight-bearing subassembly.

(12) Gently, slide the quarter-inch holes of the ledge subassembly onto the shorter quarter-inch copper rod segments of weight-bearing subassembly.

(13) Securely fasten a stainless steel connector (Part Number 17) onto one of the copper rods underneath the ledge subassembly with a 6-32 stainless steel (Part Number 18) screw using the appropriate screwdriver. Ensure that the flat head of the screw faces towards the centre of the ledge subassembly.

(12) Repeat Step (13) for the other side of the weight-bearing subassembly.

(13) Carefully, place the alumina crucible (Part Number 7) about the sample holder on the centre of the ledge subassembly.

(14) Place the tungsten heating coil (Part Number 8) on top of the alumina crucible on the centre of the ledge subassembly. Ensure the leads of the filament are positioned at an approximate 45-degree angle to the length of alumina ledge.

(15) Place the alumina radial shield (Part Number 9) about the alumina crucible on the centre of the ledge subassembly. Ensure that the shield is oriented so that the leads of the filament pass through the shield's bottom openings.

(16) Place the molybdenum radial shield (Part Number 25) about the alumina crucible on the centre of the ledge subassembly. Ensure that the shield is oriented so that the leads of the filament pass through the shield's openings.

(17) Attach a filament copper connector (Part Number 11) to one of the ends of the tungsten filament by sliding the filament lead into one the non-threaded holes and then securely tighten the adjacent 2-56 stainless steel screw (Part Number 12) using the appropriate screw driver. Ensure that the filament connector end without a screw in it is oriented in the direction towards the closer copper rod connector.

(18) Repeat Step (17) for the other filament end.

(19) Insert a 2.5-inch long stranded 26 AWG (American wire gauge) copper wire into the non-threaded vacant hole of a copper rod connector (Part Number 24).

(20) Insert a 6-32 stainless steel screw (Part Number 18) into the threaded hole of copper rod connector. Tighten the screw using the appropriate screwdriver to ensure a good electrical connection.

(21) Insert the other end of the stranded copper wire from Step (19) into the non-threaded hole of the closer filament copper connector and create a secure electrical connection by tightening the adjacent 2-56 stainless steel screw (Part Number 12) using the appropriate screw driver.

(22) Repeat Steps (19)-(21) for the remaining stranded copper wire and filament copper connector.

A.5.2 Engineering Part Drawings

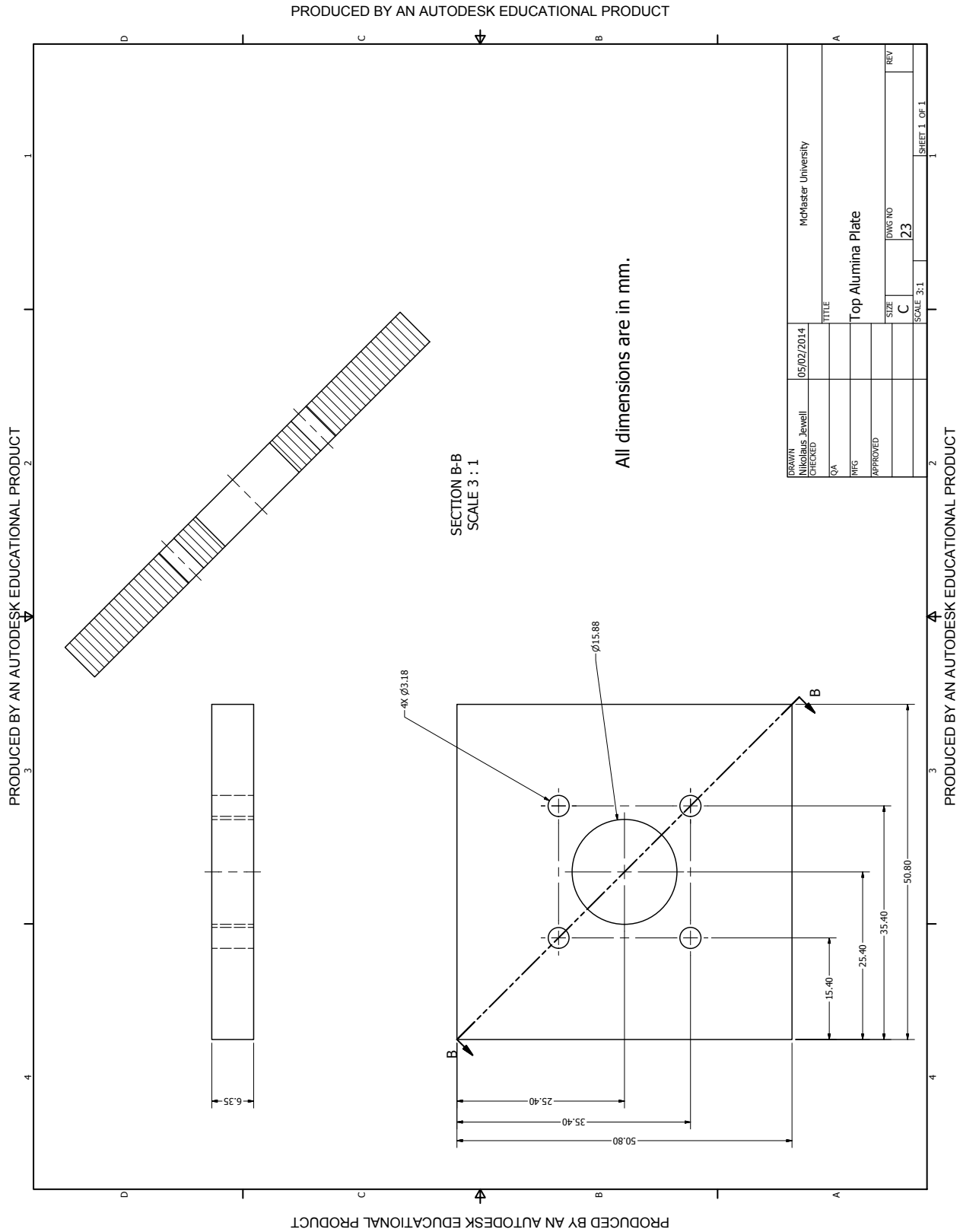

Drawing 24: Mark 3, Top Alumina Plate.

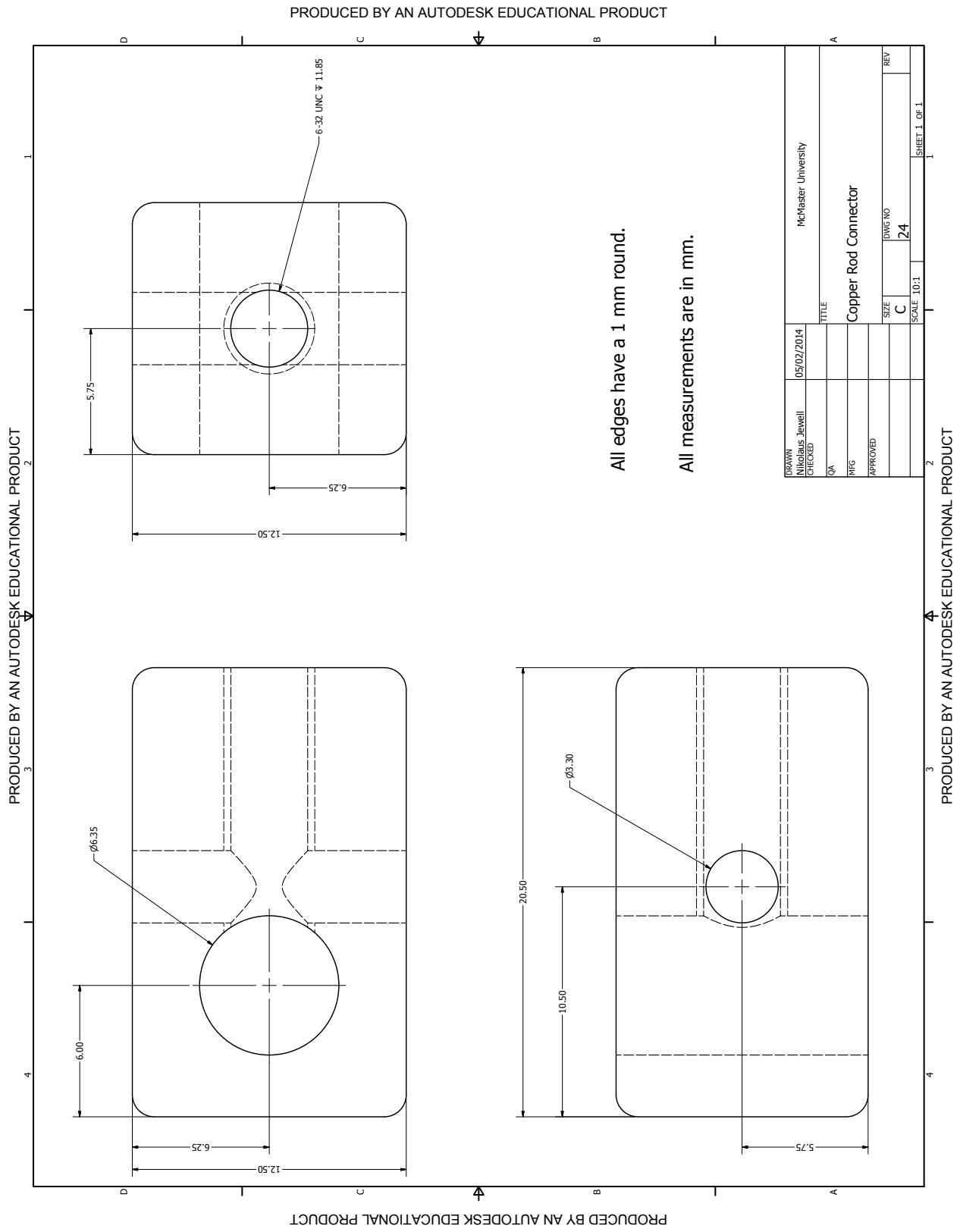

Drawing 25: Mark 3, Copper Rod Connector.

A.5.3 Assembly Drawings

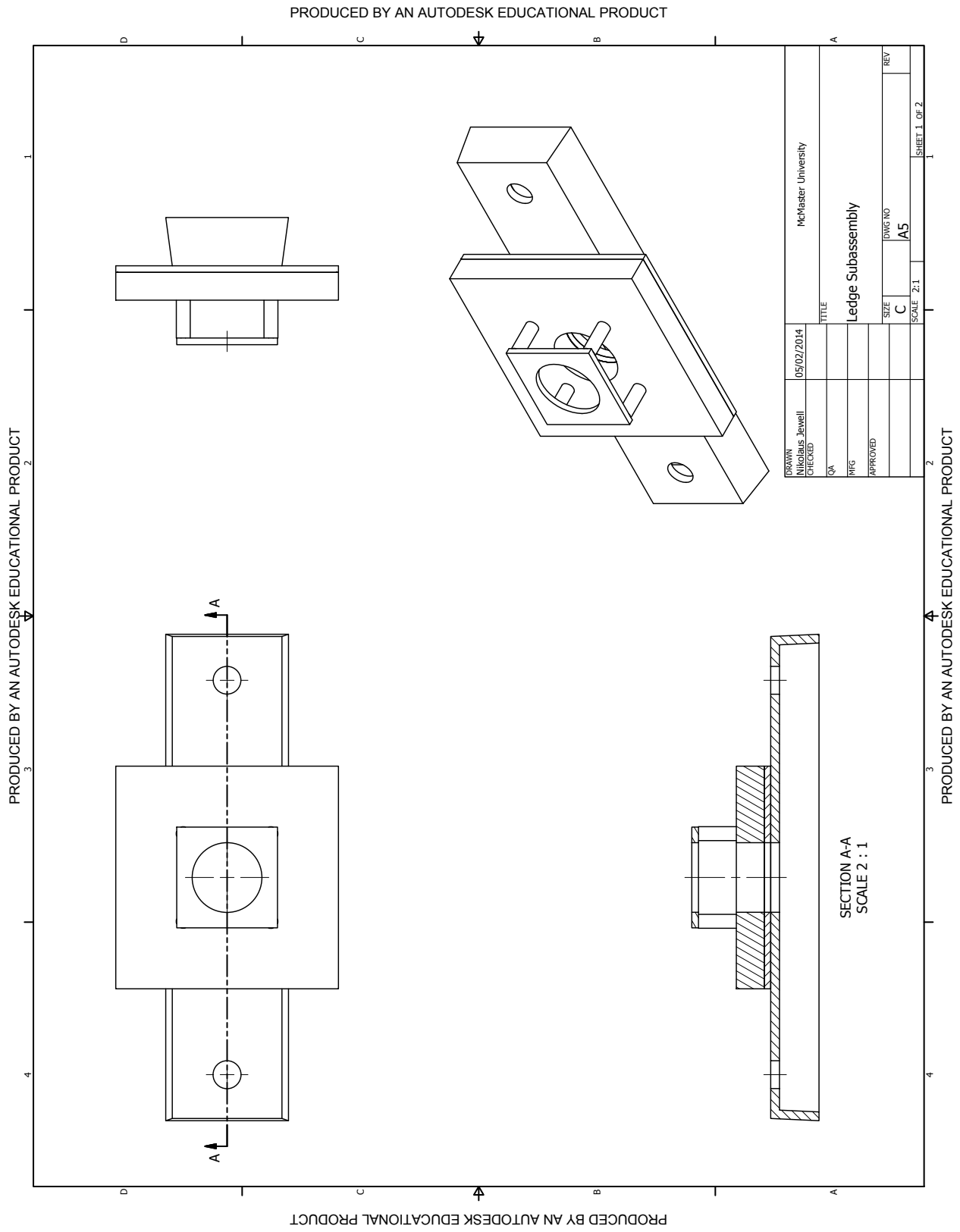

Drawing 26: Mark 3, Ledge Subassembly (A5).

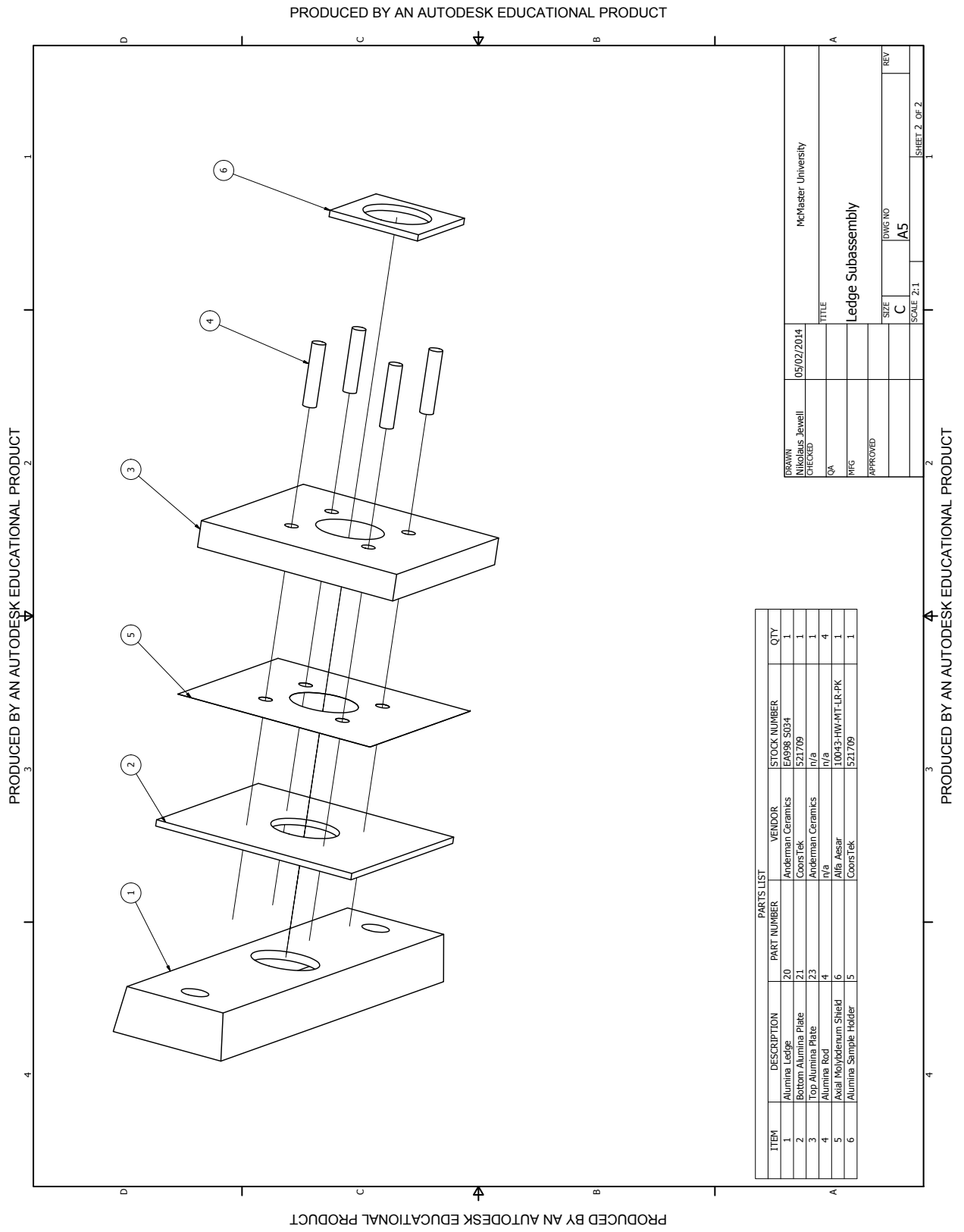
PRODUCED BY AN AUTODESK EDUCATIONAL PRODUCT
PRODUCED BY AN AUTODESK EDUCATIONAL PRODUCT
PRODUCED BY AN AUTODESK EDUCATIONAL PRODUCT
PRODUCED BY AN AUTODESK EDUCATIONAL PRODUCT
PARTS LIST
ITEM | DESCRIPTION | PART NUMBER | VENDOR | STOCK NUMBER | QTY
1 | Alumina Ledge | 20 | Anderman Ceramics | EA998 S034 | 1
2 | Bottom Alumina Plate | 21 | CoorsTek | 521709 | 1
3 | Top Alumina Plate | 23 | Anderman Ceramics | n/a | 1
4 | Alumina Rod | 4 | n/a | n/a | 4
5 | Axial Molybdenum Shield | 6 | Alfa Aesar | 10043-HW-MT-LR-PK | 1
6 | Alumina Sample Holder | 5 | CoorsTek | 521709 | 1
DRAWN Nikolaus Jewell 05/02/2014
CHECKED
QA
MFG
APPROVED
McMaster University
TITLE
Ledge Subassembly
SIZE C
DWG NO A5
REV
SCALE 2:1
SHEET 2 OF 2

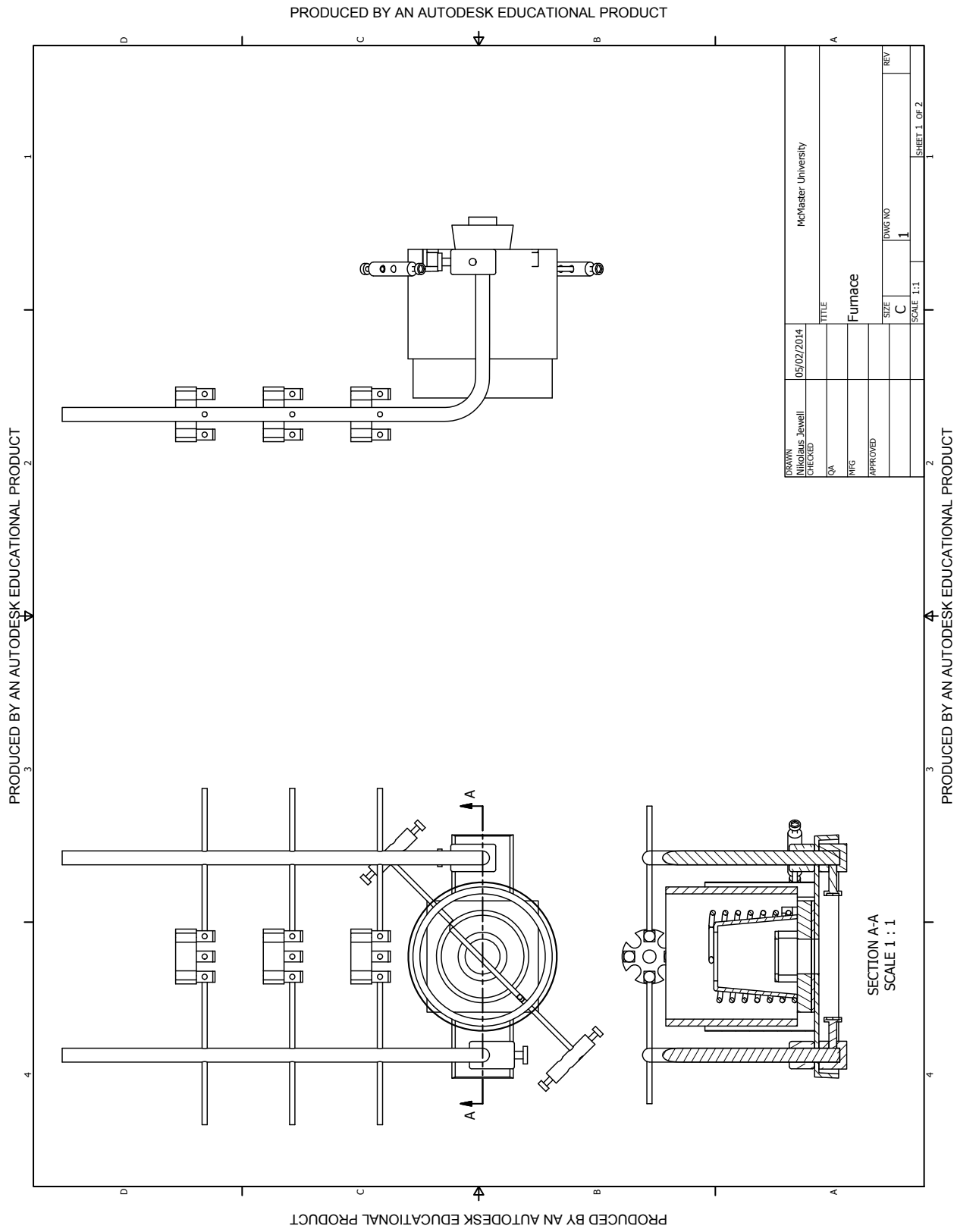

Drawing 27: Mark 3, Furnace Assembly.

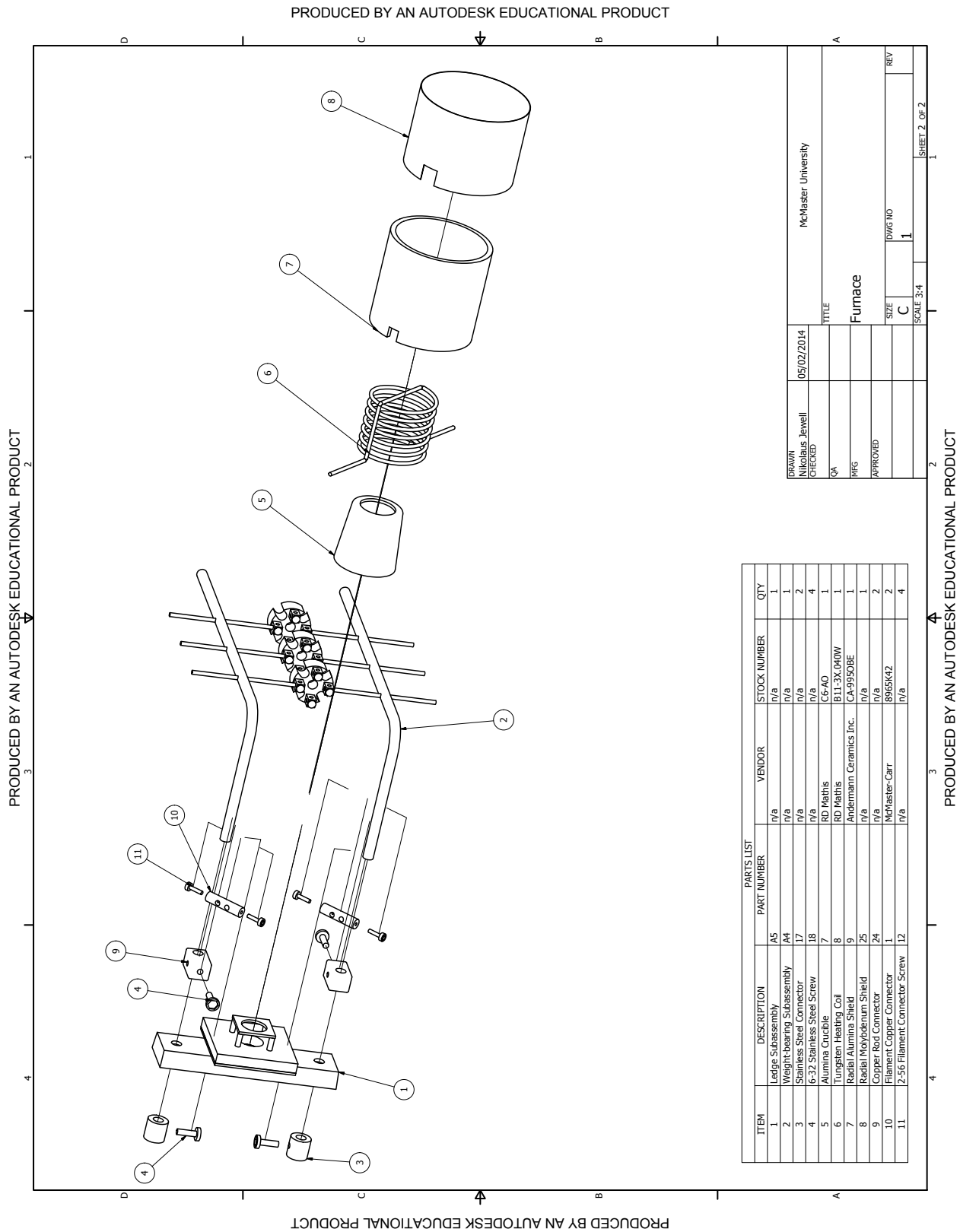
PRODUCED BY AN AUTODESK EDUCATIONAL PRODUCT
PRODUCED BY AN AUTODESK EDUCATIONAL PRODUCT
PRODUCED BY AN AUTODESK EDUCATIONAL PRODUCT
PRODUCED BY AN AUTODESK EDUCATIONAL PRODUCT
PARTS LIST
ITEM | DESCRIPTION | PART NUMBER | VENDOR | STOCK NUMBER | QTY
1 | Ledge Subassembly | A5 | n/a | n/a | 1
2 | Weight-bearing Subassembly | A4 | n/a | n/a | 1
3 | Stainless Steel Connector | 17 | n/a | n/a | 2
4 | 6-32 Stainless Steel Screw | 18 | n/a | n/a | 4
5 | Alumina Crucible | 7 | RD Mathis | C6-AO | 1
6 | Tungsten Heating Coil | 8 | RD Mathis | B11-3X.040W | 1
7 | Radial Alumina Shield | 9 | Andermann Ceramics Inc. | CA-995OBE | 1
8 | Radial Molybdenum Shield | 25 | n/a | n/a | 1
9 | Copper Rod Connector | 24 | n/a | n/a | 2
10 | Filament Copper Connector | 1 | McMaster-Carr | 8965K42 | 2
11 | 2-56 Filament Connector Screw | 12 | n/a | n/a | 4
DRAWN Nikolaus Jewell 05/02/2014
CHECKED
QA
MFG
APPROVED
McMaster University
TITLE
Furnace
SIZE C
DWG NO 1
REV
SCALE 3:4
SHEET 2 OF 2

A.6 Graphite Target Holder

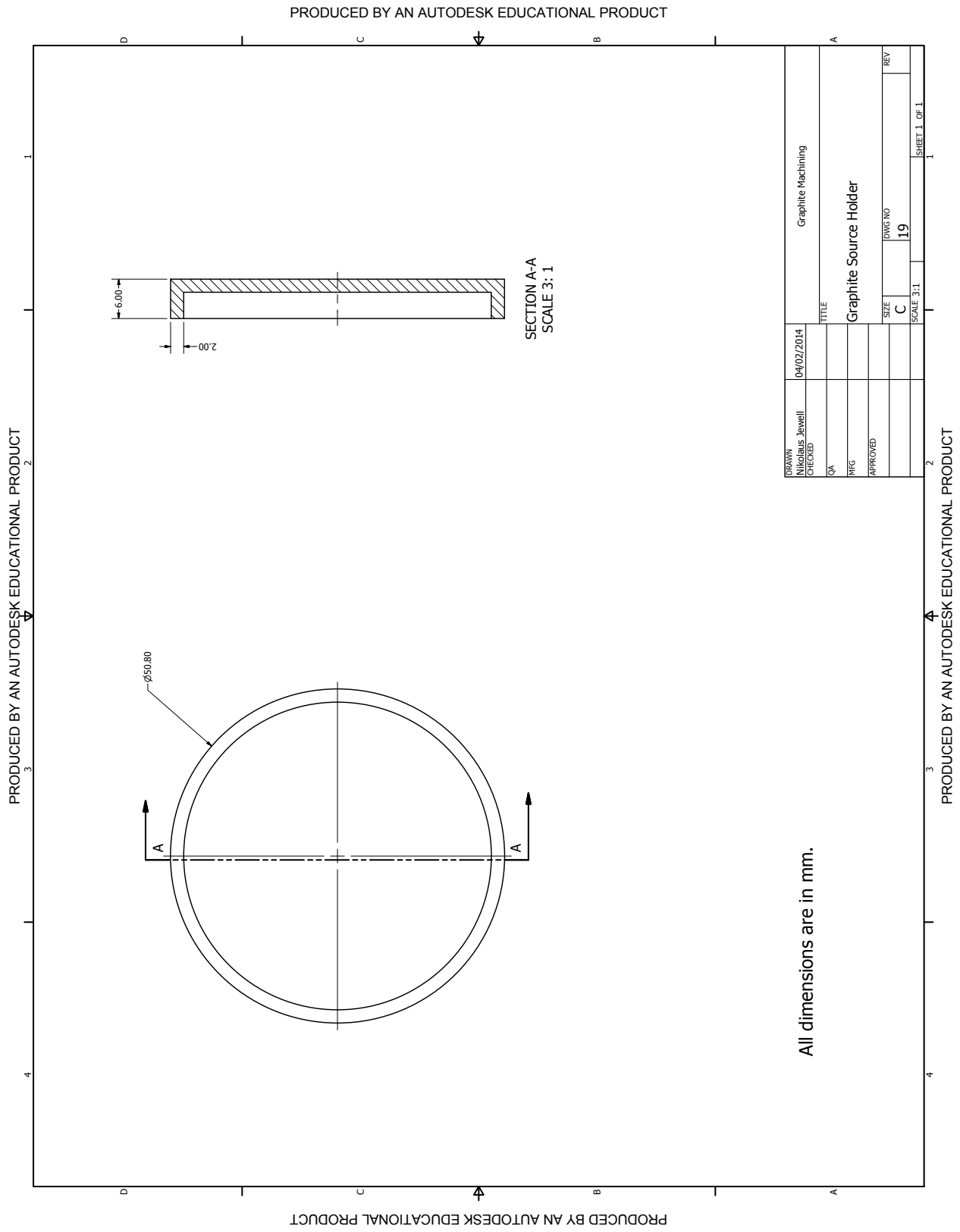

Drawing 28: Graphite Source Holder.